

UC San Diego

UC San Diego Electronic Theses and Dissertations

Title

First-Principles Study of Hybrid Halide Perovskites and Beyond for Optoelectronic Applications

Permalink

<https://escholarship.org/uc/item/2rk8n3j0>

Author

Li, Yuheng

Publication Date

2020

Peer reviewed|Thesis/dissertation

UNIVERSITY OF CALIFORNIA SAN DIEGO

First-Principles Study of Hybrid Halide Perovskites and Beyond for Optoelectronic Applications

A dissertation submitted in partial satisfaction of the
requirements for the degree
Doctor of Philosophy

in

NanoEngineering

by

Yuheng Li

Committee in charge:

Professor Kesong Yang, Chair
Professor David P. Fenning
Professor Francesco Paesani
Professor Sheng Xu
Professor Yi-Zhuang You

2020

Copyright
Yuheng Li, 2020
All rights reserved.

The dissertation of Yuheng Li is approved, and it is acceptable in quality and form for publication on microfilm and electronically:

Chair

University of California San Diego

2020

TABLE OF CONTENTS

	Signature Page	iii
	Table of Contents	iv
	List of Figures	vi
	List of Tables	ix
	Acknowledgements	x
	Vita	xii
	Abstract of the Dissertation	xiii
Chapter 1	Introduction	1
	1.1 Lead Halide Perovskites	1
	1.1.1 Promise in Optoelectronics	1
	1.1.2 Challenges	2
	1.2 High-Throughput Materials Design	3
	1.2.1 Materials Properties and Materials Descriptors	4
	1.2.2 Prior Predictions for Perovskite Optoelectronics	8
	1.3 Summary	13
Chapter 2	High-Throughput Computational Design of Organic-Inorganic Hybrid Halide Semiconductors beyond Perovskites for Optoelectronics	16
	2.1 Introduction	17
	2.2 Methods	19
	2.3 Results	20
	2.3.1 Building Repository	20
	2.3.2 Screening Process	22
	2.4 Discussion	28
	2.4.1 Composition and Structure	28
	2.4.2 Electronic Structures	32
	2.5 Conclusion	35
	2.6 Acknowledgments	35
Chapter 3	Stability Diagrams, Defect Tolerance, and Absorption Coefficients of Hybrid Halide Semiconductors: High-throughput First-principles Characterization	36
	3.1 Introduction	37
	3.2 Methods	38
	3.3 Results and Discussion	41

	3.3.1	Stability Diagram	41
	3.3.2	Defect Tolerance	43
	3.3.3	Absorption Coefficient	47
	3.4	Conclusion	49
	3.5	Acknowledgments	49
Chapter 4		Enhancing Ferroelectric Dipole Ordering in the Organic-Inorganic Hybrid Perovskite $\text{CH}_3\text{NH}_3\text{PbI}_3$: Strain and Doping Engineering	50
	4.1	Introduction	51
	4.2	Computational Details	53
	4.3	Results and Discussion	54
	4.3.1	In-Phase Rotation	54
	4.3.2	Out-of-Phase Rotation	56
	4.3.3	Spontaneous Ferroelectric Dipole Ordering	59
	4.3.4	Strain Engineering	62
	4.3.5	Doping Engineering	64
	4.4	Conclusion	66
	4.5	Acknowledgments	67
Chapter 5		First-Principles Investigation of Epitaxial Stabilization and Strain Engineering of α -FAPbI ₃	68
	5.1	Introduction	68
	5.2	Computational Details	69
	5.3	Results and Discussion	70
	5.3.1	Epitaxial Stabilization of α -FAPbI ₃	70
	5.3.2	Strained α -FAPbI ₃	76
	5.4	Conclusion	79
	5.5	Acknowledgements	80
Chapter 6		Conclusion and Outlook	81
	6.1	Outlook on High-Throughput Design of Halide Perovskites and Beyond for Optoelectronics	81
	6.2	Conclusion	84
	6.3	Acknowledgements	86
Appendix A		Prototype Structures, Anisotropic Effective Masses, and AIMD results for HT Materials Design	88
Appendix B		Phase Diagrams, Defect Tolerance, and Absorption Coefficients for the 29 Perovskite Derivatives	95
References		110

LIST OF FIGURES

Figure 2.1:	Schematic diagram of the high-throughput screening process.	22
Figure 2.2:	Total energy during 5ps <i>ab-initio</i> molecular dynamics (AIMD) simulations at 300K for two representative hybrid materials: (a) (MA) ₃ In ₂ I ₉ (hP14) and (b) (MA) ₂ ZrI ₆ (tI18).	26
Figure 2.3:	Representative candidates and their prototype structures, calculated electronic band structures, and atomic orbital projected density of states.	34
Figure 3.1:	Schematic illustration of (a) crystal structure, (b) stability diagram, and (c-d) defect properties of MA ₂ SnI ₄	43
Figure 3.2:	Schematic illustration of (a) crystal structure, (b) stability diagram, and (c-d) defect properties of MA ₃ Sb ₂ I ₉	45
Figure 3.3:	Calculated optical absorption coefficients (α) of (a) MA ₂ SnI ₄ and (b) MA ₃ Sb ₂ I ₉ with hybrid functional theory calculations at HSE06 level.	47
Figure 4.1:	Schematic illustration of the rotation modes for the MA cations.	55
Figure 4.2:	Calculated total energy change as a function of MA out-of-phase rotation angle in the tetragonal MAPbI ₃	57
Figure 4.3:	Relaxed structures with different MA ordering configurations.	60
Figure 4.4:	Energy difference between each AFE structure and the FE structure (ΔE_{AFE-FE}) (in green and red) and cell aspect ratio (c/a) (in black) versus (a) biaxial strains, and (b) uniaxial strains.	62
Figure 4.5:	Energy difference between each AFE structure and the FE structure (ΔE_{AFE-FE}) (in green and red) and cell aspect ratio (c/a) (in black) versus (a) Br doping concentration (c_{Br}) and (b) Cl doping concentration (c_{Cl}).	65
Figure 5.1:	First-principles calculations of epitaxial stabilization.	71
Figure 5.2:	First-principles calculations of the strained α -FAPbI ₃ unit cell under different strains.	77
Figure 5.3:	Calculated effective masses of the carriers at different strains, and electronic band structures under three strain levels (3%, 0%, and -3%).	78
Figure A.1:	Structures of the 24 perovskite-derived inorganic metal halide compounds (Cs _x B _y X _z) used as structural prototypes (HY.001-HY.024) to build the hybrid metal halide compound repository.	89
Figure A.2:	Total energy during 5ps <i>ab-initio</i> molecular dynamics (AIMD) simulations at 300K for all the screened tI14 compounds.	91
Figure A.3:	Total energy during 5ps <i>ab-initio</i> molecular dynamics (AIMD) simulations at 300K for all the screened hP14 compounds.	92
Figure A.4:	Total energy during 5ps <i>ab-initio</i> molecular dynamics (AIMD) simulations at 300K for all the screened tI18 compounds.	93
Figure A.5:	Total energy during 5ps <i>ab-initio</i> molecular dynamics (AIMD) simulations at 300K for all the screened cF36 compounds.	93

Figure A.6: Total energy during 5ps <i>ab-initio</i> molecular dynamics (AIMD) simulations at 300K for all the screened hP28 compounds.	94
Figure B.1: Convergence test for charged defect calculations.	95
Figure B.2: Calculated stability diagram for tI14 compounds.	97
Figure B.3: Calculated stability diagram of hP14 compounds.	98
Figure B.4: Calculated stability diagram of hP28 compounds.	99
Figure B.5: Calculated stability diagram of tI18 compounds.	99
Figure B.6: Calculated stability diagram of cF36 compounds.	99
Figure B.7: Calculated (a) defect formation energy and (b) transition energy levels for MA ₂ GeBr ₄ (tI14).	100
Figure B.8: Calculated (a) defect formation energy and (b) transition energy levels for MA ₂ GeI ₄ (tI14).	100
Figure B.9: Calculated (a) defect formation energy and (b) transition energy levels for MA ₂ SnCl ₄ (tI14).	100
Figure B.10: Calculated (a) defect formation energy and (b) transition energy levels for MA ₂ SnBr ₄ (tI14).	101
Figure B.11: Calculated (a) defect formation energy and (b) transition energy levels for FA ₂ SnBr ₄ (tI14).	101
Figure B.12: Calculated (a) defect formation energy and (b) transition energy levels for AD ₂ GeI ₄ (tI14).	101
Figure B.13: Calculated (a) defect formation energy and (b) transition energy levels for AD ₂ SnBr ₄ (tI14).	102
Figure B.14: Calculated (a) defect formation energy and (b) transition energy levels for AD ₂ SnI ₄ (tI14).	102
Figure B.15: Calculated (a) defect formation energy and (b) transition energy levels for MA ₂ SnI ₄ (tI14).	102
Figure B.16: Calculated (a) defect formation energy and (b) transition energy levels for MA ₃ In ₂ I ₉ (hP14).	103
Figure B.17: Calculated (a) defect formation energy and (b) transition energy levels for MA ₃ Sb ₂ Br ₉ (hP14).	103
Figure B.18: Calculated (a) defect formation energy and (b) transition energy levels for MA ₃ Sb ₂ I ₉ (hP14).	103
Figure B.19: Calculated (a) defect formation energy and (b) transition energy levels for MA ₃ Bi ₂ I ₉ (hP14).	104
Figure B.20: Calculated (a) defect formation energy and (b) transition energy levels for FA ₃ Ga ₂ I ₉ (hP14).	104
Figure B.21: Calculated (a) defect formation energy and (b) transition energy levels for FA ₃ In ₂ Br ₉ (hP14).	104
Figure B.22: Calculated (a) defect formation energy and (b) transition energy levels for FA ₃ In ₂ I ₉ (hP14).	105
Figure B.23: Calculated (a) defect formation energy and (b) transition energy levels for FA ₃ Bi ₂ I ₉ (hP14).	105

Figure B.24: Calculated (a) defect formation energy and (b) transition energy levels for AD ₃ Sb ₂ Br ₉ (hP14).	105
Figure B.25: Calculated (a) defect formation energy and (b) transition energy levels for AD ₃ Sb ₂ I ₉ (hP14).	106
Figure B.26: Calculated (a) defect formation energy and (b) transition energy levels for AD ₃ Bi ₂ I ₉ (hP14).	106
Figure B.27: Calculated (a) defect formation energy and (b) transition energy levels for FA ₃ Sb ₂ I ₉ (hP28).	106
Figure B.28: Calculated (a) defect formation energy and (b) transition energy levels for AD ₃ In ₂ I ₉ (hP14).	107
Figure B.29: Calculated (a) defect formation energy and (b) transition energy levels for MA ₂ ZrI ₆ (tI18).	107
Figure B.30: Calculated (a) defect formation energy and (b) transition energy levels for AD ₂ HfI ₆ (tI18).	107
Figure B.31: Calculated (a) defect formation energy and (b) transition energy levels for AD ₂ SnBr ₆ (tI18).	108
Figure B.32: Calculated (a) defect formation energy and (b) transition energy levels for AD ₂ TeBr ₆ (tI18).	108
Figure B.33: Calculated (a) defect formation energy and (b) transition energy levels for MA ₂ SnI ₆ (cF36).	108
Figure B.34: Calculated (a) defect formation energy and (b) transition energy levels for MA ₂ TeI ₆ (cF36).	109
Figure B.35: Calculated (a) defect formation energy and (b) transition energy levels for AD ₂ TeI ₆ (cF36).	109
Figure B.36: Calculated optical absorption coefficients (α) for all the tI14 compounds.	113
Figure B.37: Calculated optical absorption coefficients (α) for all the hP14 compounds.	114
Figure B.38: Calculated optical absorption coefficients (α) for all the tI18 compounds.	115
Figure B.39: Calculated optical absorption coefficients (α) for all the cF36 compounds.	115
Figure B.40: Calculated optical absorption coefficients (α) for all the hP28 compounds.	115

LIST OF TABLES

Table 1.1:	List of compounds in the search space of IVA element-based single perovskites designed from high-throughput computational studies reviewed.	9
Table 1.2:	List of compounds in the search space of other element-based single perovskites designed from high-throughput computational studies reviewed. . .	10
Table 1.3:	List of compounds in the search space of double perovskites designed from high-throughput computational studies reviewed.	11
Table 1.4:	List of compounds in the search space of perovskite derivatives designed from high-throughput computational studies reviewed.	14
Table 2.1:	Structural properties of the $\text{Cs}_x\text{B}_y\text{X}_z$ compounds used to extract prototype structures.	20
Table 2.2:	Properties of selected hybrid halide compounds for light-emitting materials.	30
Table 2.3:	Properties of selected hybrid halide compounds for solar-cell materials. . . .	32
Table 3.1:	List of 29 candidate hybrid halide semiconductor materials.	40
Table 4.1:	Relaxed lattice parameters of the MAPbI_3 with different MA ordering configurations and their discrepancies (δ) with the experimental values.	59
Table 5.1:	Thermodynamic terms relevant to epitaxial nucleation of α - FAPbI_3 and δ - FAPbI_3 on cubic MAPbBr_3 substrates.	75
Table A.1:	Calculated properties for the reference compound MASnBr_3 (cP5) using different functionals.	88
Table A.2:	Calculated electron and hole effective masses along major directions for the anisotropic tI14, hP14, hP28, and tI18 candidates.	90
Table B.1:	Cell sizes for defect calculations of exemplary compounds in the five prototype structures.	96
Table B.2:	Defect tolerance level determination for the tI14 compounds.	110
Table B.3:	Defect tolerance level determination for the hP14 compounds.	111
Table B.4:	Defect tolerance level determination for the hP28 compounds.	112
Table B.5:	Defect tolerance level determination for the tI18 compounds.	112
Table B.6:	Defect tolerance level determination for the cF36 compounds.	112

ACKNOWLEDGEMENTS

First and foremost, I would like to express my gratitude to my dissertation advisor, Professor Kesong Yang, for his guidance and support during my graduate studies. I greatly appreciate your patience and trust that helped me transform from an undergraduate novice to a scientific researcher. Beyond your always inspiring insights, your diligence and academic integrity and taste have set an excellent example for me to follow.

I am grateful to my dissertation committee members, Professor David P. Fenning, Professor Francesco Paesani, Professor Sheng Xu, and Professor Yi-Zhuang You, for their advice and support in the completion of this dissertation.

I thank my fellow students and friends in the Yang Group, Dr. Jianli Cheng, Dr. Maziar Behtash, Dr. Paul H. Joo, Dr. Safdar Nazir, Sicong Jiang, Jingning Zhang, Dr. Liyuan Wu, Dr. Yaqin Wang, and Joseph Wong, for all the helpful discussions and the memorable days. I thank my collaborators and friends Dr. Yimu Chen and Yusheng Lei, as well as Dr. Shen Wang and all the other PSC journal club friends.

I thank my mother and father for their constant love and support. I thank you for giving me the resilience to overcome all the difficulties.

I thank my wife, Yubin Kang, for all our joys of life. I thank you for moving from London to San Diego and always being there with me through my brightest days and darkest hours along this journey. You bring happiness and encouragement to the pursuit of my dreams.

Chapter 1, in part, is a reprint of the material “High-Throughput Computational Design of Halide Perovskites and Beyond for Optoelectronics” as it appears in WIREs Computational Molecular Science. Yuheng Li, Kesong Yang, e1500, 2020. The dissertation author was the primary investigator and author of this paper.

Chapter 2, in full, is a reprint of the material “High-Throughput Computational Design of Organic–Inorganic Hybrid Halide Semiconductors Beyond Perovskites for Optoelectronics” as it appears in Energy & Environmental Science. Yuheng Li, Kesong Yang, 12, 2233-2243, 2019.

The dissertation author was the primary investigator and author of this paper.

Chapter 3, in full, is a reprint of the material “Stability Diagrams, Defect Tolerance, and Absorption Coefficients of Hybrid Halide Semiconductors: High-Throughput First-Principles Characterization” as it appears in *The Journal of Chemical Physics*. Yuheng Li, Daniel Maldonado-Lopez, Valeria Ríos Vargas, Jingning Zhang, Kesong Yang, 152, 084106, 2020. The dissertation author was the primary investigator and author of this paper.

Chapter 4, in full, is a reprint of the material “Enhancing Ferroelectric Dipole Ordering in Organic–Inorganic Hybrid Perovskite $\text{CH}_3\text{NH}_3\text{PbI}_3$: Strain and Doping Engineering” as it appears in *The Journal of Physical Chemistry C*. Yuheng Li, Maziar Behtash, Joseph Wong, Kesong Yang, 122, 177-184, 2018. The dissertation author was the primary investigator and author of this paper.

Chapter 5, in part, is a reprint of the material “Strain Engineering and Epitaxial Stabilization of Halide Perovskites” as it appears in *Nature*. Yimu Chen, Yusheng Lei, Yuheng Li, Yugang Yu, Jinze Cai, Ming-Hui Chiu, Rahul Rao, Yue Gu, Chunfeng Wang, Woojin Choi, Hongjie Hu, Chonghe Wang, Yang Li, Jiawei Song, Jingxin Zhang, Baiyan Qi, Muiyang Lin, Zhuorui Zhang, Ahmad E. Islam, Benji Maruyama, Shadi Dayeh, Lain-Jong Li, Kesong Yang, Yu-Hwa Lo, Sheng Xu, 577, 209-215, 2020. The dissertation author was a co-author of this paper.

Chapter 6, in part, is a reprint of the material “High-Throughput Computational Design of Halide Perovskites and Beyond for Optoelectronics” as it appears in *WIREs Computational Molecular Science*. Yuheng Li, Kesong Yang, e1500, 2020. The dissertation author was the primary investigator and author of this paper.

VITA

- 2015 B. E. in Materials Science and Engineering, Zhejiang University
- 2020 Ph. D. in NanoEngineering, University of California San Diego

PUBLICATIONS

Yuheng Li, Kesong Yang, “High-Throughput Computational Design of Organic–Inorganic Hybrid Halide Semiconductors Beyond Perovskites for Optoelectronics”, *Energy Environ. Sci.*, 12, 2233-2243, 2019.

Yuheng Li, Daniel Maldonado-Lopez, Valeria Ríos Vargas, Jingning Zhang, Kesong Yang, “Stability Diagrams, Defect Tolerance, and Absorption Coefficients of Hybrid Halide Semiconductors: High-Throughput First-Principles Characterization”, *J. Chem. Phys.*, 152, 084106, 2020.

Yuheng Li, Kesong Yang, “High-Throughput Computational Design of Halide Perovskites and Beyond for Optoelectronics”, *WIREs Comput. Mol. Sci.*, e1500, 2020.

Yuheng Li, Maziar Behtash, Joseph Wong, Kesong Yang, “Enhancing Ferroelectric Dipole Ordering in Organic–Inorganic Hybrid Perovskite $\text{CH}_3\text{NH}_3\text{PbI}_3$: Strain and Doping Engineering”, *J. Phys. Chem. C*, 122, 177-184, 2018.

Yimu Chen, Yusheng Lei, Yuheng Li, Yugang Yu, Jinze Cai, Ming-Hui Chiu, Rahul Rao, Yue Gu, Chunfeng Wang, Woojin Choi, Hongjie Hu, Chonghe Wang, Yang Li, Jiawei Song, Jingxin Zhang, Baiyan Qi, Muyang Lin, Zhuorui Zhang, Ahmad E. Islam, Benji Maruyama, Shadi Dayeh, Lain-Jong Li, Kesong Yang, Yu-Hwa Lo, Sheng Xu, “Strain Engineering and Epitaxial Stabilization of Halide Perovskites”, *Nature*, 577, 209-215, 2020.

Yusheng Lei, Yimu Chen, Ruiqi Zhang, Yuheng Li, Qizhang Yan, Seunghyun Lee, Yugang Yu, Hsinhan Tsai, Woojin Choi, Kaiping Wang, Yanqi Luo, Yue Gu, Xinran Zheng, Chunfeng Wang, Chonghe Wang, Hongjie Hu, Yang Li, Baiyan Qi, Muyang Lin, Zhuorui Zhang, Shadi A. Dayeh, Matt Pharr, David P. Fenning, Yu-Hwa Lo, Jian Luo, Kesong Yang, Jinkyong Yoo, Wanyi Nie, Sheng Xu, “A Fabrication Process for Flexible Single-Crystal Perovskite Devices”, *Nature*, 583, 790-795, 2020.

Liyuan Wu, Pengfei Lu, Yuheng Li, Yan Sun, Joseph Wong, Kesong Yang, “First-Principles Characterization of Two-Dimensional $(\text{CH}_3(\text{CH}_2)_3\text{NH}_3)_2(\text{CH}_3\text{NH}_3)_{n-1}\text{Ge}_n\text{I}_{3n+1}$ Perovskite”, *J. Mater. Chem. A*, 6, 24389-24396, 2018.

ABSTRACT OF THE DISSERTATION

First-Principles Study of Hybrid Halide Perovskites and Beyond for Optoelectronic Applications

by

Yuheng Li

Doctor of Philosophy in NanoEngineering

University of California San Diego, 2020

Professor Kesong Yang, Chair

Organic-inorganic hybrid lead halide perovskites are promising for next-generation solar cells and light-emitting diodes, and it is of high demand to solve their critical issues and to understand their working mechanisms. In this dissertation, using first-principles calculations, we focus on design of stable and non-toxic alternatives to this class of materials, as well as to understand and optimize their structural, energetic, electronic, and ferroelectric properties for optoelectronic applications.

In the first project, we designed novel optoelectronic materials based on 24 perovskite-related prototype structures by high-throughput computing and data mining. Out of 4507 hybrid

halide compounds calculated, we selected 29 compounds adopting five prototype structures for light-emitting diodes and solar energy conversion. All these candidates show appropriate electronic properties and robust stability. The approach of exploring a large variety of prototype structures is transformative to computational design of other functional materials.

In the second project, we further investigated stability diagrams, defect tolerance, and optical absorption of the 29 hybrid halide compounds by high-throughput first-principles calculations. We calculated 2160 neutral and about 5000 charged defect structures to determine defect formation energies and transition energy levels for all possible point defects. Out of the 29 compounds, 15 candidates show high defect tolerance. This work provides detailed guidance on experimental investigation of these novel lead-free optoelectronic materials.

In the third project, we studied ferroelectric dipole ordering in hybrid perovskites. We found that organic cations' rotational energy barrier is dependent on the cell aspect ratio, and that spontaneous ferroelectric dipole ordering exists with small energy advantage. More importantly, we found that by increasing the cell aspect ratio, strain and doping can enhance the dipole ordering, which could boost electron-hole separations for photovoltaic applications.

In the fourth project, we studied strained epitaxial growth of halide perovskites. Our calculations demonstrate the epitaxial stabilization by calculating detailed thermodynamic terms in the epitaxial nucleation process. We also show that strains control the crystal structure, the bandgap, and the hole effective mass.

Chapter 1

Introduction

1.1 Lead Halide Perovskites

1.1.1 Promise in Optoelectronics

Lead halide perovskites have emerged as stellar next-generation materials for a wide range of optoelectronic applications, including solar cells, light-emitting diodes (LEDs), transistors, lasers, etc.¹⁻⁷ This class of materials has a common chemical formula of $APbX_3$, in which A is an organic cation (e.g. $CH_3NH_3^+ = MA^+$, $CH(NH_2)_2^+ = FA^+$) or a large inorganic cation (e.g. Cs^+) and X is a halide anion. They adopt the perovskite structures that consist of a three-dimensional framework of corner-sharing PbX_6 octahedra. Since the debut of $MAPbI_3$ and $MAPbBr_3$ as photovoltaic materials,¹ the power conversion efficiency (PCE) of lead halide perovskite solar cells have rapidly reached 25.2%.⁸ For light-emitting diodes, halide perovskites-based devices have achieved an external quantum efficiency (EQE) of over 20%.⁹ The success of this class of materials is largely attributed to their exceptional properties like proper and tunable band-gaps, large optical absorption coefficients, long diffusion lengths, small and balanced charge carrier effective masses, compositional flexibility, high defect tolerance, and low-temperature solution processability.¹⁰⁻¹⁸

1.1.2 Challenges

Despite their great promise in optoelectronic applications, there are great challenges in the way of real-world large-scale commercialization of halide perovskite optoelectronics.

On one hand, deep understandings of the working mechanism, especially atomic-scale origins of the energetic and electronic properties, have not been fully achieved for hybrid halide perovskites. For example, origins of the high PCEs of hybrid perovskites compared to their inorganic counterparts has not been fully understood.^{19–21} One of the most plausible arguments for their high efficiency is the ability of organic cations to form ferroelectric (FE) domains, which could help separate photo-generated electron-hole pairs in solar cells. However, the movement and ordering of organic cations is still controversial from both theoretical^{22–25} and experimental perspectives.^{26–31} Another example is that some metastable halide perovskites suffer from spontaneous phase transition to photoinactive competing phases, hindering their use in optoelectronic devices.⁶ It is helpful to understand the driving force of the phase transition and to explore stabilization methods. Open questions like these, broadly involving the structural, energetic, electronic, optical properties, etc., call for detailed theoretical investigations, and the answers are expected to provide guidance on improving the material properties and device performance for optoelectronic applications.

On the other hand, lead halide perovskites are confronted with two major problems that hinder their large-scale commercialization, namely low stability and toxicity of lead.^{10,32,33} One intrinsic solution to these problems is to find stable and lead-free alternatives that possess similar optoelectronic properties with lead halide perovskites.^{34–40} This solution requires comprehensive searches in large compositional and structural spaces, which would be too expensive in terms of time and cost for traditional trial-and-error experiments. Therefore, computational efforts are in demand for the design and discovery of effective lead halide perovskite alternatives.

1.2 High-Throughput Materials Design

As discussed above, first-principles calculations are in demand for intrinsic solutions to the stability and toxicity issues of lead halide perovskites. In recent years, high-throughput (HT) computational materials design has become an effective and efficient approach to the discovery of novel functional materials, thanks to the development of computation power. It has been applied in various materials for broad application areas, including topological insulators, thermoelectric materials, transparent conducting oxides, two-dimensional electron gas, heusler magnets, halide perovskite optoelectronic, etc.^{41–53} This approach uses first-principles calculations to build large-scale databases for existing and hypothetical materials, and promising candidate materials are then selected from the databases using data-driven methods. The selection process relies on materials descriptors that are computationally viable and accurately describe desired materials properties for target applications. Therefore, careful development of materials descriptors is the key to successful HT computational design. There are many well-developed software frameworks to assist the large-scale computation and data analysis in HT computational design. A few examples are AFLOW,⁵⁴ pymatgen,⁵⁵ the Atomic Simulation Environment,⁵⁶ and MatCloud.⁵⁷ There are also online materials databases built from first-principles calculations, including AFLOWLIB,⁵⁴ Materials Project,⁵⁸ Open Quantum Materials Database (OQMD),⁵⁹ and Computational Materials Repository.⁶⁰

The HT computational design approach has seen successful applications in the search of stable and nontoxic alternatives to lead halide perovskites for optoelectronic applications.⁶¹ Various HT studies have explored enormous compositional and structural spaces using different materials descriptors, calculation methodologies, and screening processes. It has become necessary to summarize these different studies and discuss the effective design principles to provide informative guidance for computational and experimental design of new materials. In addition, a large number of promising candidates designed from the HT studies need to be categorized for

the convenience of researchers in the broad field of halide perovskite optoelectronics to conduct further theoretical and experimental research as well as practical applications. Therefore, in this section, we overview common materials descriptors and their computational viability for halide perovskites and beyond for optoelectronics, which are vital for the HT computational design. In addition, we summarize selected candidates from previous HT studies in Table 1.1-1.4, as classified in terms of IVA element-based single perovskites, other element-based single perovskites, double perovskites, and perovskite derivatives.

1.2.1 Materials Properties and Materials Descriptors

Materials properties direct the design of specific classes of materials for specific applications. In the design of halide perovskite-like materials for optoelectronics, properties of stability and non-toxicity are considered for solving the common challenges faced by prototypical lead halide perovskites, and optical and electronic properties determine essential functionalities of materials in the optoelectronic applications. In HT computational design, materials properties are described using computationally viable descriptors. The descriptors filter a large calculated materials repository and select candidates with desired properties, playing critical roles in applying HT computational design in specific materials applications. In this section, we briefly review the desired materials properties for halide perovskites and beyond for optoelectronics, and how these properties are accessed through calculated descriptors in HT computational design.

Stability

Evaluating structural stability (or formability) of the perovskite structures for different chemical compositions has been one main screening process in many studies.⁶²⁻⁶⁴ There are empirical descriptors of octahedral factor $\mu = r_B/r_X$ and Goldshmidt tolerance factor $t = (r_A + r_X)/\sqrt{2}(r_B + r_X)$ that use ionic radii to predict the perovskite formability.⁶⁵ Recently, researchers have defined effective ionic radii for organic cations,^{66,67} and revised the Shannon radii for cations

in halide systems.^{68,69} In 2019, Bartel et al. proposed a new machine-learned tolerance factor $\tau = \frac{r_X}{r_B} - n_A \left(n_A - \frac{r_A/r_B}{\ln(r_A/r_B)} \right)$ that show higher prediction accuracy than the traditional t .⁷⁰ Notably, τ uses Shannon radii and change monotonically with perovskite formability.

High thermodynamic stability is essential for computationally predicted materials. It is especially important when designing alternative materials to the intrinsically unstable lead halide perovskites.⁷¹ In HT design, the descriptors of formation enthalpy (ΔH_f) and decomposition enthalpy (ΔH_d) are usually used.^{72,73} ΔH_f describes energy change from elemental component to compound, and positive values indicate unstable compounds. ΔH_d describes whether the compound tends to decompose into various elemental, binary, ternary, or more complex components, and negative values indicate unstable compounds. A rigorous determination of ΔH_d must consider all existing compounds in the Inorganic Crystal Structure Database (ICSD) and even hypothetical compounds as potential decomposition products and scrutinize all possible decomposition pathways to avoid overestimation of the thermodynamic stability.⁷⁴⁻⁷⁶ A comprehensive way to predict thermodynamic stability based on ΔH_d is to construct phase diagrams using the convex hull method.^{77,78}

Dynamic stability represents a more realistic evaluation of materials stability in the working environment. Computationally, phonon calculations⁷⁹ and *ab initio* molecular dynamics (AIMD)⁸⁰ are two main methods to assess materials' dynamic stability. In detail, the finite-temperature phonon spectrum can be calculated using density functional perturbation theory (DFPT), and imaginary frequencies in phonon spectrum indicate dynamical instability. AIMD calculations show total energy evolutions at finite temperature as a function of time, and also give crystal geometry change with time, from which the dynamic stability can be observed. These calculations are expensive in terms of time and cost and are usually performed only for pre-selected candidates in HT screening processes.

Optoelectronic properties

The bandgap is one of the most important electronic properties for optoelectronic materials because it directly determines how the materials interact with light (*e.g.* absorb or emit light). Bandgap energy determines the energy of the photons being emitted or absorbed, and the bandgap type determines whether phonons are required in the interactions with light. Different optoelectronic applications require different bandgap characteristics. The two most prevalent applications of halide perovskites serve as good examples. For photovoltaics, the optimal bandgap energy for single-junction solar cells is 1.34 eV according to the Shockley-Queisser (S-Q) detailed-balance model.^{81,82} Type of bandgap can be either direct or indirect for photovoltaics.⁷² For light-emitting, bandgap energy determines the photon energy for the desired color of light by the equation $E_{\text{photon}} = E_g + k_B T / 2$, and direct bandgap type is required for high emission efficiency.⁵ The calculation of bandgap energy has different levels of theory. The standard density functional theory (DFT) calculations using the Perdew–Burke–Ernzerhof (PBE)⁸³ functional within the generalized gradient approximation (GGA) is computationally efficient but severely underestimate bandgap energy, while hybrid functional within Heyd-Scuseria-Ernzerhof (HSE) formalism give more accurate results but are more time-consuming.⁸⁴ Spin-orbit coupling (SOC) is also very important in halide perovskite systems containing heavy elements.⁸⁵ Most HT studies screen materials on bandgaps calculated at GGA-PBE level and perform HSE and SOC calculations for a relatively small amount of candidates.

Electron and hole effective masses are directly related to their mobility. They are required to be small and balanced for efficient transport of photogenerated carriers in solar cell materials. In methylammonium lead iodide perovskite (MAPbI₃), effective masses of both electrons and holes are very small, granting the material long-range ambipolar transport property.⁸⁶ One method to determine effective masses is to fit calculated band structures near band edges using the equations $\frac{1}{m^*} = \frac{1}{\hbar^2} \frac{\partial^2 E}{\partial k^2}$. Visually, a more dispersive band indicates smaller effective mass. Another method is to calculate through the semiclassical Boltzmann transport theory.⁶² Interestingly,

Xiao et al. brought up the concept of electronic dimensionality, which can be used to understand isotropic/anisotropic current flow and different effective masses in materials.⁸⁷

Exciton binding energy is the energy needed to separate electron-hole pairs. A small exciton binding energy is beneficial for exciton separation into free carriers in photovoltaics, and a large one is beneficial for charge recombination to emit light. Exciton binding energy in HT computational studies is usually approximated using the hydrogen-like Wannier-Mott model, which sees it as an effective Rydberg: $E_B = \frac{\mu^* R_y}{m_0 \epsilon_r^2}$.^{62,88} In the equation, ϵ_r is the relative dielectric constant. It is usually adopted by the high-frequency limit of the dielectric constant (ϵ_∞) contributed by electronic polarization and calculated using finite-electric field and Berry-phase calculations.⁷²

Halide perovskites have extremely high optical absorption coefficients, which greatly contribute to their high efficiency as solar cell absorbers.^{65,89,90} The optical absorption coefficients can be calculated using the equation:⁹¹

$$\alpha(\omega) = \sqrt{2} \frac{\omega}{c} \sqrt{\sqrt{\epsilon_1(\omega)^2 + \epsilon_2(\omega)^2} - \epsilon_1(\omega)}, \quad (1.1)$$

where c is the speed of light, ω is the photon frequency, and $\epsilon_1(\omega)$ and $\epsilon_2(\omega)$ are the real part and imaginary part of the complex dielectric function. $\epsilon_1(\omega)$ and $\epsilon_2(\omega)$ can be calculated from ground-state electronic structure calculations.^{92,93} More accurate description of optical properties requires GW approximation and the Bethe-Salpeter equation (BSE),^{94,95} which are very time-consuming and usually beyond the scope of HT computational design.

Defect properties

Point defects could create non-radiative electron-hole recombination centers and deteriorate quantum efficiencies in solar cells and light emitters.¹⁶ Intrinsic point defects can be categorized into vacancies, interstitials, and antisites. Taking a typical A-M-X ternary system as

an example, there could be three types of vacancies (V_A , V_M , and V_X), three types of interstitials (A_i , M_i , and X_i), and six types of antisites (A_M , M_A , A_X , X_A , M_X , and X_M). These defects should be considered on all possible non-equivalent lattice sites when building models for calculations. In calculations, defect tolerance level of optoelectronic materials can be evaluated by calculating defect formation energy (E^f) and transition energy level ($\epsilon(q1/q2)$) (Equations 1.2 and 1.3, respectively).⁹⁶

$$E^f[X^q] = E_{tot}[X^q] - E_{tot}[bulk] - \sum_i n_i \mu_i + qE_F + E_{corr} \quad (1.2)$$

$$\epsilon(q1/q2) = \frac{E^f(X^{q1}; E_F = 0) - E^f(X^{q2}; E_F = 0)}{q2 - q1} \quad (1.3)$$

In the equations, X denotes a defect, q denotes a charge state, E_{tot} is total energy, μ is chemical potential, and E_F is Fermi energy. E_{corr} is a correction term based on different theories and methods, including image charge correction, potential alignment correction, band filling correction, etc.^{96–100} In a material, if defects with low formation energies do not create deep transition levels and defects that create deep levels have high formation energies, the material is defect tolerant and suitable for optoelectronic applications.⁹³ HT calculations of charged point defects are possible with reasonably sized supercells.^{62,93,101} There are also tools like PyCDT built for integrated point defect calculations.⁹⁹ Notably, linear and planar defects are usually out of the scope of HT computational studies.

1.2.2 Prior Predictions for Perovskite Optoelectronics

As discussed above, the key materials properties for optoelectronics are computationally accessible through descriptors. Therefore, it is viable to perform HT computational design of halide perovskites and beyond for optoelectronics. In Table 1.1-1.4, we summarize HT research examples classified by materials composition and structure of interest.

Table 1.1: List of compounds in the search space of IVA element-based single perovskites designed from high-throughput computational studies reviewed in this article: compound, lattice system, space group, lattice parameters, bandgap, and experimental validation. In this and the following tables: Symbols following compound formulas denote the specific optoelectronic applications predicted: circles (\circ) denote photovoltaic applications, triangles (\triangle) denote light-emitting applications, and no symbol means that the prediction was targeted for general optoelectronic applications. The lattice system and space group of most compounds refer to their assumed structures (starting from which the compounds were constructed), and their optimized structures do not always strictly belong to the same lattice system and space group, especially for organic-inorganic hybrid compounds. For lattice parameters and bandgap, the values calculated at the highest or most accurate level of theory in the reference are shown here. The experimental validation is not an exhaustive list. Note that, for each compound, synthesis of its structural isomer is not considered as its experimental validation.

Compound	Lattice system	Space group	Lattice parameters			E_g (eV)	Ref	Experimental validation
			a (Å)	b (Å)	c (Å)			
RbSnBr ₃ \circ	Cubic	–	5.87	5.87	5.87	2.26	102	103
CsSnBr ₃ \circ	Cubic	–	5.89	5.89	5.89	2.27	102	104
CsGeI ₃ \circ	Cubic	–	5.99	5.99	5.99	1.93	102	105
CsGeI ₃ \circ	Cubic	–	–	–	–	1.15	62	105
CsGeBr ₃ \circ	Cubic	–	–	–	–	1.64	62	106
HAGeBr ₃ \circ	Cubic	–	–	–	–	2.26	62	–
DAGeBr ₃ \circ	Cubic	–	–	–	–	2.47	62	–
MAGeI ₃ \circ	Cubic	–	6.10	6.10	6.10	1.98	62	–
CsSnI ₃ \circ	Cubic	–	–	–	–	0.95	62	107, 108
CsSnBr ₃ \circ	Cubic	–	–	–	–	1.53	62	104
CsSnCl ₃ \circ	Cubic	–	–	–	–	2.14	62	109
MASnI ₃ \circ	Cubic	–	6.26	6.26	6.26	1.26	62	107, 110, 111
MASnBr ₃ \circ	Cubic	–	–	–	–	2.00	62	111
FASnI ₃ \circ	Cubic	–	–	–	–	1.21	62	107, 112
EASnI ₃ \circ	Cubic	–	–	–	–	1.70	62	–
GASnI ₃ \circ	Cubic	–	–	–	–	1.78	62	–
DEASnI ₃ \circ	Cubic	–	–	–	–	1.62	62	–
CsSnI ₃ \circ	–	–	–	–	–	0.95	113	107, 108
FASnI ₃ \circ	–	–	–	–	–	1.00	113	107, 112
CsSnBr ₃ \circ	–	–	–	–	–	1.07	113	104
CsGeI ₃ \circ	–	–	–	–	–	1.28	113	105
MASnI ₃ \circ	–	–	–	–	–	1.43	113	107, 110, 111
CsGeBr ₃ \circ	–	–	–	–	–	1.56	113	106
MAGeI ₃ \circ	–	–	–	–	–	1.83	113	–
MASnBr ₃ \circ	–	–	–	–	–	1.89	113	111
MASiI ₃ \circ	–	–	–	–	–	1.44	113	–
MA _{0.75} Cs _{0.25} SnI ₃ \circ	–	–	–	–	–	1.20	114	–
MA _{0.875} Cs _{0.125} SnI ₃ \circ	–	–	–	–	–	1.18	114	–
MA _{0.75} Rb _{0.25} SnI ₃ \circ	–	–	–	–	–	1.21	114	–
FA _{0.5} Cs _{0.5} SnI ₃ \circ	–	–	–	–	–	1.11	114	–
FA _{0.5} Rb _{0.5} SnI ₃ \circ	–	–	–	–	–	1.12	114	–

Table 1.2: List of compounds in the search space of other element-based single perovskites designed from high-throughput computational studies reviewed in this article. For each other element-based single perovskite compound, experimental validation of its analogues with different A-site cations is also included. † The structural optimization started from five unique orthorhombic perovskite unit cells, and the resulting structures were not disclosed in reference. ‡ The bandgaps were given in color maps without explicit values.

Compound	Lattice system	Space group	Lattice parameters			E_g (eV)	Ref	Experimental validation
			a (Å)	b (Å)	c (Å)			
CsMgI ₃ ○	†	–	–	–	–	‡	115	–
CsVI ₃ ○	†	–	–	–	–	‡	115	–
CsMnI ₃ ○	†	–	–	–	–	‡	115	–
CsMnBr ₃ ○	†	–	–	–	–	‡	115	–
CsNiBr ₃ ○	†	–	–	–	–	‡	115	–
CsNiCl ₃ ○	†	–	–	–	–	‡	115	–
CsCdI ₃ ○	†	–	–	–	–	‡	115	–
CsCdBr ₃ ○	†	–	–	–	–	‡	115	–
CsCdCl ₃ ○	†	–	–	–	–	‡	115	–
CsHgBr ₃ ○	†	–	–	–	–	‡	115	–
CsHgCl ₃ ○	†	–	–	–	–	‡	115	–
CsHgF ₃ ○	†	–	–	–	–	‡	115	–
CsGaCl ₃ ○	†	–	–	–	–	‡	115	–
CsInBr ₃ ○	†	–	–	–	–	‡	115	116
CsInCl ₃ ○	†	–	–	–	–	‡	115	116
MACa _{0.5} Si _{0.5} I ₃ ○	Tetragonal	I4/mcm	12.2	12.4	12.3	1.33	117	–
MACa _{0.125} Si _{0.875} I ₃ ○	Tetragonal	I4/mcm	12.1	12.6	12.5	1.54	117	–
MAZn _{0.5} Si _{0.5} I ₃ ○	Tetragonal	I4/mcm	12.4	12.9	12.7	1.89	117	–
MAAuI ₃ ○	–	–	–	–	–	1.34	113	118
FAAuI ₃ ○	–	–	–	–	–	1.38	113	118
MAAuBr ₃ ○	–	–	–	–	–	1.39	113	–
KFeI ₃ ○	–	–	–	–	–	1.64	114	–
CsMn _{0.875} Fe _{0.125} I ₃ ○	–	–	–	–	–	1.33	114	–
CsMn _{0.75} Co _{0.25} I ₃ ○	–	–	–	–	–	1.50	114	–
MA _{0.5} Cs _{0.5} MnI ₃ ○	–	–	–	–	–	1.44	114	–

Table 1.3: List of compounds in the search space of double perovskites designed from high-throughput computational studies reviewed in this article. For each double perovskite compound, experimental validation of its analogues with different A-site cations is also included. \otimes denotes negative experimental validation. * denotes that the bandgaps were calculated for two different antiferromagnetic spin states.

Compound	Lattice system	Space group	Lattice parameters			E_g (eV)	Ref	Experimental validation
			a (Å)	b (Å)	c (Å)			
$\text{Cs}_2\text{CuSbCl}_6$ \circ	Cubic	$\text{Fm}\bar{3}\text{m}$	10.52	10.52	10.52	1.82	73	\otimes ⁷⁵
$\text{Cs}_2\text{CuSbBr}_6$ \circ	Cubic	$\text{Fm}\bar{3}\text{m}$	11.07	11.07	11.07	1.24	73	\otimes ⁷⁵
$\text{Cs}_2\text{CuBiBr}_6$ \circ	Cubic	$\text{Fm}\bar{3}\text{m}$	11.17	11.17	11.17	1.51	73	\otimes ⁷⁵
$\text{Cs}_2\text{AgSbBr}_6$ \circ	Cubic	$\text{Fm}\bar{3}\text{m}$	11.37	11.37	11.37	1.67	73	119
$\text{Cs}_2\text{AgSbI}_6$ \circ	Cubic	$\text{Fm}\bar{3}\text{m}$	12.13	12.13	12.13	0.95	73	120
$\text{Cs}_2\text{AgBiI}_6$ \circ	Cubic	$\text{Fm}\bar{3}\text{m}$	12.24	12.24	12.24	1.32	73	121, 122
$\text{Cs}_2\text{AuSbCl}_6$ \circ	Cubic	$\text{Fm}\bar{3}\text{m}$	10.83	10.83	10.83	1.05	73	–
$\text{Cs}_2\text{AuBiCl}_6$ \circ	Cubic	$\text{Fm}\bar{3}\text{m}$	10.94	10.94	10.94	1.38	73	–
$\text{Cs}_2\text{AuBiBr}_6$ \circ	Cubic	$\text{Fm}\bar{3}\text{m}$	11.42	11.42	11.42	0.84	73	–
$\text{Cs}_2\text{InSbCl}_6$ \circ	Cubic	$\text{Fm}\bar{3}\text{m}$	11.32	11.32	11.32	1.02	73	\otimes ⁷⁴
$\text{Cs}_2\text{InBiCl}_6$ \circ	Cubic	$\text{Fm}\bar{3}\text{m}$	11.44	11.44	11.44	0.91	73	\otimes ⁷⁴
$\text{Cs}_2\text{AgInBr}_6$ \circ	Cubic	$\text{Fm}\bar{3}\text{m}$	11.156	11.156	11.156	1.5	123	124
$\text{Rb}_2\text{AgInBr}_6$ \circ	Cubic	$\text{Fm}\bar{3}\text{m}$	11.064	11.064	11.064	1.46	123	124
$\text{Rb}_2\text{CuInCl}_6$ \circ	Cubic	$\text{Fm}\bar{3}\text{m}$	10.237	10.237	10.237	1.36	123	\otimes ⁷⁵
$\text{Cs}_2\text{BiAg}_{0.875}\text{Cu}_{0.125}\text{Cl}_6$ \circ	Cubic	$\text{Fm}\bar{3}\text{m}$	–	–	–	1.9	77	–
$\text{Cs}_2\text{BiAg}_{0.75}\text{Cu}_{0.25}\text{Cl}_6$ \circ	Cubic	$\text{Fm}\bar{3}\text{m}$	–	–	–	1.6	77	–
$\text{Cs}_2\text{AgInBr}_6$ \circ	Cubic	$\text{Fm}\bar{3}\text{m}$	11.16	11.16	11.16	1.49	63	124
$\text{Cs}_2\text{InAsBr}_6$ \circ	Cubic	$\text{Fm}\bar{3}\text{m}$	11.43	11.43	11.43	0.36	63	–
$\text{Cs}_2\text{InBiCl}_6$ \circ	Cubic	$\text{Fm}\bar{3}\text{m}$	11.42	11.42	11.42	0.92	63	\otimes ⁷⁴
$\text{Cs}_2\text{InBiBr}_6$ \circ	Cubic	$\text{Fm}\bar{3}\text{m}$	11.89	11.89	11.89	0.29	63	\otimes ⁷⁴
$\text{Cs}_2\text{InSbBr}_6$ \circ	Cubic	$\text{Fm}\bar{3}\text{m}$	11.76	11.76	11.76	0.33	63	\otimes ⁷⁴
$\text{Cs}_2\text{TlAsBr}_6$ \circ	Cubic	$\text{Fm}\bar{3}\text{m}$	11.58	11.58	11.58	1.23	63	–
$\text{Cs}_2\text{TlAsI}_6$ \circ	Cubic	$\text{Fm}\bar{3}\text{m}$	12.34	12.34	12.34	0.79	63	–
$\text{Cs}_2\text{TlSbBr}_6$ \circ	Cubic	$\text{Fm}\bar{3}\text{m}$	11.90	11.90	11.90	1.11	63	–

TABLE 1.3 Continued

Compound	Lattice system	Space group	Lattice parameters			E_g (eV)	Ref	Experimental validation
			a (Å)	b (Å)	c (Å)			
$\text{Cs}_2\text{InGaI}_6$ ○	Cubic	$\text{Fm}\bar{3}\text{m}$	12.14	12.14	12.14	0.76	63	–
$\text{Cs}_2\text{InInBr}_6$ ○	Cubic	$\text{Fm}\bar{3}\text{m}$	11.63	11.63	11.63	1.57	63	–
$\text{Cs}_2\text{TlTlBr}_6$ ○	Cubic	$\text{Fm}\bar{3}\text{m}$	11.74	11.74	11.74	1.07	63	–
$\text{Cs}_2\text{NaMnCl}_6$	Cubic	$\text{Fm}\bar{3}\text{m}$	–	–	–	2.69/2.96*	64	–
$\text{Cs}_2\text{KMnCl}_6$	Cubic	$\text{Fm}\bar{3}\text{m}$	–	–	–	3.30/3.30*	64	–
$\text{Cs}_2\text{NaNiCl}_6$	Cubic	$\text{Fm}\bar{3}\text{m}$	–	–	–	1.78/2.08*	64	–
$\text{Cs}_2\text{KNiCl}_6$	Cubic	$\text{Fm}\bar{3}\text{m}$	–	–	–	2.44/2.48*	64	–
$\text{Cs}_2\text{GeSnI}_6$ ○	–	–	–	–	–	1.04	113	–
$\text{MA}_2\text{SiSnI}_6$ ○	–	–	–	–	–	1.22	113	–
$\text{FA}_2\text{GeSnI}_6$ ○	–	–	–	–	–	1.24	113	–
$\text{Cs}_2\text{GeSnBr}_6$ ○	–	–	–	–	–	1.29	113	–
$\text{MA}_2\text{GeSnI}_6$ ○	–	–	–	–	–	1.56	113	–
$\text{FA}_2\text{SiGeI}_6$ ○	–	–	–	–	–	1.66	113	–
$\text{MA}_2\text{SiGeI}_6$ ○	–	–	–	–	–	1.82	113	–
$\text{MA}_2\text{InBiI}_6$ ○	–	–	–	–	–	0.88	113	⊗ ⁷⁴
$\text{MA}_2\text{InSbI}_6$ ○	–	–	–	–	–	1.01	113	⊗ ⁷⁴
$\text{FA}_2\text{GaBiI}_6$ ○	–	–	–	–	–	1.10	113	–
$\text{MA}_2\text{GaBiI}_6$ ○	–	–	–	–	–	1.16	113	–
$\text{MA}_2\text{InBiBr}_6$ ○	–	–	–	–	–	1.18	113	⊗ ⁷⁴
$\text{FA}_2\text{InBiI}_6$ ○	–	–	–	–	–	1.19	113	⊗ ⁷⁴
$\text{MA}_2\text{GaSbI}_6$ ○	–	–	–	–	–	1.21	113	–
$\text{Cs}_2\text{GaBiI}_6$ ○	–	–	–	–	–	1.21	113	–
$\text{Cs}_2\text{GaBiBr}_6$ ○	–	–	–	–	–	1.29	113	–
$\text{MA}_2\text{InSbBr}_6$ ○	–	–	–	–	–	1.29	113	⊗ ⁷⁴
$\text{Cs}_2\text{GaBiCl}_6$ ○	–	–	–	–	–	1.39	113	–
$\text{Cs}_2\text{GaSbCl}_6$ ○	–	–	–	–	–	1.43	113	–
$\text{Cs}_2\text{InBiBr}_6$ ○	–	–	–	–	–	1.45	113	⊗ ⁷⁴

TABLE 1.3 Continued

Compound	Lattice system	Space group	Lattice parameters			E_g (eV)	Ref	Experimental validation
			a (Å)	b (Å)	c (Å)			
MA ₂ GaPBr ₆ ○	–	–	–	–	–	1.64	113	–
MA ₂ GaBiBr ₆ ○	–	–	–	–	–	1.72	113	–
MA ₂ GaSbBr ₆ ○	–	–	–	–	–	1.77	113	–
MA ₂ AgAuBr ₆ ○	–	–	–	–	–	1.27	113	–
MA ₂ CuAuBr ₆ ○	–	–	–	–	–	1.29	113	⊗ ⁷⁵
MA ₂ CuAuI ₆ ○	–	–	–	–	–	1.30	113	⊗ ⁷⁵
FA ₂ AgAuI ₆ ○	–	–	–	–	–	1.35	113	–
Cs ₂ RhInI ₆ ○	–	–	–	–	–	1.42	113	–
FA ₂ RhInI ₆ ○	–	–	–	–	–	1.63	113	–
MA ₂ RhGaI ₆ ○	–	–	–	–	–	1.67	113	–
Cs ₂ RhGaI ₆ ○	–	–	–	–	–	1.68	113	–
Cs ₂ RhInBr ₆ ○	–	–	–	–	–	1.76	113	–
MA ₂ RhInBr ₆ ○	–	–	–	–	–	1.83	113	–
MA ₂ CuInI ₆ ○	–	–	–	–	–	1.29	113	⊗ ⁷⁵
FA ₂ AuGaI ₆ ○	–	–	–	–	–	1.44	113	–
MA ₂ AuInI ₆ ○	–	–	–	–	–	1.47	113	–
MA ₂ AuGaI ₆ ○	–	–	–	–	–	1.50	113	–
MA ₂ AgBiI ₆ ○	–	–	–	–	–	2.09	113	–
MA ₂ CuBiI ₆ ○	–	–	–	–	–	2.11	113	⊗ ⁷⁵
DMAAg _{0.5} Bi _{0.5} I ₃ ○	–	–	–	–	–	1.53	114	121, 122
FAAg _{0.5} Sb _{0.5} Br ₃ ○	–	–	–	–	–	1.56	114	119

1.3 Summary

Organic-inorganic hybrid lead halide perovskites have emerged as stellar materials for next-generation optoelectronics, but solutions to their critical issues and deep understanding

Table 1.4: List of compounds in the search space of perovskite derivatives designed from high-throughput computational studies reviewed in this article. For each perovskite-derived compound, experimental validation of its analogues with different A-site cations is also included.

Compound	Lattice system	Space group	Lattice parameters			E_g (eV)	Ref	Experimental validation
			a (Å)	b (Å)	c (Å)			
RbSbI ₄	Rhombohedral	R3c	–	–	–	2.34	125	–
CsSbI ₄	Rhombohedral	R3c	–	–	–	2.34	125	–
K ₃ Sb ₂ I ₉	Hexagonal	P $\bar{3}$ m1	–	–	–	2.04	125	126
Rb ₃ Sb ₂ I ₉	Hexagonal	P $\bar{3}$ m1	–	–	–	2.07	125	126
Cs ₃ Sb ₂ I ₉	Hexagonal	P $\bar{3}$ m1	–	–	–	2.13	125	126
Rb ₃ In ₂ I ₉	Hexagonal	P6 ₃ /mmc	–	–	–	2.05	125	–
Cs ₃ In ₂ I ₉	Hexagonal	P6 ₃ /mmc	–	–	–	2.12	125	–
Cs ₃ Ga ₂ I ₉	Hexagonal	P6 ₃ /mmc	–	–	–	1.72	125	–
Cs ₄ SnSb ₂ I ₁₂ ○	Monoclinic	C2/m	8.72	8.72	15.13	1.50	127	–
Cs ₄ GeSb ₂ I ₁₂ ○	Monoclinic	C2/m	8.61	8.61	14.93	1.60	127	–
K ₄ SnSb ₂ Cl ₁₂	Monoclinic	C2/m	–	–	–	2.63	128	–
K ₄ SnBi ₂ Cl ₁₂	Monoclinic	C2/m	–	–	–	2.54	128	–
K ₄ SnSb ₂ Br ₁₂	Monoclinic	C2/m	–	–	–	2.17	128	–
Rb ₄ SnSb ₂ Cl ₁₂	Monoclinic	C2/m	–	–	–	2.45	128	–
Rb ₄ SnBi ₂ Cl ₁₂	Monoclinic	C2/m	–	–	–	2.43	128	–
Rb ₄ SnSb ₂ Br ₁₂	Monoclinic	C2/m	–	–	–	2.07	128	–
MA ₂ GeBr ₄ △	Tetragonal	I4/mmm	5.54	5.54	19.02	1.99	72, 93	–
MA ₂ GeI ₄ ○△	Tetragonal	I4/mmm	5.94	5.87	20.11	1.66	72, 93	–
MA ₂ SnCl ₄ △	Tetragonal	I4/mmm	5.56	5.48	18.35	2.49	72, 93	–
MA ₂ SnBr ₄ ○△	Tetragonal	I4/mmm	5.72	5.74	19.08	1.67	72, 93	–
MA ₂ SnI ₄ ○	Tetragonal	I4/mmm	6.12	6.11	20.00	1.42	72, 93	–
FA ₂ SnBr ₄ ○△	Tetragonal	I4/mmm	5.64	5.71	20.60	1.69	72, 93	–
AD ₂ GeI ₄ △	Tetragonal	I4/mmm	6.14	6.16	18.97	2.30	72, 93	–
AD ₂ SnBr ₄ △	Tetragonal	I4/mmm	5.87	5.86	18.09	2.51	72, 93	–
AD ₂ SnI ₄ ○△	Tetragonal	I4/mmm	6.22	6.21	19.17	1.87	72, 93	–
MA ₃ In ₂ I ₉ △	Hexagonal	P $\bar{3}$ m1	8.23	8.31	11.00	2.18	72, 93	–
MA ₃ Sb ₂ Br ₉ △	Hexagonal	P $\bar{3}$ m1	7.71	7.71	10.37	2.70	72, 93	–
MA ₃ Sb ₂ I ₉ ○△	Hexagonal	P $\bar{3}$ m1	8.26	8.26	10.91	2.02	72, 93	129, 130
MA ₃ Bi ₂ I ₉ ○	Hexagonal	P $\bar{3}$ m1	8.35	8.35	11.00	1.82	72, 93	–
FA ₃ Ga ₂ I ₉ △	Hexagonal	P $\bar{3}$ m1	7.94	8.25	11.83	2.17	72, 93	–
FA ₃ In ₂ Br ₉ △	Hexagonal	P $\bar{3}$ m1	7.38	7.83	11.17	2.91	72, 93	–
FA ₃ In ₂ I ₉ △	Hexagonal	P $\bar{3}$ m1	8.04	8.30	11.67	1.90	72, 93	–
FA ₃ Bi ₂ I ₉ ○△	Hexagonal	P $\bar{3}$ m1	8.06	8.36	11.60	1.80	72, 93	131
AD ₃ Sb ₂ Br ₉ △	Hexagonal	P $\bar{3}$ m1	8.30	8.36	9.55	2.52	72, 93	–
AD ₃ Sb ₂ I ₉ ○△	Hexagonal	P $\bar{3}$ m1	8.69	8.77	10.20	1.91	72, 93	129, 130
AD ₃ Bi ₂ I ₉ ○	Hexagonal	P $\bar{3}$ m1	8.78	8.84	10.26	1.80	72, 93	–
FA ₃ Sb ₂ I ₉ △	Hexagonal	P6 ₃ /mmc	8.02	8.32	23.18	2.54	72, 93	132, 133
AD ₃ In ₂ I ₉ △	Hexagonal	P6 ₃ /mmc	8.61	8.71	20.54	2.00	72, 93	–
MA ₂ ZrI ₆ △	Tetragonal	I4/mmm	8.18	8.19	12.37	2.60	72, 93	–
AD ₂ HfI ₆ △	Tetragonal	I4/mmm	8.47	8.46	12.17	2.89	72, 93	–
AD ₂ SnBr ₆ △	Tetragonal	I4/mmm	8.13	8.12	11.56	2.42	72, 93	–
AD ₂ TeBr ₆ △	Tetragonal	I4/mmm	8.29	8.30	11.18	2.71	72, 93	–
MA ₂ SnI ₆ ○	Cubic	Fm $\bar{3}$ m	11.61	11.44	12.55	0.80	72, 93	134, 135
MA ₂ TeI ₆ ○	Cubic	Fm $\bar{3}$ m	11.67	11.51	12.58	1.77	72, 93	134
AD ₂ TeI ₆ ○	Cubic	Fm $\bar{3}$ m	12.54	11.63	12.17	1.87	72, 93	–

of their atomic-scale mechanisms require further first-principles computational studies. With the goals of materials design, understanding, and optimization, we discuss our high-throughput approaches and individual material properties investigation of halide perovskites and beyond for optoelectronic applications. In Chapter 2, we demonstrate a unique high-throughput approach to the discovery of stable hybrid halide perovskites and derivatives for solar cells and light-emitting diodes. In Chapter 3, we investigated stability diagrams, defect tolerance, and optical absorption of the selected hybrid halide compounds. In Chapter 4, we investigate spontaneous ferroelectric dipole ordering of MA cations in MAPbI_3 and strain and doping as tools to enhance the ordering. In Chapter 5, we investigate epitaxial stabilization and strain effects in strained epitaxial growth of $\alpha\text{-FAPbI}_3$. Finally, in chapter 6, we provide our perspectives and outlook on high-throughput design of perovskite-related optoelectronics, and we summarize the results and conclusions in this dissertation.

Chapter 2

High-Throughput Computational Design of Organic-Inorganic Hybrid Halide Semiconductors beyond Perovskites for Optoelectronics

As introduced in Chapter 1, organic-inorganic lead halide perovskites show great promise in optoelectronic applications such as light-emitting diodes and solar energy conversion. However, the poor stability and toxicity of lead halide perovskites severely limit their large-scale applications. In this chapter, we show a high-throughput design of lead-free hybrid halide semiconductors with robust materials stability and desired material properties beyond perovskites. On the basis of 24 prototype structures that include perovskite and non-perovskite structures and several typical organic cations, a comprehensive quantum materials repository that contains 4507 hypothetical hybrid compounds was built using large-scale first-principles calculations. After a high-throughput screening of this repository, we have rapidly identified 23 candidates for light-emitting diodes and 13 candidates for solar energy conversion. Our work demonstrates a new avenue to design of

novel organic-inorganic functional materials by exploring a great variety of prototype structures.

2.1 Introduction

Organic-inorganic hybrid lead halide perovskites with a prototypical formula of MAPbI_3 ($\text{MA}=\text{CH}_3\text{NH}_3$) are one emerging class of semiconductor materials with promising optoelectronic applications including solar energy conversion and light-emitting diodes.^{1,5} This is mainly attributed to their excellent materials properties such as tunable band gaps¹³⁶, high charge carrier mobility¹⁴, defect tolerance¹⁷, and low-temperature solution processability¹⁸. In spite of their promising optoelectronic applications, particularly for solar energy conversion, the hybrid lead halide perovskites are facing two major challenges including poor stability and presence of toxic lead, which limits their large-scale applications.^{32,33} To overcome these challenges, one solution is to search for novel hybrid materials with potentially superior properties beyond or like that of lead-based hybrid halide perovskites.

Some prior experimental and computational efforts both have been made to explore alternatives to lead halide perovskites. There are two major classes of candidates that are being extensively studied. One class of candidates are Ge- and Sn-based halide perovskites with various organic cations, but these materials usually have even lower stability than lead halide perovskites.⁶² To enhance stability of Sn-based perovskites, some experimental approaches such as the fabrication of low-dimensional structures¹³⁷ and the encapsulation of device¹³⁸ have been proposed. In addition to Ge and Sn, Si mixed with other cations such as Ca/Si and Zn/Si with different ratios were also tried.¹¹⁷ The other class of candidates are called double perovskites with a chemical formula $\text{A}_2\text{BB}'\text{X}_6$ ($\text{A}=\text{Cs}$ or organic cations; $\text{X}=\text{Cl}$, Br , or I), which can be regarded as derivatives of single perovskite MAPbX_3 but with Pb replaced by two different metal cations ($\text{B}=\text{B}^+$; $\text{B}'=\text{B}^{3+}$).^{73,113,123,139–142} Early experimental demonstration of double perovskites for optoelectronics include Cs-based inorganic double perovskites with Ag-Bi composition^{139–141}

and the MA-based hybrid double perovskite with K-Bi composition.¹⁴² Nevertheless, most double perovskites that are predicted to have good electronic properties often suffer from instability issues such as phase separation or redox decomposition, *e.g.*, $\text{Cs}_2\text{InBiCl}_6$ and $\text{Cs}_2\text{InSbCl}_6$,⁷⁴ while double perovskites that can be synthesized usually show large indirect band gaps.^{139–142} Despite this, extensive research efforts are being made to search for novel double perovskites with desired electronic properties and high stability, such as using high-throughput materials design approach,^{73,113,123} towards lead-free perovskite optoelectronics.^{39,143,144}

Notably, these prior efforts primarily focused on the single perovskite structure with a stoichiometry of 1:1:3 or on the double perovskite with a stoichiometry of 2:1:1:6. Besides perovskite structures, there exist in principles other organic-inorganic hybrid ternary metal halide compounds with appropriate metal elements and the stoichiometry of component elements that are more stable and even show better optoelectronic properties than the typical perovskite structures.³⁷ As a proof of concept, Sb-based hybrid ternary compound, $(\text{MA})_3\text{Sb}_2\text{Cl}_x\text{I}_{9-x}$, has been prepared, and the solar cell based on this material reached a power conversion efficiency over 2%;¹⁴⁵ the ternary silver bismuth iodides showed tunable optoelectronic properties upon sulfide modification for photovoltaics.¹⁴⁶ Therefore, it is worthwhile to explore non-perovskite ternary structures for searching for alternatives to lead halide perovskites.

In this work, we have carried out a high-throughput computational design of novel lead-free organic-inorganic ternary halide semiconductors for optoelectronic applications using large-scale first-principles electronic structure calculations and have successfully identified 13 candidates for photovoltaic applications and 23 candidates for light-emitting applications. The chemical formulas of selected candidates include A_2BX_4 , $\text{A}_3\text{B}_2\text{X}_9$, and A_2BX_6 , in which A = MA, FA, or AD, and X=Cl, Br, or I. All these candidates have robust materials stability, appropriate band gaps, effective masses, and exciton binding energies for the optoelectronic applications.

2.2 Methods

The high-throughput first-principles calculations were performed using the automatic framework AFLOW¹⁴⁷ based on the Vienna *Ab-initio* Simulation Package (VASP).¹⁴⁸ The projector augmented wave potentials, and the generalized gradient approximation (GGA) of the exchange-correlation functional as parameterized by Perdew, Burek, and Ernzerhof (PBE) are used in the DFT calculations.¹⁴⁹ To properly describe the long-range dispersion interactions between the organic molecules in the hybrid materials, two types of van der Waals (vdW) functionals including DFT-D3¹⁵⁰ and optB86b¹⁵¹ were carefully assessed for the prototype compound MASnBr_3 , along with the standard PBE functional. As shown in Table A.1 of Appendix A, our test calculations suggest that both vdW functionals give more accurate equilibrium lattice parameters than the PBE functional while the DFT-D3 method shows a better match with the experimental value than the optB86b and thus is used in our calculations. Structures are fully relaxed with a convergence tolerance of 0.01 meV/atom. k -points grid of 0.05 \AA^{-1} were automatically set for relaxation of different structures. Accurate charge densities and density of states are obtained in static calculations with a denser grid of 0.04 \AA^{-1} . Other computational settings such as cutoff energy are managed by the AFLOW code that also generates appropriate entries for the structural relaxation, static calculations, and the electronic band structure calculations sequentially and automatically.¹⁴⁷ The hybrid DFT calculations within Heyd-Scuseria-Ernzerhof (HSE) formalism with 25% Hartree-Fock (HF) exchange are employed to predict accurate band gaps for the candidate compounds.^{152,153} The parameter of 25% HF mixing constant was derived from perturbation theory,^{152,153} which can generally yield close band gaps to the experiment and is appropriate for a large number and variety of hypothetical compounds.^{73,123}

2.3 Results

2.3.1 Building Repository

Table 2.1: Structural properties of the $\text{Cs}_x\text{B}_y\text{X}_z$ compounds used to extract prototype structures. Original inorganic compound, space group, ICSD number, and Pearson symbol. All the prototype structures are available in the AFLOWLIB and/or Materials Project.

B^{+n}	Stoichiometry	Original Compound	Space Group	ICSD Number	Pearson Symbol
B^{+1}	1:1:2	$\text{Cs}_4\text{Ag}_4\text{Br}_8$	Cmcm	150301	oS16
		$\text{Cs}_2\text{Ag}_2\text{Cl}_4$	P4/nmm	150300	tP8
B^{+2}	1:2:3	$\text{Cs}_4\text{Cu}_8\text{Br}_{12}$	Cmcm	49613	oS24
		$\text{Cs}_1\text{Sn}_1\text{Br}_3$	$\text{Pm}\bar{3}\text{m}$	4071	cP5
		$\text{Cs}_1\text{Ge}_1\text{Br}_3$	R3m	80317	hR5
	1:1:3	$\text{Cs}_3\text{Mn}_3\text{Cl}_9$	$\text{R}\bar{3}\text{m}$	2555	hR15
		$\text{Cs}_4\text{Ag}_4\text{Cl}_{12}$	I4/mmm	66067	tI20
		$\text{Cs}_2\text{Cd}_2\text{Br}_6$	$\text{P}6_3\text{mc}$	281176	hP10
		$\text{Cs}_2\text{Dy}_2\text{Br}_6$	P4/mbm	300285	tP10
		$\text{Cs}_4\text{Cr}_4\text{I}_{12}$	Pbcn	23383	oP20
		$\text{Cs}_4\text{Sn}_4\text{I}_{12}$	$\text{P}2_1/\text{m}$	14070	mP20
	2:1:4	$\text{Cs}_4\text{Cr}_4\text{Cl}_{12}$	C2/m	41802	mS20
		$\text{Cs}_4\text{Pb}_4\text{I}_{12}$	Pnma	161480	oP20'
		$\text{Cs}_4\text{Cd}_2\text{Cl}_8$	I4/mmm	16576	tI14
		$\text{Cs}_8\text{Pd}_4\text{Cl}_{16}$	Cmmm	95812	oS28
		$\text{Cs}_4\text{Hg}_2\text{I}_8$	$\text{P}2_1/\text{m}$	63110	mP14
	2:3:8	$\text{Cs}_8\text{Zn}_4\text{Br}_{16}$	Pnma	69139	oP28
$\text{Cs}_4\text{Hg}_6\text{I}_{16}$		Cm	4074	mS26	
$\text{Cs}_2\text{Hg}_4\text{Br}_{10}$		$\text{P}2_1/\text{m}$	200751	mP16	
B^{+3}	3:2:9	$\text{Cs}_3\text{Bi}_2\text{Br}_9$	$\text{P}\bar{3}\text{m}1$	1142	hP14
		$\text{Cs}_6\text{Mo}_4\text{Br}_{18}$	$\text{P}6_3/\text{mmc}$	26213	hP28
B^{+4}	2:1:6	$\text{Cs}_4\text{Pd}_2\text{I}_{12}$	I4/mmm	280189	tI18
		$\text{Cs}_8\text{Pt}_4\text{Br}_{24}$	$\text{Fm}\bar{3}\text{m}$	77381	cF36
		Cs_2CeCl_6	$\text{P}\bar{3}\text{m}1$	14339	hP9

As the first step, we built a quantum materials repository that contains hybrid halide

perovskites and perovskite derivatives. To do this, we began by identifying all possible prototype structures based on existing ternary metal halide compounds with a formula of $Cs_xB_yX_z$ from the online quantum materials databases AFLOWLIB⁵⁴ and Materials Project.⁵⁸ The reason for selecting Cs-contained compounds is as follows. The Cs cation has a large ionic radius that is comparable with that of the organic cations such as MA, and thus it can be readily substituted by organic cations to form organic-inorganic hybrid compounds. Note that one chemical formula may correspond to different crystal structures, and only the most stable one was selected as a prototype structure. As shown in Fig. A.1 of Appendix A, a total number of 24 unique prototype structures were identified. Their complete structural information is listed in Table 2.1, including space group, ICSD number, and Pearson symbol. The unique Pearson symbol is used to denote these prototype structures. For example, the structure generated from the compound $CsSnBr_3$ with a space group of $Pm\bar{3}m$ and an ICSD number of 4071 (identified as $CsSnBr_3_ICSD_4071$ in AFLOWLIB) is denoted using its Pearson symbol of cP5. The prototype structures cP5 and tI20 (tP10) are the cubic and tetragonal perovskites, respectively, and the others are perovskite derivatives. Note that two prototypes, $CsCrI_3_ICSD_23383$ and $CsPbI_3_ICSD_161480$, share the same Pearson symbol of oP20, and to distinguish them, we denote the former with oP20, and the later with oP20'.

After identifying the structure prototypes, we next generate hypothetical compounds by placing various elements in the $A_xB_yX_z$ formula. At A site, we put relatively small organic cations, including MA (CH_3NH_3), FA ($CH(NH_2)_2$), AD ($((CH_2)_2NH_2)$)¹⁵⁴, DMA ($NH_2(CH_3)_2$), and EA ($C_2H_5NH_3$). At B site, we select elements with different valence states according to the different stoichiometry of $A_xB_yX_z$. As shown in Table 2.1, there are three structure prototypes for B^+ , 16 prototypes for B^{2+} , two prototypes for B^{3+} , and three prototypes for B^{4+} . B^+ -based prototypes have two different stoichiometries (A:B:X=1:1:2 and 1:2:3); B^{2+} -based prototypes have four different stoichiometries (A:B:X=1:1:3, 2:1:4, 2:3:8, and 1:2:5); B^{3+} -based prototypes only have one stoichiometry (A:B:X=3:2:9); and B^{4+} -based prototypes also only have one stoichiometry

(A:B:X=2:1:6). A total number of 65 possible B-site elements with common valence states from +1 to +4 were placed in the corresponding prototypes. The X site is occupied by I, Br, or Cl ions. With the three sites combined in the 24 prototypes, a total number of 4507 hypothetical compounds were generated. The electronic structure of all the compounds is computed in a high-throughput fashion.

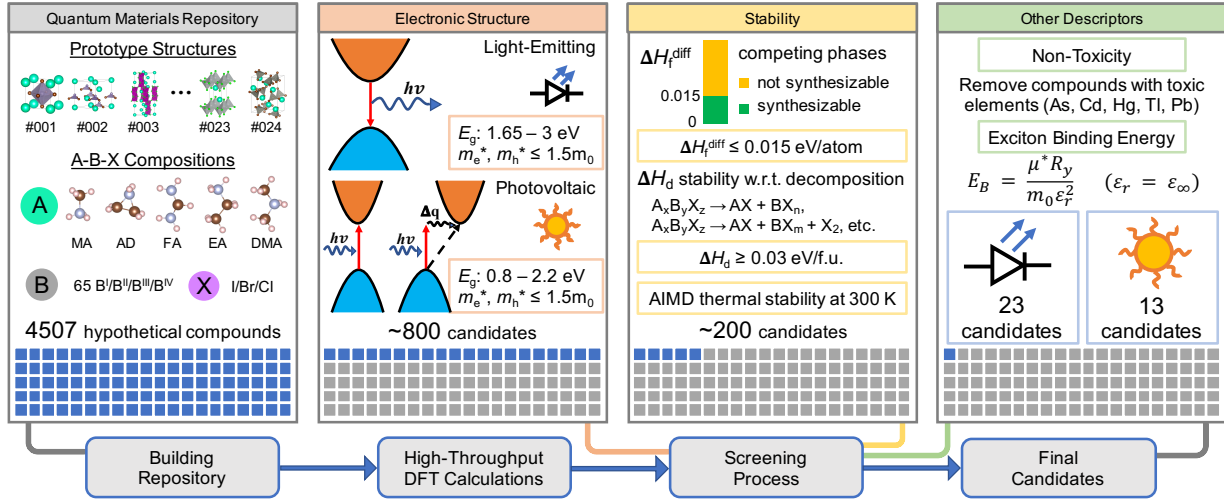


Figure 2.1: Schematic diagram of the high-throughput screening process. A total number of 4507 compounds ($A_xB_yX_z$, $A = \text{MA/FA/AD/EA/DMA}$, $X = \text{I/Br/Cl}$) were generated from 65 kinds of B-site elements in 24 different crystal structures. Compounds with direct band gaps in the visible spectrum range are kept for light-emitting materials, and compounds with band gaps in 0.8-2.2 eV are kept for solar-cell materials. Compounds with effective masses greater than $1.5m_0$ are excluded. Compounds with a formation enthalpy higher than its most energetically favorable competing phase by a value greater than 0.015 eV/atom are excluded. Compounds containing toxic B-site elements are also excluded. Compounds that cannot maintain structural integrity at room temperature are excluded. The selected candidates are all stable with respect to decomposition by at least 0.03 eV/formula unit. Compounds with exciton binding energy greater than 130 meV are excluded for solar-cell materials. 23 candidates for light-emitting materials and 13 candidates for solar-cell materials were selected.

2.3.2 Screening Process

In terms of optoelectronic applications like solar cells and light emitters, there are several common descriptors often used for high-throughput screening of target materials. These descriptors include band gap, charge carrier effective masses, and decomposition enthalpy. Our detailed

criteria for each descriptor are discussed as below:

(i) Band gap (E_g). We obtained band gaps using DFT calculations with two different types of functionals: One is calculated with the standard GGA functional (E_g^{GGA}), and the other is calculated with the hybrid functionals (E_g^{HSE})¹⁵². This is because the GGA functional often underestimate band gaps, thus E_g^{GGA} can only serve as a rough reference for screening; while E_g^{HSE} is much closer to the experimental value, as shown from previous calculations on halide perovskites,^{73,92,123} and thus it can be used to select promising compounds more accurately. For compounds that contain heavy elements with atomic number ≥ 72 , we also incorporated spin-orbit coupling (SOC) to get more accurate E_g .⁸⁵ Note that requirements for E_g are different in solar-cell and light-emitter applications. For solar cells, the light-absorbing materials can have either direct or indirect band gaps. The optimal band gap energy should be in the range from 0.8 to 2.2 eV. This range is selected according to the relationship between Shockley-Queisser efficiency limit and band gap energy.⁸² For light emitters, the energy of photons emitted by a light-emitting material is approximately equal to the band gap energy of the material ($E_{photon} = E_g + k_B T / 2$, $k_B T$ is thermal energy). Therefore, for visible-light emission excluding short-wavelength violet light, we selected materials with E_g^{HSE} in the range from 1.65 to 3.0 eV. Note that this range partially overlap with the range required for solar cell materials. The overlap demands discrimination in exciton binding energy of the materials with E_g in 1.65 - 2.2 eV to decide their proper applications, which will be discussed in (vii). In terms of band gap type, direct band gaps are required for a high photon-emission efficiency.⁵ This is because a direct band gap greatly promotes radiative recombination of electron-hole pairs, which results in more photons emitted. In contrast, for an indirect-band gap material, radiative recombination is much less likely because phonons are required in the process.^{155,156} Therefore, indirect transition is detrimental to light-emitting materials. As the opposite process to the carrier-recombination and photon-emission in light-emitting materials, the light-absorption and electron-excitation process in solar-cell materials is also adversely affected by indirect transition with the same mechanism. However, the poor absorption and excitation

can be compensated by increasing the thickness of absorbing layer made of indirect-band gap material, as long as the material has a long minority carrier diffusion length to guarantee carrier separation and collection across the solar cell device.^{156–158} For example, silicon (indirect band gap) absorbers are made much thicker than GaAs (direct band gap) absorbers to absorb more light, and long minority diffusion length of Si ensures photogenerated carriers to cross the device before recombination.

(ii) Electron and hole effective masses (m_e^* and m_h^*). Small and balanced carrier effective masses are required for both solar cells and light emitters. This is because the photovoltaic and electroluminescence processes both require efficient carrier transport, which is beneficial for charge separation in solar cells and charge recombination in light emitters.¹⁵⁹ m_e^* and m_h^* are calculated by fitting band structures near the band edges according to the equations: $\frac{1}{m_e^*} = \frac{1}{\hbar^2} \frac{\partial^2 E_C}{\partial k^2}$, and $\frac{1}{m_h^*} = \frac{1}{\hbar^2} \frac{\partial^2 E_V}{\partial k^2}$. That is, m_e^* is derived from the curvature of the bottom conduction bands near the conduction band minimum (CBM) and m_h^* is derived from the curvature of the top valence bands near the valence band maximum (VBM). Note that the CBM (VBM) involves two reciprocal paths in the high-throughput electronic structure calculations, and only the smaller value of m_e^* (m_h^*) is used as the materials descriptor for the anisotropic materials. This is because the such values can best represent the charge transport potential that can be utilized in experiments.¹³⁷ Meanwhile, to provide more detailed information on the effective masses near the band edges, we also listed effective masses along the major directions for the anisotropic candidates in Table A.2 of Appendix A. In addition, to obtain more accurate m_e^* and m_h^* for compounds containing heavy elements (atomic number ≥ 72), the spin-orbit-coupling was included in our electronic structure calculations. In this work, a common upper limit of $1.5m_0$ was used as the screening criterion ($m_e^* \leq 1.5m_0$, $m_h^* \leq 1.5m_0$).¹¹³

(iii) Formation enthalpy difference (ΔH_f^{diff}). As shown in Table 2.1, one stoichiometry may correspond to several different prototype structures. This means that there might exist several competing phases for the same composition in the same stoichiometry. For example,

the well-known MAPbI₃ corresponds to 10 hypothetical compounds as competing phases of each other. To select compounds that can be synthesized in experiments, we define ΔH_f^{diff} as the calculated formation enthalpy difference between each compound and its most energetically favorable competing phase of the same composition and stoichiometry. This is because different stoichiometries can usually be achieved by using precursors of different molar ratios when synthesizing compounds.^{160–163} For example, both MACdBr₃ and MA₂CdBr₄ have been synthesized via an appropriate control of stoichiometry.¹⁶⁴ All compounds with $\Delta H_f^{diff} \leq 0.015$ eV/atom were selected as synthesizable compounds. This criterion comes from the MAPbI₃ example. For MAPbI₃, the tetragonal perovskite (tI20) phase is often synthesized in experiments^{1,165}, while our calculations show that oP20' is the structure with the lowest energy instead of tI20. tI20 for MAPbI₃ has a ΔH_f higher than the most stable oP20' by $\Delta H_f^{diff} = 0.015$ eV/atom. This indicates that compounds with such a small ΔH_f^{diff} can be experimentally synthesized.

(iv) Decomposition enthalpy (ΔH_d). To ensure stability of selected compounds with respect to decomposition, ΔH_d should be positive for all possible decomposition pathways. In this work, we calculated phase separation of compounds into binary products ($A_xB_yX_z \rightarrow AX + BX_n$), as well as redox decomposition pathways. The pathway with the lowest ΔH_d for each compound is used to determine its stability. We set the criterion as $\Delta H_d > 0.03$ eV/f.u. to ensure relatively high stability of selected compounds.

(v) Compounds with toxic B-site elements (As, Cd, Hg, Tl, Pb) were removed. In addition, because the compositions of our selected perovskite compounds (B = Ge/Sn/Au/Ag/Cu) have all been discovered in prior studies, we excluded all perovskites in the final list.

(vi) Structural integrity at room temperature. To evaluate room-temperature structural stability of candidate materials, *ab-initio* molecular dynamics (AIMD) calculations were carried out at 300K within the van der Waals correction using DFT-D3 method.¹⁵⁰ The entire molecular dynamics simulation lasted 5 ps with a time step of 1 fs using the Nosé-Hoover method. The supercells of 2×2×1 unit cell for the tI14, tI18, hP14, and hP28 structures and the conventional

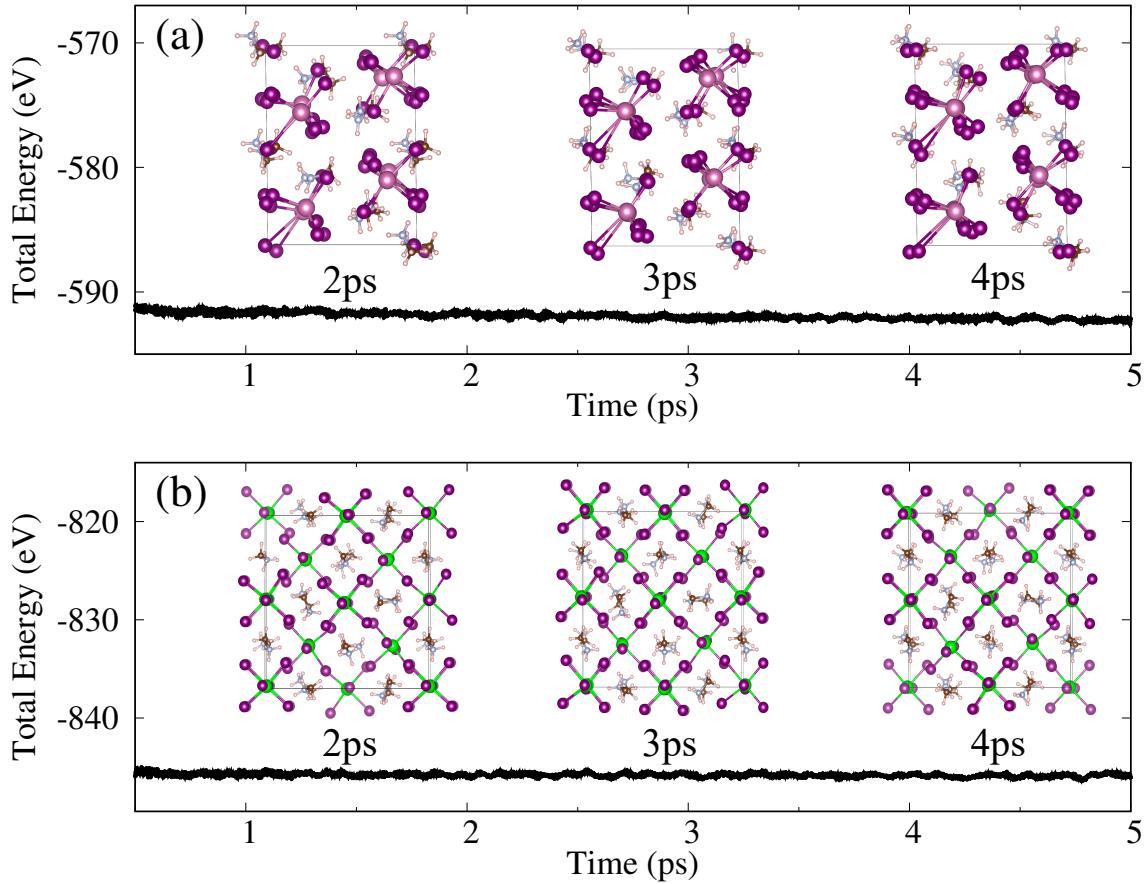


Figure 2.2: Total energy during 5ps *ab-initio* molecular dynamics (AIMD) simulations at 300K for two representative hybrid materials: (a) (MA)₃In₂I₉ (hP14) and (b) (MA)₂ZrI₆ (tI18).

unit cell for cF36 structure were used. As shown in Figure 2.2 for two representative compounds (MA)₃In₂I₉ and (MA)₂ZrI₆, the calculated total energies as a function of time during the 5ps simulation time are oscillating within a rather narrow energy range and the selected geometrical structures at 2, 3, and 4ps all exhibit an ordered crystalline phase, indicating their structural integrity at room temperature.⁸⁰ Otherwise, the candidate materials are not stable at room temperature and will be excluded from the final list. The calculated time-dependent total energies for all the final candidate materials are shown in the Fig. A.2-A.6 of Appendix A.

(vii) Exciton binding energy (E_B). E_B is the energy required to separate electron-hole pairs (excitons) into free carriers. It is critical to the electron-hole separation and recombination

processes in solar cells and light emitters, respectively. A small E_B is beneficial for separation of photogenerated electron-hole pairs in solar cells, but detrimental to charge recombination in light emitters; while a large E_B inhibits separation but promotes recombination. Therefore, E_B discriminates photovoltaic and electroluminescence applications for our final candidates. In this study, we use the hydrogen-like Wannier-Mott model to calculate E_B as an effective Rydberg:⁶²

$$E_B = \frac{\mu^* R_y}{m_0 \epsilon_r^2} \quad (2.1)$$

It is dependent on effective mass ($\frac{\mu^*}{m_0}$) and screening effect on Coulomb interaction between electrons and holes (represented by relative dielectric constant, ϵ_r). The high-frequency limit of dielectric constant (ϵ_∞), which is solely contributed by electronic polarization, is adopted as ϵ_r , and it is obtained by finite-electric field and Berry-phase calculations. The calculated exciton binding energy of some compounds are anisotropic depending on their crystal structures. We take averaged value of exciton binding energies along three directions as the descriptor ($E_B = \frac{1}{3}(E_B^{xx} + E_B^{yy} + E_B^{zz})$). Our calculations for tetragonal MAPbI₃ (tI20) with spin-orbit-coupling interactions yield an E_B about 72 meV, which is comparable to the experimental value (50 meV).¹⁶⁶ In this work, we set the criterion at $E_B \leq 130$ meV for solar-cell materials to include more promising candidates. Such relatively small E_B values are comparable to thermal energy ($k_B T$) at solar-cell operating temperatures and are beneficial for easy dissociation of photogenerated electron-hole pairs before they recombine. For light-emitting materials, we use intrinsic E_B of our candidates as a reference instead of a selection criterion. This is because light-emitting materials like perovskites are usually prepared in nanocrystals to enlarge E_B ,⁵ and materials with intrinsic small E_B can also be utilized in actual applications.

The above screening process is summarized in Figure 2.1. The screening gives us 23 final candidates for light emitters (Table 2.2) and 13 final candidates for solar cells (Table 2.3). Among these final candidates, 7 compounds are suitable for both applications.

Besides the seven materials descriptors discussed above, some other materials parameters such as defect tolerance and light absorption are also closely related to the optoelectronic properties. An ideal defect tolerance should have following property: intrinsic defects with low formation energies do not induce deep gap states, while those creating deep gap states have high formation energies.^{62,167–169} Such defect tolerance prevents the undesired recombination of photoexcited electrons and holes. A complete defect property study requires considerations of all the possible defects, such as various types of anionic and cationic vacancies, anti-sites defects, and interstitial defects, and even charged defects, in each candidate, which is beyond the scope of this high-throughput screening study. Moreover, our screening process already limits the final candidates to a very small and specific structural and compositional space out of the comprehensive materials repository of over 4500 compounds, and some predicted materials (including their inorganic analogues) have been demonstrated in recent experiments for optoelectronic applications (see Table 2.2 and 2.3), indicating a robust credibility of our high-throughput screening approach. As for the light absorption property, as discussed in previous studies, it is largely dependent on the bonding characteristic, band-gap type and values, and band dispersion,^{73,170} which have been partially addressed in the screening process and will be discussed later with the electronic structures for the final candidates.

2.4 Discussion

2.4.1 Composition and Structure

In this section, we discuss crystal structure and composition of the selected compounds. Table 2.2 and Table 2.3 show all the final candidates for light-emitting and photovoltaic materials, respectively. The final candidates based on different organic A cations take the same structures and contain similar B and X elements. Note that EA- and DMA-based compounds are not included in the final lists, because they show relatively low decomposition enthalpy compared

to their MA/FA/AD analogues according to our calculations. All the final candidates adopt five out of the 23 prototype structures, with their Pearson numbers being tI14, hP14, hP28, tI18, and cF36, see their structural illustrations in Figure 2.3a-d and Figure A.1 of Appendix A. The B sites in the five structures correspond to ions of different valence states from +2 to +4, and they greatly determine the compositions of the final candidates. Below we discuss the selected compounds in the order of their B-site valence states.

The B^{2+} candidates all take the tI14 structure (Figure 2.3a) with a chemical formula of A_2BX_4 . tI14 consists of corner-sharing octahedra in a two-dimensional (2D) arrangement. B-site elements of selected tI14 compounds include Ge and Sn. Note that Sn^{2+} or Ge^{2+} oxidation states are metastable and are prone to be oxidized to +4, which could raise concerns about their oxidation stability. However, recent experimental¹³⁷ and computational⁹² studies both indicate that the 2D hybrid perovskites based on Sn^{2+} or Ge^{2+} show enhanced materials stability compared to the 3D perovskites because of their low-dimensional structural feature, and the low-dimensional structure effectively prevents the oxidation of Sn^{2+} during the film fabrication.¹³⁷ Interestingly, unlike traditional perovskites, crystal structure of screened tI14 compounds resemble that of the 2D hybrid perovskites, implying a robust stability of these candidate materials. Moreover, even for traditional perovskites containing Sn^{2+} or Ge^{2+} , some experimental techniques are actively proposed to improve their stability and to prevent the oxidation, such as using encapsulation of devices,¹³⁸ and the solar cells based on $MASnI_3$ perovskites have been demonstrated with an efficiency around 6%.^{110,111} In addition, it is worth mentioning that some other tI14 compounds have been synthesized and proposed for solar cells in prior experiments, including MA_2CuX_4 ¹⁷¹ and $MA_2PdCl(Br)_4$ ^{161,162}. Our calculations show that these compounds have large m_h^* , and we excluded them according to the $m_h^* \leq 1.5m_0$ criterion. Our calculation results of large m_h^* are also in good agreement with the reduced charge mobility and very low device efficiency observed in the above experimental studies. Notably, Zn and Mg-based tI14 compounds show excellent optoelectronic properties in our calculations, but they were excluded due to large ΔH_f^{diff} .¹¹⁷

Table 2.2: Properties of selected hybrid halide compounds for light-emitting materials: compound, Pearson symbol of the prototype structures, equilibrium lattice parameters (in Å), calculated band gaps (in eV) from GGA-PBE (E_g^{GGA}) and HSE (E_g^{HSE}) approaches, band gap type and k -point position from VBM to CBM, electron (hole) effective mass m_e^* (m_h^*) (in m_0) near the CBM (VBM), reduced effective mass (μ^*) (in m_0), average of exciton binding energies on xx , yy , and zz directions (E_B), and decomposition enthalpy (ΔH_d , in eV/f.u.). In this and the next Table, † denotes the calculations with spin orbit coupling; ‡ denotes compounds that are suitable for both light-emitting and solar-cell materials; and * indicates experimental validation of the hybrid compound or its inorganic analogue for optoelectronics.

Compound	Pearson Symbol	Lattice Parameters			E_g^{GGA}	E_g^{HSE}	E_g	$k_{VBM} \rightarrow$	m_e^*	m_h^*	μ^*	E_B	ΔH_d
		a	b	c									
(MA) ₂ GeBr ₄	tI14	5.54	5.54	19.02	1.40	1.99	D	S - S	0.06	0.12	0.04	31.47	0.33
‡(MA) ₂ GeI ₄	tI14	5.94	5.87	20.11	1.21	1.66	D	S - S	0.11	0.11	0.06	35.22	0.24
(MA) ₂ SnCl ₄	tI14	5.56	5.48	18.35	1.80	2.49	D	S - S	0.55	0.19	0.14	157.62	0.25
‡(MA) ₂ SnBr ₄	tI14	5.72	5.74	19.08	1.11	1.67	D	S - S	0.11	0.10	0.05	37.33	0.23
(MA) ₃ In ₂ I ₉	hP14	8.23	8.31	11.00	1.34	2.18	D	Γ - Γ	0.40	0.61	0.24	200.96	0.93
(MA) ₃ Sb ₂ Br ₉	hP14	7.71	7.71	10.37	2.07	2.70	D	Γ - Γ	0.33	0.41	0.18	126.79	1.04
‡(MA) ₃ Sb ₂ I ₉ * ¹²⁹	hP14	8.26	8.26	10.91	1.52	2.02	D	Γ - Γ	0.21	0.31	0.13	53.67	0.75
(MA) ₂ ZrI ₆	tI18	8.18	8.19	12.37	1.68	2.60	D	Γ - Γ	0.74	0.98	0.42	306.27	0.77
‡(FA) ₂ SnBr ₄	tI14	5.64	5.71	20.60	1.15	1.69	D	S - S	0.61	0.09	0.08	57.66	0.03
(FA) ₃ Ga ₂ I ₉	hP14	7.94	8.25	11.83	1.27	2.17	D	A - A	0.61	1.17	0.40	374.59	0.90
(FA) ₃ In ₂ Br ₉	hP14	7.38	7.83	11.17	1.79	2.91	D	Γ - Γ	0.52	0.60	0.28	351.69	0.69
(FA) ₃ In ₂ I ₉	hP14	8.04	8.30	11.67	1.06	1.90	D	Γ - Γ	0.40	0.38	0.19	156.31	0.71
‡(FA) ₃ Bi ₂ I ₉ * ¹³¹	hP14	8.06	8.36	11.60	1.79	1.80†	D	Γ - Γ	0.28†	0.58†	0.19†	96.88	0.56
(FA) ₃ Sb ₂ I ₉ * ¹³²	hP28	8.02	8.32	23.18	1.97	2.54	D	M - M	0.39	0.68	0.25	155.23	0.79
(AD) ₂ GeI ₄	tI14	6.14	6.16	18.97	1.74	2.30	D	S - S	0.14	0.45	0.11	71.77	0.12
(AD) ₂ SnBr ₄	tI14	5.87	5.86	18.09	1.78	2.51	D	S - S	0.43	0.34	0.19	150.24	0.22
‡(AD) ₂ SnI ₄	tI14	6.22	6.21	19.17	1.33	1.87	D	S - S	0.15	0.25	0.09	48.21	0.30
(AD) ₃ Sb ₂ Br ₉	hP14	8.30	8.36	9.55	1.90	2.52	D	Γ - Γ	0.39	0.43	0.20	151.96	1.43
‡(AD) ₃ Sb ₂ I ₉	hP14	8.69	8.77	10.20	1.43	1.91	D	Γ - Γ	0.26	0.31	0.14	61.17	1.06
(AD) ₃ In ₂ I ₉	hP28	8.61	8.71	20.54	1.13	2.00	D	Γ - Γ	0.50	1.11	0.34	270.00	0.94
(AD) ₂ HfI ₆	tI18	8.47	8.46	12.17	2.07	2.89†	D	Γ - Γ	1.28†	0.80†	0.49†	431.53	0.93
(AD) ₂ SnBr ₆	tI18	8.13	8.12	11.56	1.36	2.42	D	Γ - Γ	0.51	1.24	0.36	483.68	0.90
(AD) ₂ TeBr ₆	tI18	8.29	8.30	11.18	2.14	2.71	D	Γ - Γ	1.14	0.97	0.52	533.26	0.99

The B^{3+} candidates take two different crystal structures, hP14 and hP28, both with the formula of $A_3B_2X_9$ (Figure 2.3b and 2.3c, respectively). Their difference lies in microscopic structure units. hP14 consists of corner-sharing octahedra in 2D corrugated layers, while hP28 consists of face-sharing octahedra in zero-dimensional (0D) dimers. As competing phases of each other, hP14 and hP28 for the same composition usually have pretty close total energies. To decide which structure stays in the final list, we first followed our criterion for selecting stable competing phases ($\Delta H_f^{diff} \leq 0.015$ eV/atom), and then kept the one with more suitable electronic properties for light-emitter or solar-cell applications. hP14 is usually more favorable due to higher electronic dimensionality⁸⁷, but hP28 gives more appropriate properties for some compositions according to our calculations. For example, hP28 $MA_3Sc_2I_9$ yields a direct band gap of proper energy, while hP14 yields an indirect band gap out of the optimal range. In fact, halogen substitution has been demonstrated to lead to phase transition between hP14 and hP28 for $A_3B_2X_9$ compounds¹⁴⁵. The B^{3+} elements of the selected compounds contain Ga, In, Sb, and Bi. Interestingly, some compounds in hP28 ($Cs_3Bi_2I_9$, $MA_3Bi_2I_9$, and $MA_3Sb_2I_9$) and hP14 ($Cs_3Sb_2I_9$ and $Rb_3Sb_2I_9$) have been fabricated for photovoltaic applications in prior experiments.³⁷ Accordingly, this class of materials, particularly the new compounds discovered in this work, hold great promise with intrinsic high stability and non-toxicity for the optoelectronic applications.

The B^{4+} candidates adopt two very similar structures, tetragonal tI18 and cubic cF36 (Figure 2.3d and Figure S1p, respectively). These two structures have the same formula of A_2BX_6 and can convert to each other through phase transition.¹⁷² They both consist of 0D isolated BX_6 octahedra. According to our screening, promising B-site elements in these structures include Zr, Hf, Sn, and Te. Cs_2SnI_6 and Cs_2TeI_6 (cF36) have been incorporated in solar cell devices.¹³⁴ These compounds were demonstrated to have high air and moisture stability, proper band gaps, and good electron conductivity. Interestingly, it is noted that Cs_2PdBr_6 (cF36) has also been synthesized and shows promising properties and high stability;¹⁶³ its hybrid analogue MA_2PdBr_6 (cF36) was not selected in our list because of a large m_h^* of $1.98m_0$.

2.4.2 Electronic Structures

In this section, we discuss electronic band structures and atomic orbital projected density of states (PDOS) of representative candidates to reveal electronic properties of all selected compounds. This is because compounds of each prototype structure have common attributes in electronic structures. We selected $(MA)_2GeI_4$, $(MA)_3In_2I_9$, $(FA)_3Sb_2I_9$, and $(MA)_2ZrI_6$ to represent selected compounds of the prototype structures tI14, hP14, hP28, and tI18, respectively. Note that example of cF36 compounds is not shown here because cF36 is very similar to tI18. Figure 2.3a'-d' and 2.3a''-d'' show the band structures and PDOS of the four representative candidates. The calculated band gap and effective masses data for all final candidates is listed in Table 2.2 and Table 2.3.

Table 2.3: Properties of selected hybrid halide compounds for solar-cell materials.

Compound	Pearson Lattice Parameters Symbol	Lattice Parameters			E_g^{GGA}	E_g^{HSE}	E_g	$k_{VBM} \rightarrow$ Type	k_{CBM}	m_e^*	m_h^*	μ^*	E_B	ΔH_d
		a	b	c										
$\ddagger(MA)_2GeI_4$	tI14	5.94	5.87	20.11	1.21	1.66	D	S - S	0.11	0.11	0.06	35.22	0.24	
$\ddagger(MA)_2SnBr_4$	tI14	5.72	5.74	19.08	1.11	1.67	D	S - S	0.11	0.10	0.05	37.33	0.23	
$(MA)_2SnI_4$	tI14	6.12	6.11	20.00	0.97	1.42	D	S - S	0.18	0.10	0.06	33.81	0.30	
$\ddagger(MA)_3Sb_2I_9^{*129}$	hP14	8.26	8.26	10.91	1.52	2.02	D	Γ - Γ	0.21	0.31	0.13	53.67	0.75	
$(MA)_3Bi_2I_9$	hP14	8.35	8.35	11.00	1.85	1.82 \dagger	I	A - Γ	0.41 \dagger	0.62 \dagger	0.25 \dagger	124.88	0.59	
$(MA)_2SnI_6^{*134}$	cF36	11.61	11.44	12.55	0.09	0.80	D	Γ - Γ	0.22	1.16	0.18	94.82	0.43	
$(MA)_2TeI_6^{*134}$	cF36	11.67	11.51	12.58	1.27	1.77	I	Γ - L	0.25	1.24	0.21	104.21	0.78	
$\ddagger(FA)_2SnBr_4$	tI14	5.64	5.71	20.60	1.15	1.69	D	S - S	0.61	0.09	0.08	57.66	0.03	
$\ddagger(FA)_3Bi_2I_9^{*131}$	hP14	8.06	8.36	11.60	1.79	1.80 \dagger	D	Γ - Γ	0.28 \dagger	0.58 \dagger	0.19 \dagger	96.88	0.56	
$\ddagger(AD)_2SnI_4$	tI14	6.22	6.21	19.17	1.33	1.87	D	S - S	0.15	0.25	0.09	48.21	0.30	
$\ddagger(AD)_3Sb_2I_9$	hP14	8.69	8.77	10.20	1.43	1.91	D	Γ - Γ	0.26	0.31	0.14	61.17	1.06	
$(AD)_3Bi_2I_9$	hP14	8.78	8.84	10.26	1.79	1.80 \dagger	I	M - Γ	0.38 \dagger	0.48 \dagger	0.21 \dagger	109.24	0.94	
$(AD)_2TeI_6$	cF36	12.54	11.63	12.17	1.24	1.87	I	Γ - L	0.27	1.09	0.22	120.85	0.93	

$(MA)_2GeI_4$, representing the tI14 candidates with B^{2+} cations, shows a direct band gap of

1.66 eV at S point (Figure 2.3a'). Bands near the conduction band minimum (CBM) and valence band maximum (VBM) are very dispersive, yielding small m_e^* and m_h^* of both $0.11m_0$. Its PDOS shows that conduction band (CB) is mainly contributed by Ge $4p$ orbitals while valence band (VB) is mostly derived from I $5p$ and Ge $4s$ orbitals (Figure 2.3a'').

(MA)₃In₂I₉, as an example of the hP14 candidates, shows a direct band gap of 2.18 eV at Γ point (Figure 2.3b'). Near the band edges, it has a m_e^* of $0.40m_0$, and a m_h^* of $0.61m_0$. Its VB is derived from In $4d$ and I $5p$ orbitals, and the CB is derived from In $5s$ and I $5p$ orbitals (Figure 2.3b''). (FA)₃Sb₂I₉, as an example of hP28 candidates, shows a direct band gap of 2.54 eV at M point (Figure 2.3c'). The m_e^* and m_h^* were calculated to be $0.39m_0$ and $0.68m_0$, respectively. Its VB consists of Sb $5s$ and I $5p$ orbitals, and the CB consists of Sb $5p$ and I $5p$ orbitals (Figure 2.3c''). These two candidates both contain B³⁺ cations but adopt different prototype structures. To discuss dependence of electronic structures on crystal structures, we compare the two candidates' valence bands on two parts of the hexagonal k -path. On the Γ -A k -path, both the hP14 and hP28 candidates show non-dispersive valence bands and large m_h^* . Γ -A corresponds to [001] direction for the hexagonal lattice in real space, and large calculated m_h^* on Γ -A indicates poor hole transport along [001]. This agrees well with poor octahedral connectivity along [001] in the hP14 and hP28 structures (Figure 2.3b and 2.3c). On the M-K k -path, valence bands of the hP14 candidate is much more dispersive than those of hP28 candidate. This is because M-K corresponds to real-space direction in (001) plane, and the 2D connectivity in hP14 is much more beneficial for hole transport than the 0D connectivity in hP28. Notably, compounds in both of these structures have rather indistinct VBMs, making the band gap types ambiguous. For light-emitting applications, the band gaps become more distinctly direct due to quantum confinement when the compounds are synthesized as nanocrystals.^{173,174}

(MA)₂ZrI₆, representing the tI18 candidates with B⁴⁺ cations, shows a distinct direct band gap of 2.60 eV at Γ point, with very dispersive bands near the band edges (Figure 2.3d'). Its PDOS shows that both VB and CB are mainly contributed by Zr $4d$ and I $5p$ orbitals (Figure

2.3d^{'''}). As mentioned, B⁴⁺-based compounds in the tI18 and cF36 structures consist of isolated octahedra, and their B-X bonds are not well connected in a 3D manner. However, the BX₆ octahedra are in close proximity to each other, making it possible for tI18 and cF36 compounds to possess appropriate band gaps and effective masses for the optoelectronic applications³⁷. Interestingly, the previously synthesized Cs₂SnI₆ (cF36) shows large m_h^* , which is not suitable for photovoltaics.¹³⁴ Our screening results of novel tI18 and cF36 compounds show more suitable properties, especially small and balanced carrier effective masses, and hold great promise for applications in light emitters and solar cells.

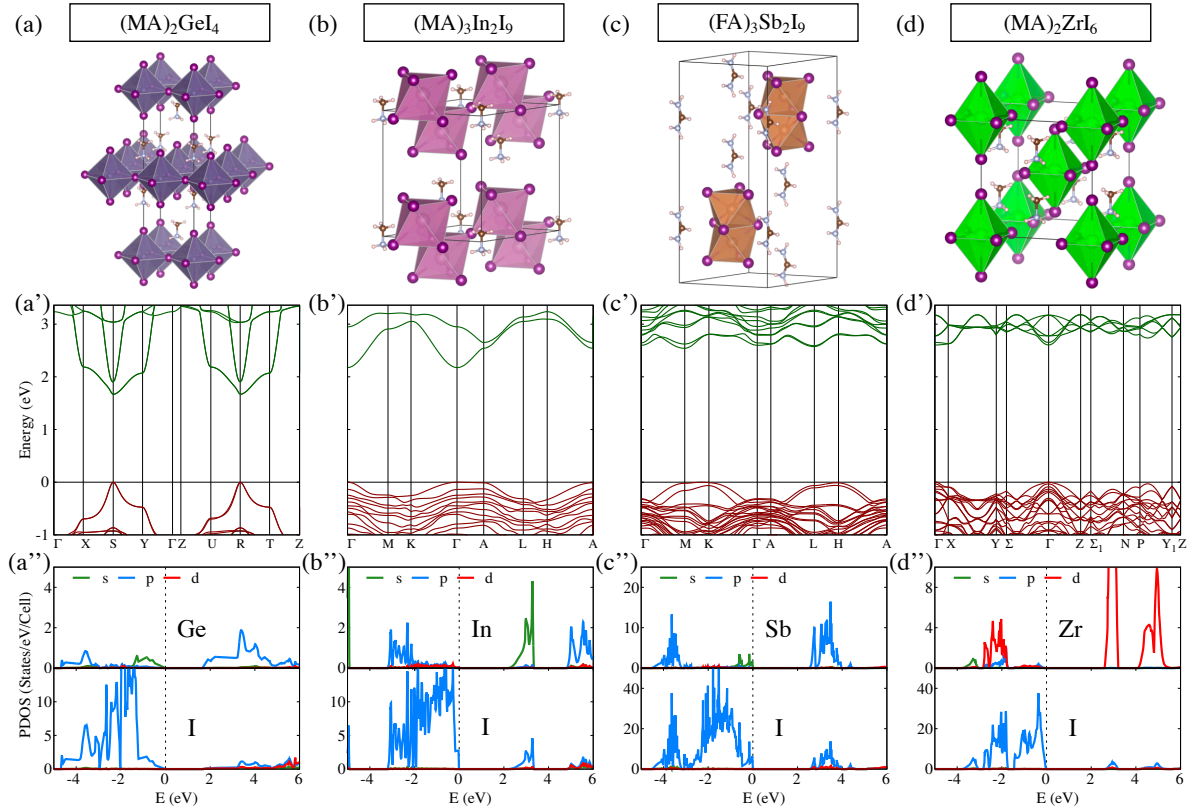


Figure 2.3: Representative candidates and their prototype structures: (a) (MA)₂GeI₄ in tI14, a tetragonal structure consisting of layers of corner-sharing B^{II}X₆ octahedra, (b) (MA)₃In₂I₉ in hP14, a hexagonal structure consisting of corrugated layers of corner-sharing B^{III}X₆ octahedra, (c) (FA)₃Sb₂I₉ in hP28, a hexagonal structure consisting of dimers of face-sharing B^{III}X₆ octahedra, and (d) (MA)₂ZrI₆ in tI18, a tetragonal structure consisting of isolated B^{IV}X₆ octahedra. Their calculated electronic band structures are shown in (a'-d') and atomic orbital projected density of states with HSE06 correction are shown in (a''-d'').

2.5 Conclusion

In summary, we have demonstrated a high-throughput approach to the discovery of hybrid halide compounds beyond perovskites for optoelectronic applications. The discovery process has screened a comprehensive quantum materials repository containing 4507 hybrid compounds using a series of electronic and energetic descriptors including difference of formation enthalpy, decomposition enthalpy, band gap, charge carrier effective masses, and exciton binding energy to select promising candidates for optoelectronic applications. A total number of 23 candidates for light-emitting diodes and 13 candidates for solar energy conversion were selected. These candidates adopt five prototype structures, including tetragonal structure consisting of layers of corner sharing $B^{II}X_6$ (tI14), hexagonal structure consisting of corrugated layers of corner-sharing $B^{III}X_6$ (hP14), hexagonal structure consisting of dimers of face-sharing $B^{III}X_6$ (hP28), tetragonal structure consisting of isolated $B^{IV}X_6$ (tI18), and cubic structure consisting of isolated $B^{IV}X_6$ (cF36). The tI14 candidates contain $B^{II}=\text{Ge, Sn}$; the hP14 and hP28 candidates contain $B^{III}=\text{Ga, In, Sb, Bi}$; and the tI18 and cF36 candidates contain $B^{IV}=\text{Zr, Te, Sn, and Hf}$. It is important to note that this approach is transformative to the discovery of other types of functional materials.

2.6 Acknowledgments

Chapter 2, in full, is a reprint of the material “High-Throughput Computational Design of Organic–Inorganic Hybrid Halide Semiconductors Beyond Perovskites for Optoelectronics” as it appears in *Energy & Environmental Science*. Yuheng Li, Kesong Yang, 12, 2233-2243, 2019. The dissertation author was the primary investigator and author of this paper.

Chapter 3

Stability Diagrams, Defect Tolerance, and Absorption Coefficients of Hybrid Halide Semiconductors: High-throughput First-principles Characterization

On the basis of the 29 selected hybrid halide compounds from Chapter 2, in this chapter, we report a systematic computational study of the stability diagram, defect tolerance, and optical absorption coefficients for these candidate materials using high-throughput first-principles calculations. We take two exemplary compounds, MA_2SnI_4 and $\text{MA}_3\text{Sb}_2\text{I}_9$, as examples to show the computational process and to discuss in detail. This work is expected to provide a detailed guide for further experimental synthesis and characterization, with the potential to develop novel lead-free optoelectronic devices.

3.1 Introduction

The organic-inorganic hybrid halide perovskites have emerged as one important class of semiconductor materials for various types of optoelectronic applications such as solar cells and light emitting diodes because of their low-temperature solution-based fabrication techniques and excellent optoelectronic properties.^{2,3,10,11,175,176} As proof of example, the power conversion efficiency (PCE) of the perovskite-based solar cells at lab-scale testing has rapidly increased from 3.8% to 25.2% in the past few years.¹⁷⁷ This is mainly attributed to their exceptional optoelectronic properties such as tunable bandgaps, high absorption coefficient, long carrier diffusion length and lifetime, strong defect tolerance, and high carrier mobility.^{4,12,13,15,92,167,178}

In spite of the exceptional properties, it is still of urgent demand to search for stable and non-toxic alternative hybrid materials because of low stability and presence of toxic lead in the halide perovskite.¹¹ Some great research efforts have been made to search for new halide perovskites materials using high-throughput materials design approach,^{35,62,63,73,80,113–115,123,125} though nearly all of them are focusing on either purely inorganic perovskites or several limited number of hybrid perovskite structures (cubic structure or its distorted derivatives). This is mainly due to great computational challenges caused by the structural complexity of the hybrid structures in the large-scale first-principles calculations. It is also worth noting that quantitative physical properties of hybrid perovskites cannot be directly derived from their inorganic bulk analogs.

In our recent work, instead of focusing on the prototype perovskite structure, we have carried out a systematic investigation of all the possible hybrid halide materials on the basis of the 24 prototype structures and five relatively small organic cations using high-throughput computational materials design approach.⁷² By employing a group of combinatorial material descriptors that covers the critical features of electronic band structures, several energetic parameters, structural integrity at room-temperature, and exciton binding energies, we have successfully identified 13 candidates for solar energy conversion and 23 candidates for light-emitting diodes (a total number

of 29 hybrid compounds) in five different types of crystal structures out of a quantum materials repository of 4507 hybrid halide materials.⁷²

In this work, to provide a more detailed guide for the experimental synthesis and characterization, we systemically studied the stability diagrams, defect tolerance, and absorption coefficients for the identified 29 promising hybrid halide materials. To do this, we first calculated thermodynamically stable ranges for all these compounds and considered non-equivalent lattice sites in each compound for building defect structures. A total number of about 5000 defect structures (including neutral and charged) were computed to analyze the defect transition energy levels using high-throughput first-principles calculations. The absorption coefficients were calculated from the dielectric function. For convenience, two representative compounds, MA₂SnI₄ and MA₃Sb₂I₉, were selected for discussing the computational and analysis process. The calculated stability diagrams, defect formation energies and transition levels, and absorption coefficients for all the 29 compounds are presented in Appendix B.

3.2 Methods

The automatic framework AFLOW¹⁴⁷ based on the Vienna *Ab-initio* Simulation Package (VASP)¹⁷⁹ was used for the high-throughput first-principles Density Functional Theory (DFT) calculations. The Projector Augmented Wave (PAW) pseudopotentials were used for describing electron-ion interactions,¹⁸⁰ and the Generalized Gradient Approximation (GGA) parametrized by Perdew, Burke, and Ernzerhof (PBE) was used for treating electron-electron exchange-correlation functional.⁸³ The van der Waals (vdW) functional DFT-D3 is incorporated to properly describe the long-range dispersion interactions between the organic molecules.¹⁵⁰ k -points grid of 0.05 Å⁻¹ were automatically set for structural relaxation with a convergence tolerance of 0.01 meV/atom, and a denser grid of 0.04 Å⁻¹ was used in static calculations. Other computational settings such as the cutoff energy (the highest value of the pseudopotentials) were managed by the AFLOW code

that generates appropriate entries for the structural relaxation and static calculations sequentially and automatically.¹⁴⁷ The supercell model (with more than 40 atoms) was built for each material system to study defect properties, in which the supercell size was determined based on the convergence tests for the formation energy of iodine vacancy, see Figure B.1 and Table B.1 in Appendix B. Our calculations indicate that the supercell with more than 40 atoms is large enough to produce converged defect formation energy. Similar conclusions can be also found in previous literature on perovskite oxides.^{181,182} The hybrid DFT calculations within Heyd-Scuseria-Ernzerhof (HSE) formalism with 25% Hartree-Fock (HF) exchange are employed to calculate the absorption coefficients.^{152,153}

All the possible intrinsic point defects, including vacancies (V_A , V_B , V_X), interstitial (A_i , B_i , X_i), and antisite (A_B , B_A , A_X , X_A , B_X , X_B) defects, were considered for all the 29 hybrid halide compounds $A_xB_yX_z$, see the list of compounds in Table 3.1. The defect structures were built based on all the possible non-equivalent lattice sites in each compound. The PyCDT toolkit based on the Interstitial Finding Tool (InFiT) was used to determine possible interstitial sites.^{55,99} The building process yields a total number of 2160 defect structures. After first-principles total energy calculations, we selected the defect structure with the lowest total energy for the same type of defects for the further investigation of defect transition levels. This process leads to a total number of 348 selected structures, which are the lowest-energy site representatives for 12 intrinsic point defects in each of the 29 compounds and used for charged defect calculations.

For charged defect calculations, we considered defect charge ranges derived from all the possible oxidation states of involved element(s) and the defect type based on the selected 348 defect structures. In terms of defect type, vacancies of atom A^n (n is the formal charge of A in the compound $A_xB_yX_z$) can have charge states in the range of $[-n, +n]$; interstitial A^m (m represents all the possible oxidation states of A) can have charge states in the range of $[\min(m), \max(m)]$; and antisite A_B have charge ranges of $[\min(p), \max(p)]$, where p represents all possible oxidation states of A and B.⁹⁹ According to the above charge ranges, a total number of about 2400 charged

defect calculations were to be carried out.

Table 3.1: List of 29 candidate hybrid halide semiconductor materials. Calculated Properties: compound, Pearson symbol, lattice parameters (Å), band gap E_g (eV) using hybrid functional calculations (* marks calculations with spin-orbit coupling), absorption coefficient α ($\times 10^5$ cm^{-1}) at 450 nm, and defect tolerance level. The lattice parameters and band gaps are adapted from Ref⁷².

Compound	Pearson Symbol	Lattice Parameters			E_g	α	Defect Tolerance
		a	b	c			
(MA) ₂ GeBr ₄	tI14	5.54	5.54	19.02	1.99	1.10	high
(MA) ₂ GeI ₄	tI14	5.94	5.87	20.11	1.66	1.95	high
(MA) ₂ SnCl ₄	tI14	5.56	5.48	18.35	2.49	0.41	low
(MA) ₂ SnBr ₄	tI14	5.72	5.74	19.08	1.67	1.61	high
(MA) ₂ SnI ₄	tI14	6.12	6.11	20.00	1.42	2.43	high
(FA) ₂ SnBr ₄	tI14	5.64	5.71	20.60	1.69	1.58	high
(AD) ₂ GeI ₄	tI14	6.14	6.16	18.97	2.30	1.12	low
(AD) ₂ SnBr ₄	tI14	5.87	5.86	18.09	2.51	0.84	low
(AD) ₂ SnI ₄	tI14	6.22	6.21	19.17	1.87	1.89	high
(MA) ₃ In ₂ I ₉	hP14	8.23	8.31	11.00	2.18	0.22	low
(MA) ₃ Sb ₂ Br ₉	hP14	7.71	7.71	10.37	2.70	0.49	low
(MA) ₃ Sb ₂ I ₉	hP14	8.26	8.26	10.91	2.02	3.10	high
(MA) ₃ Bi ₂ I ₉	hP14	8.35	8.35	11.00	1.82*	0.63	high
(FA) ₃ Ga ₂ I ₉	hP14	7.94	8.25	11.83	2.17	0.08	low
(FA) ₃ In ₂ Br ₉	hP14	7.38	7.83	11.17	2.91	0.03	high
(FA) ₃ In ₂ I ₉	hP14	8.04	8.30	11.67	1.90	0.30	low
(FA) ₃ Bi ₂ I ₉	hP14	8.06	8.36	11.60	1.80*	0.86	low
(AD) ₃ Sb ₂ Br ₉	hP14	8.30	8.36	9.55	2.52	0.41	low
(AD) ₃ Sb ₂ I ₉	hP14	8.69	8.77	10.20	1.91	2.90	high
(AD) ₃ Bi ₂ I ₉	hP14	8.78	8.84	10.26	1.80*	0.55	high
(FA) ₃ Sb ₂ I ₉	hP28	8.02	8.32	23.18	2.54	0.53	low
(AD) ₃ In ₂ I ₉	hP28	8.61	8.71	20.54	2.00	0.51	low
(MA) ₂ ZrI ₆	tI18	8.18	8.19	12.37	2.60	0.39	high
(AD) ₂ HfI ₆	tI18	8.47	8.46	12.17	2.89*	0.08	low
(AD) ₂ SnBr ₆	tI18	8.13	8.12	11.56	2.42	0.06	high
(AD) ₂ TeBr ₆	tI18	8.29	8.30	11.18	2.71	0.20	high
(MA) ₂ SnI ₆	cF36	11.61	11.44	12.55	0.80	0.60	high
(MA) ₂ TeI ₆	cF36	11.67	11.51	12.58	1.77	2.93	low
(AD) ₂ TeI ₆	cF36	12.54	11.63	12.17	1.87	2.65	low

It is noted that, in the charged defects calculations under the periodic boundary conditions, the Coulombic interaction between a charged defect and its periodic images is the dominant

source of error for defect energetics. The interaction is inversely proportional to the supercell periodic length. The supercells used in the high-throughput calculations are finitely sized, so the charged defect images cannot be effectively isolated and thus the Coulombic interaction cannot be completely eliminated either. To correct supercell finite-size effects in the charged defects calculations, we employed the image charge correction proposed by Freysoldt *et al.* in our calculations by calling *pymatgen* package.^{55,183}

3.3 Results and Discussion

3.3.1 Stability Diagram

We first computed stability diagrams of the 29 hybrid halide compounds by determining their thermodynamically stable chemical ranges with respect to their decomposers. Note that the dynamic stability, as a more realistic descriptor for screening novel materials than the thermodynamic stability, has been investigated in our prior study using *ab initio* molecular dynamics (AIMD) simulations.⁷² Here, the calculated thermodynamic stability diagrams have two major purposes: i) to determine the chemical potential ranges for synthesizing the hybrid materials; and ii) to choose appropriate chemical potentials for subsequent defect formation energy calculations. The first representative compound, MA₂SnI₄, a tetragonal compound consisting of layers of corner-sharing SnI₆, was taken as an example to discuss the computational process, see Figure 3.1(a). Under thermodynamic equilibrium growth conditions, the formation of MA₂SnI₄ should satisfy the following equation:

$$2\Delta\mu_{MA} + \Delta\mu_{Sn} + 4\Delta\mu_I = \Delta H(MA_2SnI_4), \quad (3.1)$$

in which $\Delta\mu_X = \mu_X - E_X$ is chemical potential change of *X* component (organic molecule MA was treated as one component), and ΔH is formation enthalpy. The total energy of MA species

(E_{MA}) was calculated using a standalone neutral MA molecule in a big box, which represents the gaseous phase as reference ground state for the species. In addition, to prevent formation of secondary phases MAI, SnI₂, and SnI₄, the following stability limits should also be satisfied:

$$\Delta\mu_{MA} + \Delta\mu_I < \Delta H(MAI), \quad (3.2)$$

$$\Delta\mu_{Sn} + 2\Delta\mu_I < \Delta H(SnI_2), \quad (3.3)$$

$$\Delta\mu_{Sn} + 4\Delta\mu_I < \Delta H(SnI_4). \quad (3.4)$$

By applying these thermodynamic conditions, we plotted the stability diagram for MA₂SnI₄ against $\Delta\mu_{Sn}$ and $\Delta\mu_I$, as shown in Figure 3.1(b). The green region is the thermodynamically stable range for MA₂SnI₄. In this region, we have selected three representative points: A ($\Delta\mu_{Sn} = -4.41$ eV, $\Delta\mu_I = 0$ eV), B ($\Delta\mu_{Sn} = -1.56$ eV, $\Delta\mu_I = -0.75$ eV), and C ($\Delta\mu_{Sn} = 0$ eV, $\Delta\mu_I = -2.2$ eV), which represent chemical potential conditions of X-rich/B-poor, X-moderate/B-moderate, and X-poor/B-rich, respectively.

Similarly, the stability limits and stability diagram of the second example compound MA₃Sb₂I₉ were calculated and plotted, as shown in Figure 3.2(a) and 3.2(b). The three representative $\Delta\mu$ points for MA₃Sb₂I₉ are: A ($\Delta\mu_{Sb} = -2.73$ eV, $\Delta\mu_I = 0$ eV), B ($\Delta\mu_{Sb} = -1.04$ eV, $\Delta\mu_I = -0.35$ eV), and C ($\Delta\mu_{Sb} = 0$ eV, $\Delta\mu_I = -0.91$ eV). The calculated stability diagrams for all the 29 compounds, plotted against the chemical potential change $\Delta\mu_B$ and $\Delta\mu_X$, are shown in Figures B.2-B.6 of Appendix B. To deduce all the possible thermodynamic stability limits for each of the 29 compounds, we have carefully considered all the possible neighboring secondary phases on the basis of the open quantum materials repositories AFLOWLIB⁵⁴ and Materials Project.⁵⁸ The binary halide compounds BX_n for B elements in the 29 A_xB_yX_z compounds were systemically recalculated in the DFT-D3 approach.

3.3.2 Defect Tolerance

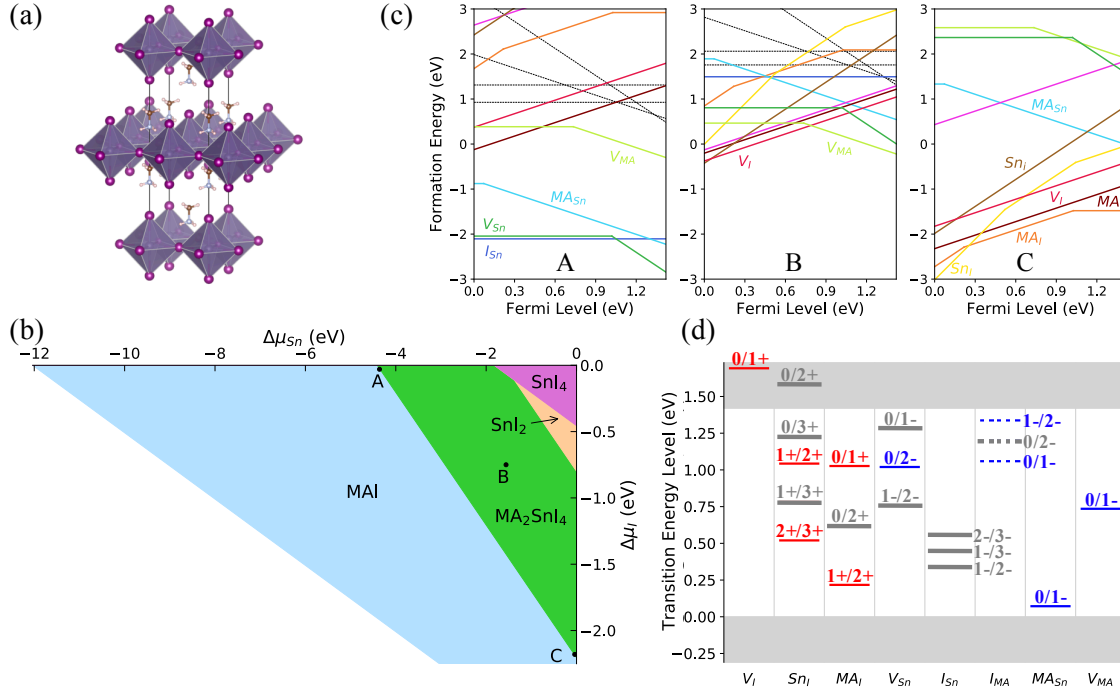


Figure 3.1: Schematic illustration of (a) crystal structure, (b) stability diagram, and (c-d) defect properties of MA_2SnI_4 . In the stability diagram, the green region depicts the thermodynamically stable range for equilibrium growth of MA_2SnI_4 under different Sn and I chemical potentials; outside this region, the compound decomposes into MAI, SnI_2 , or SnI_4 . Three representative points A ($\Delta\mu_{\text{Sn}} = -4.41$ eV, $\Delta\mu_{\text{I}} = 0$ eV), B ($\Delta\mu_{\text{Sn}} = -1.56$ eV, $\Delta\mu_{\text{I}} = -0.75$ eV), and C ($\Delta\mu_{\text{Sn}} = 0$ eV, $\Delta\mu_{\text{I}} = -2.2$ eV) are selected to calculate the defect formation energy. (c) Defect formation energies as a function of Fermi level at chemical potentials A, B, and C. (d) Defect transition energy levels, in which gray levels indicate the metastable charge states and red (blue) lines indicate the donor (acceptor) levels. The dashed lines in (c-d) indicate high defect formation energies. Note that some defects in (c) but absent in (d) mean that these defects do not create transition energy levels within the band gap or near the band edges; and the defects in (d) but absent in (c) mean that they have high formation energies at all the considered chemical potential conditions A, B, and C. In the compound MA_2SnI_4 , the defects creating deep transition levels include SnI_i , MAI_i , V_{Sn} , and V_{MA} , which, however, have high formation energies at chemical potential condition B, indicating a high defect tolerance.

Defect tolerance significantly influences the optoelectronic properties of semiconductor materials and can be evaluated from the defect transition levels and the defect formation energy. A strong defect tolerance can prevent the undesired recombination of photoexcited electrons and holes, and has following features: the intrinsic defects with a low formation energy will not

create deep gap states, while those producing deep gap states have a relatively high formation energy.^{72,167} Formation energy (E^f) of a defect X at charge state q can be calculated using the following equation:⁹⁶

$$E^f[X^q] = E_{tot}[X^q] - E_{tot}[bulk] - \sum_i n_i \mu_i + qE_F + E_{corr}, \quad (3.5)$$

in which $E_{tot}[X^q]$ and $E_{tot}[bulk]$ are total energies of defected and pristine supercells, respectively. $\sum n_i \mu_i$ is sum of chemical potentials to compensate in the defected supercell, E_F is Fermi energy, and E_{corr} is a correction term for electrostatic interactions between supercell images. Here, we only considered defect charge states derived from involved elements' oxidation states in the compound, which gives upper and lower limits of defects' charge states. All the charge states between these limits are plotted in the formation energy plots as a function of Fermi energy. This consideration leads to a convenient visualization of the most probable charge states and avoidance of redundancy in the plots, which is also well justified by a prior computational study of point defects in the hybrid halide systems.¹⁶⁷ By taking iodine as one example, one only needs to consider its oxidation state of 1- in the hybrid iodides. As a result, an interstitial iodine (I_i) can have two possible charge states of 0 and 1-, and one iodine vacancy (V_I) can have two possible charge states of 0 and 1+. The reason why iodine's positive oxidation states are not considered is that there are no elements oxidizing iodine in the hybrid metal iodide materials.

Figure 3.1c and 3.2c show the formations energies of intrinsic point defects under chemical potential conditions A, B, and C for MA_2SnI_4 and $MA_3Sb_2I_9$, respectively. The lower E^f are shown in colored solid lines, while higher E^f are shown in black dashed lines. The slope of line represents charge q , so horizontal lines show E^f of neutral defects ($q = 0$). E^f lines change as the $\sum n_i \mu_i$ term changes among A, B, and C, which is in agreement with chemical condition changes of the involved elements. For example, as chemical condition becomes more I-rich, E^f of V_I and I_i increases and decreases, respectively. Accordingly, the intersection points between different

charge states of a defect correspond to the same E_F . As shown in Figure 3.1c, the defects with relatively low E^f in MA_2SnI_4 are: V_{Sn} , I_{Sn} , and MA_{Sn} at A; V_I and Sn_i at B; Sn_I , MA_I , MA_i , V_I , and Sn_i at C.

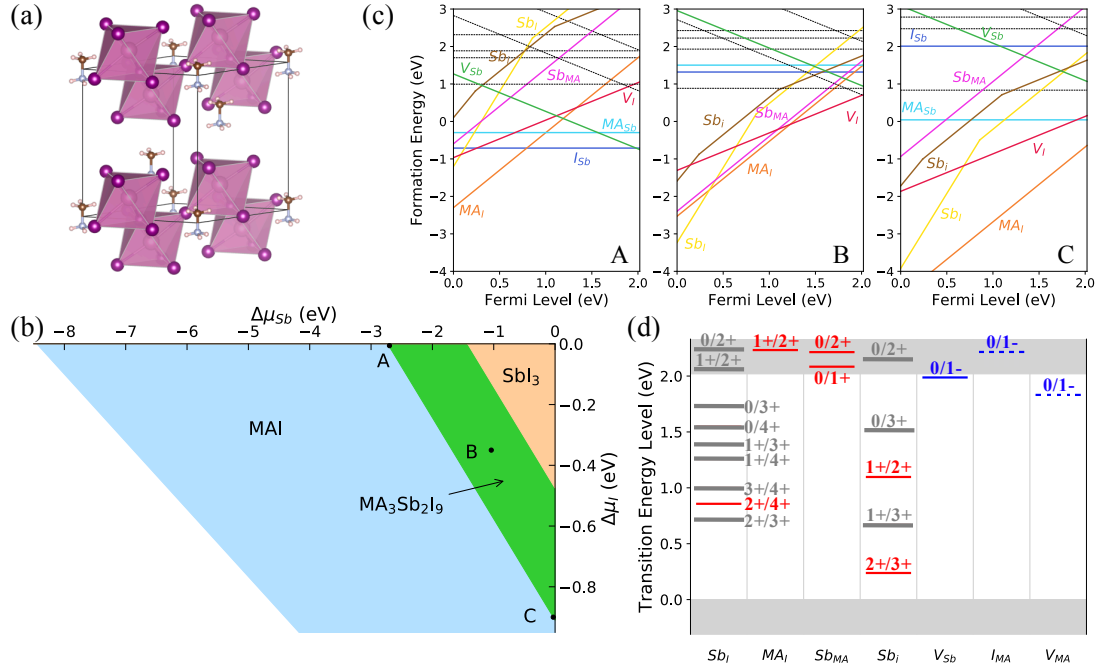


Figure 3.2: Schematic illustration of (a) crystal structure, (b) stability diagram, and (c-d) defect properties of $\text{MA}_3\text{Sb}_2\text{I}_9$. Three representative points A ($\Delta\mu_{\text{Sb}} = -2.73$ eV, $\Delta\mu_I = 0$ eV), B ($\Delta\mu_{\text{Sb}} = -1.04$ eV, $\Delta\mu_I = -0.35$ eV), and C ($\Delta\mu_{\text{Sb}} = 0$ eV, $\Delta\mu_I = -0.91$ eV) are selected to calculate the defect formation energy. (c) Defect formation energies as a function of Fermi level at chemical potentials A, B, and C. (d) Defect transition energy levels. In the compound $\text{MA}_3\text{Sb}_2\text{I}_9$, only two defects, Sb_I and Sb_i , can create deep transition levels, but they have high formation energies at chemical potential condition A, indicating a high defect tolerance. At chemical potential conditions B and C, Sb_I has a relatively low formation energy and thus its deep transition levels could be introduced, though.

The transition energy level ($\epsilon(q1/q2)$) of a defect is the Fermi level position that corresponds to the intersection point of two different charge states ($q1$ and $q2$) of a defect in the E^f plots, where the formation energies of the two charge states are equal. In other words, $\epsilon(q1/q2)$ is the energy level where the defect can accept or donate electrons so that the charge states of a defect can be changed. As shown in Figure 3.1c, the lowest E^f of V_{Sn} (green line) is composed of two parts, *i.e.*, V_{Sn}^0 (left) and V_{Sn}^{2-} (right), and the two parts intersect at $E^f = 1.02$ eV. At this

transition energy level, V_{Sn}^0 accepts two electrons and becomes V_{Sn}^{2-} . On the basis of eq. 3.5, $\epsilon(q1/q2)$ can be calculated using the following equation:⁹⁶

$$\epsilon(q1/q2) = \frac{E^f(X^{q1}; E_F = 0) - E^f(X^{q2}; E_F = 0)}{q2 - q1}, \quad (3.6)$$

where $E^f(X^q; E_F = 0)$ is the formation energy of defect X^q when the Fermi level is at 0 (valence band maximum). One defect with $\epsilon(q1/q2)$ close to the middle of the band gap has a deep transition level that will attract electrons/holes and act as undesired nonradiative recombination centers. In contrast, defects with $\epsilon(q1/q2)$ close to band edges or at the inside of conduction band (CB) or valence band (VB) will not significantly affect the optoelectronic performance.

The calculated transition levels of MA_2SnI_4 and $MA_3Sb_2I_9$ are shown in Figure 3.1d and 3.2d, respectively. In the $\epsilon(q1/q2)$ figures, the red and blue levels indicate intrinsic donors and acceptors, and the top and bottom grey regions indicate CB and VB, respectively. For MA_2SnI_4 (band gap of 1.42 eV), as shown in Figure 3.1d, the defects that induce deep transition levels are Sn_I ($\epsilon(1+/2+) = 1.04$ eV and $\epsilon(2+/3+) = 0.52$ eV), MA_I ($\epsilon(0/1+) = 1.03$ eV and $\epsilon(1+/2+) = 0.22$ eV), V_{Sn} ($\epsilon(0/2-) = 1.02$ eV), I_{MA} ($\epsilon(0/1- = 1.06$ eV), and V_{MA} ($\epsilon(0/1-) = 0.74$ eV). Among these defects, I_{MA} has very high formation energies at all chemical conditions, as indicated by the dashed lines, and thus will not lead to deep gap states, indicating a high defect tolerance. Sn_I (yellow) has a high formation energy at chemical conditions A and B, MA_I (orange) has a high formation energy at chemical conditions A and B, V_{Sn} (green) has a high formation energy at chemical conditions B and C, and V_{MA} (lime) has a relatively high formation energy at all chemical conditions, see Figure 3.1c. Therefore, the best chemical condition to synthesize MA_2SnI_4 is at B (I-moderate/Sn-moderate), under which undesired Shockley-Read-Hall (SRH) nonradiative recombination centers can be largely prevented in the material.

For $MA_3Sb_2I_9$ (band gap = 2.02 eV), as shown in Figure 3.2d, the defects that create deep transition levels are Sb_I ($\epsilon(2+/4+) = 0.86$ eV) and Sb_I ($\epsilon(1+/2+) = 1.10$ eV and $\epsilon(2+/3+) =$

0.24 eV). Both Sb_I (yellow) and Sb_i (brown) have high formation energies at chemical condition A but very low formation energies at B and C. Therefore, to prevent the deep transition levels in $MA_3Sb_2I_9$, the material should be synthesized under chemical condition A (I-rich/Sb-poor).

The calculated defect formation energies and transition energy levels for all the 29 compounds are shown in Figures B.7-B.35 of Appendix B. To determine the defect tolerance for each compound, we listed the defects that have low formation energies and meanwhile can create deep transition levels in Table B.2-B.6 of Appendix B. The defect tolerance was determined based on the three chemical conditions A, B, and C and also summarized in the Table 3.1. In specific, for one compound, if there is at least one chemical condition that prevents all the kind of defects mentioned above, the compound is determined to have high defect tolerance; if such defects cannot be prevented at any chemical condition, the compound is determined to have low defect tolerance. From this perspective, there are 15 out of 29 compounds that show high defect tolerance.

3.3.3 Absorption Coefficient

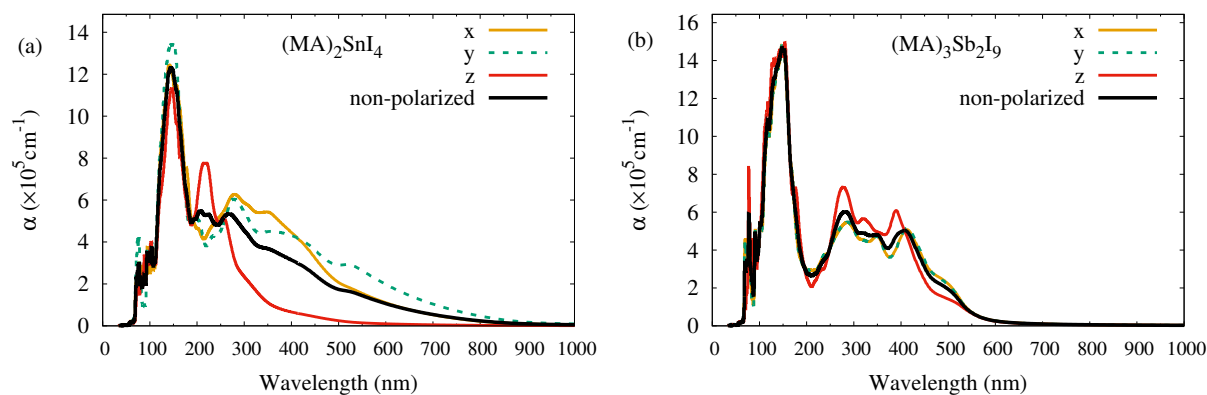


Figure 3.3: Calculated optical absorption coefficients (α) of (a) MA_2SnI_4 and (b) $MA_3Sb_2I_9$ with hybrid functional theory calculations at HSE06 level.

In this section, we investigated the optical absorption coefficients using the following

equation,⁹¹

$$\alpha(\omega) = \sqrt{2} \frac{\omega}{c} \sqrt{\sqrt{\epsilon_1(\omega)^2 + \epsilon_2(\omega)^2} - \epsilon_1(\omega)} \quad (3.7)$$

where ω is the photon frequency, and c is the speed of light in the vacuum. The real part $\epsilon_1(\omega)$ and imaginary part $\epsilon_2(\omega)$ are from the complex dielectric function $\epsilon(\omega)$. The real part $\epsilon_1(\omega)$ follows the Kramer-Kronig relationship, and the imaginary part $\epsilon_2(\omega)$ is calculated from the appropriate momentum matrix elements between the occupied and the unoccupied wave functions within the selection rules over the Brillouin zone. On the basis of the ground state electronic structure calculations at HSE06 level, we obtained $\epsilon_2(\omega)$ and $\epsilon_1(\omega)$ of dielectric function and calculated the optical absorption coefficient of the screened 29 compounds.

The calculated absorption coefficients as a function of wavelength (nm) for the two representative compounds, MA_2SnI_4 and $\text{MA}_3\text{Sb}_2\text{I}_9$, are shown in Figure 3.3a and 3.3b, respectively. The averaged (non-polarized) absorption coefficients at 450 nm are estimated to be $2.4 \times 10^5 \text{ cm}^{-1}$ for MA_2SnI_4 and $3.1 \times 10^5 \text{ cm}^{-1}$ for $\text{MA}_3\text{Sb}_2\text{I}_9$, even higher than $2 \times 10^5 \text{ cm}^{-1}$ for MAPbI_3 . Interestingly, MA_2SnI_4 shows a much higher absorption coefficient along the in-plane (x and y) direction than that along the out-of-plane (z) direction, see Figure 3.3a. The anisotropy of the calculated absorption coefficients resembles that of two-dimensional Ruddlesden-Popper perovskites such as Ge-based compound in our prior work, which is attributed to the two-dimensional structural feature.⁹² However, it is noted that in these quantum well-like perovskites, local fields and excitonic effects have major impacts on their optical properties. To accurately describe optical properties of these materials, DFT calculations with GW approximation and the Bethe-Salpeter equation (BSE) are required,^{94,95} which, however, is more time-consuming. Therefore, to have a direct comparison with the well-studied MAPbI_3 at the same computational level, the ground-state HSE06 calculations were adopted in this work. All the calculated absorption coefficients for the 29 compounds are shown in Figures B.36-B.40 of Appendix B.

3.4 Conclusion

In summary, by using high-throughput first-principles electronic structure calculations, we have systemically studied the stability diagrams, defect tolerance, and absorption coefficients for the screened lead-free 29 candidate hybrid semiconductors for optoelectronic applications. The calculated stability diagram outlines the thermodynamically stable range for the equilibrium growth of the predicted compound with different chemical potentials. The defect tolerance was evaluated from the calculated defect formation energies and transition levels, and the absorption coefficients were calculated from the dielectric functions. These computational studies provide a detailed guide to the further experimental synthesis and characterization of these hybrid compounds, with a potential to facilitate the development of novel optoelectronic devices.

3.5 Acknowledgments

Chapter 3, in full, is a reprint of the material “Stability Diagrams, Defect Tolerance, and Absorption Coefficients of Hybrid Halide Semiconductors: High-Throughput First-Principles Characterization” as it appears in *The Journal of Chemical Physics*. Yuheng Li, Daniel Maldonado-Lopez, Valeria Ríos Vargas, Jingning Zhang, Kesong Yang, 152, 084106, 2020. The dissertation author was the primary investigator and author of this paper.

Chapter 4

Enhancing Ferroelectric Dipole Ordering in the Organic-Inorganic Hybrid Perovskite $\text{CH}_3\text{NH}_3\text{PbI}_3$: Strain and Doping Engineering

In Chapter 2 and Chapter 3, we discuss our high-throughput computational materials design of hybrid lead halide perovskite alternatives for optoelectronics. Starting from this chapter, we discuss materials understanding and optimization of specific properties for individual hybrid halide perovskites. In this chapter, by using first-principles calculations to examine the rotational behavior of MA cations in MAPbI_3 , we show a relationship between the lattice structures and the FE dipole ordering of MA cations. It is found that the MA cations could form a spontaneous FE dipole ordering in tetragonal MAPbI_3 at room temperature. The tendency of the FE formation is strongly related to the ratio of lattice parameters of MAPbI_3 . On the basis of the developed structure-ferroelectric-property relationship, we propose that a biaxial or uniaxial compressive strain and an anion doping with small halogen ions can further enhance the FE dipole ordering.

These findings are in good agreement with the experimental discoveries that high-performance solar cells always incorporate mixed halide hybrid perovskites involving Br or Cl ions. This work may provide some guidelines for rational designs of highly efficient hybrid perovskite solar cells.

4.1 Introduction

Organic-inorganic hybrid perovskites have gained considerable attention in recent years because of their exceptional properties for next-generation photovoltaic applications.^{184,185} Solar cells employing hybrid perovskites have shown an unprecedented rise in power conversion efficiency and have reached a recent record efficiency of 25.2%.⁸ The high power conversion efficiency is largely attributed to the intrinsic optoelectronic properties of hybrid perovskites,^{65,186–189} such as an appropriate band gap matched with the visible-light solar spectrum,^{190,191} high optical absorption,¹⁹² small electron and hole effective masses,¹⁹³ long carrier diffusion length,^{12,158,194–196} and the possible existence of ferroelectric (FE) domains.²⁶ In addition, their low-temperature solution processability makes them substantially cost-effective for large-scale applications.^{197,198}

In spite of promising photovoltaic applications of hybrid perovskites, the origin of the high power conversion efficiency, particularly the role of organic cations, is still an open question.^{19–21} Recent studies have indicated that the superior performance of hybrid perovskites with respect to that of their inorganic counterparts is derived from the organic cations.^{19,22,31,199–202} One of the most prevalent arguments is that intrinsic dipoles of the organic cations are likely to form nanoscale FE domains, which are thought to play a critical role in the efficient separation of photo-induced electron-hole pairs that leads to the high power conversion efficiency.^{22,31,199,201,202} Nevertheless, the movement and ordering of organic cations is still controversial in both theoretical^{22–25} and experimental studies,^{26–31} and far away from a complete understanding.

From the theoretical perspective, the polarization intensity contributed from the organic

cations is particularly quite controversial. Walsh *et al.*'s first-principles calculations indicate a spontaneous formation of FE domains in MAPbI₃ and a large polarization value of 38 $\mu\text{C}/\text{cm}^2$.²² A later first-principle computational study showed that MA cations in tetragonal MAPbI₃ have a preferential alignment along the *c* axis, and the polarization intensity is estimated to be 4.42 $\mu\text{C}/\text{cm}^2$, which is mainly contributed by the MA dipole.²³ The authors also explained that the large discrepancy from the Walsh's study was possibly due to the neglect of the relaxations or the possible inclusion of polarization quanta. Rappe *et al.* reported that the bulk polarization contribution solely from the organic molecular dipole moment is less than 2.5 $\mu\text{C}/\text{cm}^2$, and the PbI₃ inorganic lattice has a major contribution to the polarization.²⁴ Moreover, their calculations showed that the anti-ferroelectric (AFE) tetragonal structure with nearly zero net polarization is more stable than its FE counterpart by 21 meV, implying that the FE domains cannot form spontaneously at room-temperature. On the other hand, Wang *et al.* used first-principles electronic structure calculations to reveal a FE tetragonal structure with polarization of about 8 $\mu\text{C}/\text{cm}^2$, primarily contributed by the organic cations.²⁵

From the experimental perspective, there has been a direct observation of FE domains in high-quality β -MAPbI₃ perovskites using piezoforce microscopy.²⁶ A later experimental study reported the FE polarization behavior in the MAPbI₃ perovskite crystal, and confirmed the formation of spontaneous polarization even without the presence of an electric field.²⁷ A ferroelectric hysteresis and polar domains in tetragonal MAPbI₃ were also observed through dielectric response and chemical etching, respectively.³¹ On the contrary, Weller *et al.* investigated the full structure of MAPbI₃ using neutron powder diffraction and found that the cations were disordered in the tetragonal phase,²⁸ implying no polarization. Sharada *et al.* claimed a nonpolar or centrosymmetric structure of MAPbI₃ using a time-resolved pump-probe measurement of the second harmonic generation efficiency.²⁹ Similarly, in the case of MAPbBr₃, it was found the compound is centrosymmetric and nonpolar and thus could not be ferroelectric by using a second-harmonic-generation spectroscopy.³⁰ All these irreconcilable experimental results indicate

that a more comprehensive computational and theoretical study is essential to understand whether the organic cations can form a ferroelectric dipole ordering, and to further elucidate the roles of organic cations in the hybrid perovskite solar cells.

In this work, we explore ferroelectric dipole ordering in MAPbI₃ using first-principles calculations. This article is organized as follows. First, we discuss two types of rotation modes of MA cations: in-phase rotation and out-of-phase rotation. Next, we explore the possibility of spontaneous formation of FE dipole ordering in tetragonal MAPbI₃. Finally, we propose two nanoengineering approaches to further enhance the FE dipole ordering, *i.e.*, strain engineering and doping engineering.

4.2 Computational Details

First-principles density functional theory (DFT) calculations were performed using the Vienna *Ab-initio* Simulation Package (VASP).^{179,203} The Projector Augmented Wave (PAW) pseudopotential was used for describing electron-ion interactions,¹⁸⁰ and the Generalized Gradient Approximation (GGA) parameterized by Perdew-Burke-Ernzerhof (PBE) was used for treating electron-electron exchange-correlation functional.¹⁴⁹ A cut-off energy of 400 eV for the plane-wave basis set was used, and Γ -centered $6 \times 6 \times 6$ and $4 \times 4 \times 2$ k -point meshes were used for cubic and tetragonal structures, respectively. Lattice parameters and atomic positions were optimized until all components of the residual forces were smaller than 0.01 eV/Å, and the convergence threshold for self-consistent-field iteration was set at 10^{-5} eV.

4.3 Results and Discussion

4.3.1 In-Phase Rotation

We begin by studying the in-phase rotational behavior of MA cations in cubic and tetragonal MAPbI₃ phases, respectively. Here, an in-phase rotation refers to a rotation of all the MA cations in synchrony. In this work, the experimental lattice parameters of $a = 6.31 \text{ \AA}$ for the cubic phase,¹⁰⁷ and $a = 8.80 \text{ \AA}$, $c = 12.99 \text{ \AA}$ for the tetragonal phase²⁰⁴ were used. The calculated dipole moment of a single MA cation is about 2.38 D, with a direction from N to C, which is consistent with previous reported values of 2.29 D.²² It is noted that, in principle, there are numerous in-phase rotation modes for the MA cations in MAPbI₃. To simplify the computational models, we consider two types of in-phase rotation modes: i) MA cations rotate around their C-N axes and keep their dipole direction fixed (non-flipping mode), and ii) MA cations rotate around their centers and flip their dipole direction (flipping mode). To explore the MA rotational behaviors, we calculated the total energy changes (ΔE) as a function of the rotation angles of MA cations (Figure 4.1). For the non-flipping mode, considering the C_{3v} symmetry of the MA cation, we performed total energy calculations for each structure with MA rotation in discrete steps ranging from 0 to 120° (see Figure 4.1a for cubic phase and Figure 4.1c for tetragonal phase). For the flipping mode, the rotation range of the MA is from 0 to 180° (Figure 4.1b and Figure 4.1d). Our calculations reveal the following two conclusions:

(1) For the non-flipping rotation mode (Figure 4.1a and 4.1c), ΔE shows similar dependence on θ in the cubic and tetragonal phases. In each case, the rotation energy barrier is smaller than 5 meV (Figure 4.1a' and 4.1c'), indicating that the non-flipping rotation mode is accessible in both phases. The energy barrier in the cubic phase is slightly lower than that in the tetragonal phase (2 meV versus 4 meV), which is due to a more spacious framework around the MA cation in the cubic phase structure. Interestingly, the rotation has a period of 90° in both the cubic and tetragonal phases, which is due to the quadrangle environment of the inorganic frameworks.

(2) For the flipping rotation mode (Figure 4.1b and 4.1d), the rotation energy barrier is about 6 meV in cubic phase and 160 meV in the tetragonal phase (Figure 4.1b' and 4.1d'), indicating that the flipping rotation mode is accessible in the cubic phase but energetically prohibited in the tetragonal phase. Moreover, the calculated value of ΔE versus θ for the tetragonal phase shows a deep trough around 50° , indicating that MA cations tend to stay at an orientation of around 50° with respect to the c -axis in the tetragonal phase.

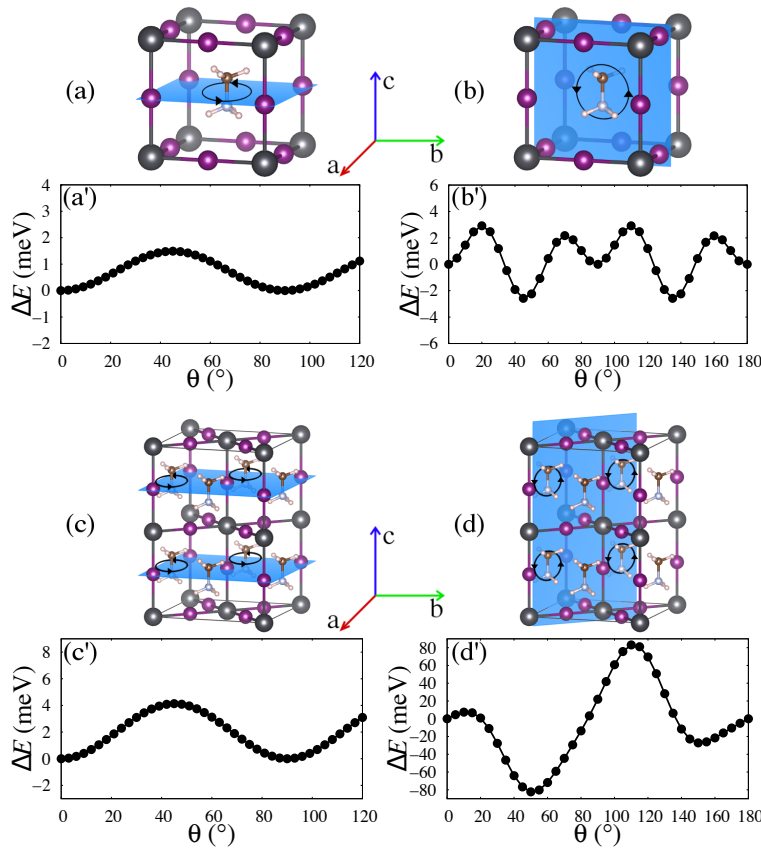


Figure 4.1: Schematic illustration of the rotation modes for the MA cations (a-d) and corresponding total energy change (ΔE) as a function of the rotation angle (θ) (a'-d'). (a-d) shows the MA rotation in (a) cubic (001) rotation plane, (b) cubic (100) rotation plane, (c) tetragonal (001) rotation plane, and (d) tetragonal (110) rotation plane. The blue shadows and the black arrows in the blue shadows illustrate the rotation planes and rotation directions of MA cations, respectively. The unit cells are shown in standard orientations of crystal shape using VESTA.²⁰⁵

Next, we analyze the origin of the different energy barriers of flipping rotation in cubic (Figure 4.1b) and tetragonal (Figure 4.1d) phases from the perspective of cell geometry. The

tetragonal MAPbI₃ unit cell can be considered consisting of four sub-unit-cells, each of which contains one MA cation (Figure 4.1d). The lattice parameters of each sub-unit-cell can be calculated from that of the MAPbI₃ unit cell using the equations: $a' = a/\sqrt{2} = 8.80/\sqrt{2} = 6.22$ Å, and $c' = c/2 = 12.99/2 = 6.50$ Å. This sub-unit-cell is more slender than the cubic unit cell with lattice constant $a = 6.31$ Å, (Figure 1b). In other words, each sub-unit-cell in the tetragonal phase has a shorter bottom edge (a') but longer vertical edge (c') than the cubic unit cell, like experiencing a compressive strain in the bottom plane. As a result, as the C-N bond of the MA cation rotates closer to an orientation parallel to the bottom plane, the MA cation tends to undergo greater steric repulsive forces from the inorganic framework, thus leading to the higher energy barrier. On the basis of this analysis, we can infer a general rule regarding the flipping rotation of MA cations: the larger the cell aspect ratio (c/a) is, the less likely MA flipping rotation becomes. As discussed later, this general rule will be applied to enhance the ferroelectric dipole ordering of MA cations.

4.3.2 Out-of-Phase Rotation

In the tetragonal MAPbI₃ unit cell, in addition to the in-phase flipping rotation, there is also out-of-phase flipping rotation that refers to a rotation of MA cations out of synchrony. For a dipole ordering study, an out-of-phase rotation model can be simplified such that only two out of the total four MA cations rotate. In other words, a pair of MA cations in the MAPbI₃ unit cell rotate, while the other pair of MA cations are fixed. The difference between in-phase and out-of-phase rotations can be explained as below. For in-phase rotation, dipoles of all MA cations are always in alignment and form a FE state. For out-of-phase rotation, the relative angle between rotating and fixed MA cations is dynamic. When the angle reaches 180°, the dipoles of the rotating MA pair and the fixed MA pair completely cancel out and yield an AFE state with zero net polarization. A rotation process with the angle changing from 0° to 180° represents a FE-to-AFE transition. The two rotating MA cations can be in the same column (Figure 4.2a),

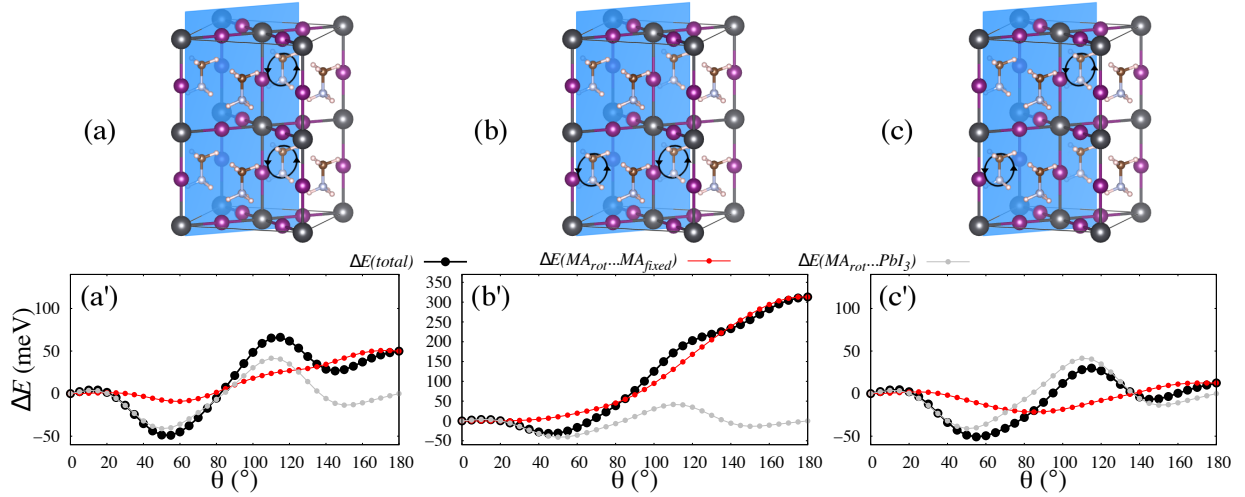


Figure 4.2: Calculated total energy change, $\Delta E(total)$, as a function of MA out-of-phase rotation angle, θ , in the tetragonal $MAPbI_3$. (a) FE to AFE1, (b) FE to AFE2, and (c) FE to AFE3. The initial state of the four MA cations is set as FE ordering, and as θ increases up to 180° , the final state becomes AFE (three AFE states are considered here, labeled as AFE1, AFE2, and AFE3, respectively). Black curves show the total energy change, labeled as $\Delta E(total)$. Red curves show the total energy change induced by interaction between rotating and fixed MA cations, labeled as $\Delta E(MA_{rot} \cdots MA_{fixed})$. Grey curves show the total energy change induced by interaction between rotating MA cations and the PbI_3 inorganic framework, labeled as $\Delta E(MA_{rot} \cdots PbI_3)$.

in the same row (Figure 4.2b), or in the same diagonal (Figure 4.2c), and their (110) rotation plane is highlighted in blue. Their corresponding AFE states are labeled as AFE1, AFE2, and AFE3, respectively. To study whether these FE-to-AFE transitions are energetically accessible, we calculated total energy changes for out-of-phase rotation models, from the FE state to the three AFE states. In our calculations, to clearly show the pure contribution of MA rotation to the total energy change, the PbI_3 inorganic framework is unrelaxed. The total energy changes during these FE-to-AFE transitions are shown in Figures 4.2a', b', and c'. Notably, the total energy change, $\Delta E(total)$, in an out-of-phase rotation model comes from two parts: (1) the interaction between rotating MA cations and PbI_3 inorganic framework, and (2) the interaction between rotating and fixed MA cations. The total energy changes induced by these two interactions are labeled as $\Delta E(MA_{rot} \cdots PbI_3)$ and $\Delta E(MA_{rot} \cdots MA_{fixed})$, respectively. As a result, we have the

following equation.

$$\Delta E(total) = \Delta E(MA_{rot} \cdots PbI_3) + \Delta E(MA_{rot} \cdots MA_{fixed}) \quad (4.1)$$

The total energy change in the out-of-phase rotations is different from that in the in-phase rotation, because the latter comes exclusively from the interaction between the rotating MA cations and PbI_3 inorganic framework. To clearly show the contribution of interaction between rotating and fixed MA cations in the FE-to-AFE transitions, we calculated $\Delta E(MA_{rot} \cdots MA_{fixed})$ from equation (1). In this equation, $\Delta E(MA_{rot} \cdots PbI_3)$ is half the value of the energy change in the in-phase rotation mode (Figure 4.1d). This is because the $\Delta E(MA_{rot} \cdots PbI_3)$ here is induced by the interaction between PbI_3 and only two rotating MA cations, instead of four rotating MA cations in the in-phase rotation mode. The calculated $\Delta E(total)$, $\Delta E(MA_{rot} \cdots PbI_3)$, and $\Delta E(MA_{rot} \cdots MA_{fixed})$ are plotted in Figure 4.2 as black, grey, and red curves, respectively. From these results, we can get the following conclusions.

(1) The total energy change, $\Delta E(total)$ (black curves in Figure 4.2), has barriers of about 120, 320, and 80 meV for transitions from the FE state to AFE1, AFE2, and AFE3 states, respectively. These barriers are far above kT at room temperature (26 meV), indicating that all the three FE-to-AFE transitions are energetically prohibited. For each case, there is an energy trough around 50° and an energy peak around 110° . This trough-peak pattern is similar to that of $\Delta E(MA_{rot} \cdots PbI_3)$ (grey curves in Figure 4.2), indicating that the pattern is mainly caused by interaction between rotating MA cations and the PbI_3 inorganic framework.

(2) $\Delta E(MA_{rot} \cdots MA_{fixed})$ has energy barriers of about 60, 300, and 30 meV for transitions from the FE state to AFE1, AFE2, and AFE3 states, respectively. (red curves in Figure 4.2) These barriers are above kT as well, although they are solely induced by the interaction between rotating and fixed MA cations. This provides more direct evidence that the FE-to-AFE transitions are inaccessible at room temperature. The trough-peak pattern of $\Delta E(total)$ and $\Delta E(MA_{rot} \cdots PbI_3)$ is

absent in $\Delta E(MA_{rot} \cdots MA_{fixed})$, indicating that this pattern is irrelevant to the interaction between rotating and fixed MA cations. Specifically, for the FE-to-AFE1 and FE-to-AFE3 transitions, they have a shallow trough around 60° (Figure 4.2a') and 85° (Figure 4.2c'), respectively. Each of these angles represents an energetically favored direction of the corresponding rotating MA pair. This indicates that, in these two out-of-phase rotations, the rotating and fixed MA pairs are not in a perfect alignment at their ground states, and they can yield a non-zero net FE polarization. For the FE-to-AFE2 transition, the red curve shows a monotonic increase in energy from 0° to 180° (Figure 4.2b'). This indicates that, in this out-of-phase rotation, the rotating MA pair tends to stay at 0° , forming a FE dipole ordering with the still MA pair. In short, the out-of-phase MA rotations which result in a FE-to-AFE transition are energetically prohibited. For all the three out-of-phase rotations, MA cations in tetragonal MAPbI₃ tend to form the FE state with non-zero net polarization.

4.3.3 Spontaneous Ferroelectric Dipole Ordering

Table 4.1: Relaxed lattice parameters of the MAPbI₃ with different MA ordering configurations and their discrepancies (δ) with the experimental values.

Phase	a (Å)	b (Å)	c (Å)	α (°)	β (°)	γ (°)	δ
Expr ⁶⁵	8.85	8.85	12.64	90.00	90.00	90.00	–
FE	8.78	8.79	13.04	89.20	89.09	89.56	1.17%
AFE1	8.80	8.80	13.04	88.62	88.55	89.82	1.27%
AFE2	8.76	8.98	12.85	87.92	87.18	89.96	1.61%
AFE3	8.93	8.91	12.70	86.99	87.09	89.23	1.58%

The preceding results based on the unrelaxed tetragonal MAPbI₃ lattice show that the MA cations tend to form FE states. In reality, however, the structural distortion of PbI₃ could significantly affect the total energy of this material and the MA orientations. Hence, to accurately determine MA orientation, cell geometry, and energetic advantage of the FE state, we also carried out total energy calculations for the fully relaxed structures with MA cations in all the FE and

AFE states. This procedure involves two steps. First, on the basis of a relaxed FE structure, we produced three AFE structures by exchanging C and N atoms in the two corresponding MA cations, and then fully relaxed all these structures. Their optimized lattice parameters are listed in Table 4.1, along with the experimental values. To determine which structure among the four states is closest to the experiment, we define *lattice discrepancy* (δ) using following equation,

$$\delta = \frac{1}{6} \sum \frac{|p - p_{expr}|}{p_{expr}} \quad (4.2)$$

in which p represents the six lattice parameters. The calculated δ of the four states are listed in Table 4.1. Our results show that the optimized lattice parameters of the FE state has the smallest δ of 1.17%, indicating that this set of lattice parameters is closest to the experimental values.

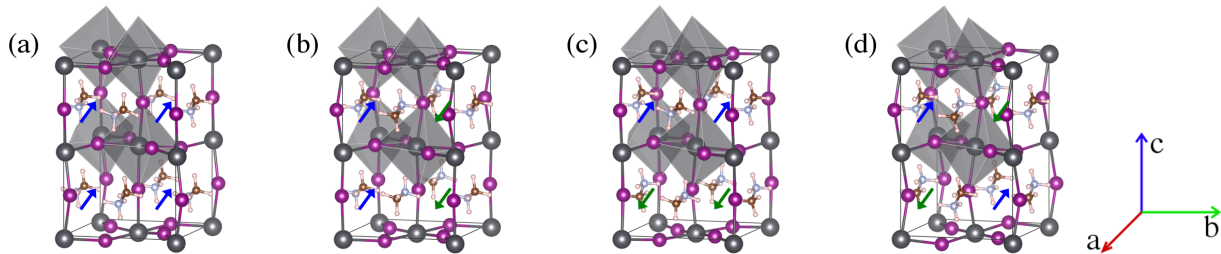


Figure 4.3: Relaxed structures with different MA ordering configurations: (a) FE, (b) AFE1, (c) AFE2, and (d) AFE3. Blue arrows show MA dipoles pointing up, and green arrows show MA dipoles pointing down.

Next, we took the lattice parameters of the FE state as a standard for best simulating actual case. The three AFE states were modeled again by manually exchanging corresponding C and N atoms in the fully relaxed FE structure. All the atomic positions of the FE and three AFE structures were relaxed with their lattice parameters fixed. This procedure ensures us to accurately produce the energy difference between AFE and FE states. All the optimized structures are shown in Figure 4.3.

After structural optimization, the MA cations tend to keep their original configurations in all the FE and AFE structures. MA cations with their dipoles pointing up are highlighted in

blue, while those with their dipoles pointing down are highlighted in green (Figure 4.3). In the FE structure, all four MA cations point up along the [111] direction (Figure 4.3a). In the AFE structures, two MA cations point up and the other two point down, yielding a polarization of zero (Figure 4.3b, 4.3c, and 4.3d). It is also found that there is distortion in PbI_3 inorganic framework for all four optimized structures, and that AFE3 has the most severe distortion. Our results show that FE is the most stable state, and is energetically more favorable than the three AFE states by 40, 36, and 65 meV, respectively. These results indicate that tetragonal MAPbI_3 is inclined to form the FE state and has a net polarization from ferroelectric dipole ordering. However, the energy difference between the most stable AFE state and the FE state is only about 36 meV, close to kT (26 meV) at room temperature. This indicates that the FE state's energetic advantage is relatively small, and thus that AFE states might be accessible with slight perturbations at ambient conditions. In other words, the weak inclination of FE state can be readily eliminated and the FE characteristics can fall below experimental detection limit. This could be a reason for why some previous experimental studies showed no ferroelectricity.^{25,29}

It is noted that the structures in our calculations represent ideal configurations with MA either completely in phase (FE) or completely out of phase (AFE) with respect to their neighbors. In reality, a wide range of possible structures exist between these two extreme cases, although these ideal FE and AFE models can give a direct indication of ferroelectric dipole ordering. Our results are consistent with a previous theoretical study²³, in which they proved a preferential MA alignment in tetragonal MAPbI_3 through comparing energy of three intermediate configurations. In addition, by using the calculated dipole moment of 2.38 D for a single MA cation, we calculated the polarization value of tetragonal MAPbI_3 contributed by MA's intrinsic dipole moment and determined a value of $3.15 \mu\text{C}/\text{cm}^2$. This value is close to previous results of $4.42 \mu\text{C}/\text{cm}^2$ ²³ and $8 \mu\text{C}/\text{cm}^2$ ²⁵. Both of these results show that the main contribution to the overall polarization is the dipole alignment of MA cations rather than distortion of the PbI_3 inorganic framework.

4.3.4 Strain Engineering

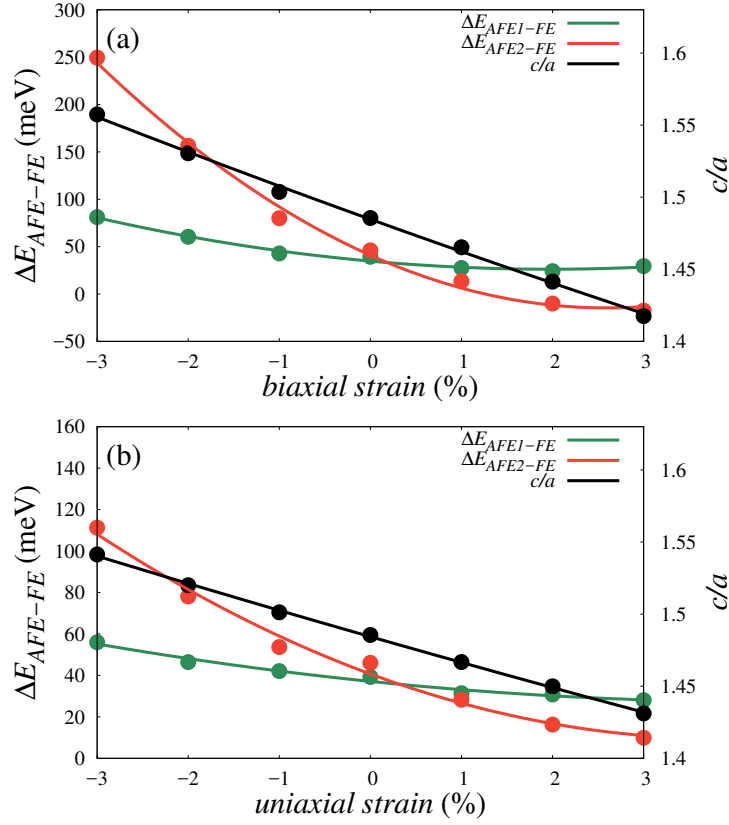


Figure 4.4: Energy difference between each AFE structure and the FE structure (ΔE_{AFE-FE}) (in green and red) and cell aspect ratio (c/a) (in black) versus (a) biaxial strains, and (b) uniaxial strains.

As discussed earlier, the MA flipping rotation is strongly related to cell aspect ratio (c/a) of MAPbI_3 . As c/a becomes larger, the MA flipping rotation becomes energetically less likely, implying a larger energy difference between an AFE state and FE state (this energy difference is defined as ΔE_{AFE-FE}). On the basis of this finding, one might expect that a compressive biaxial or uniaxial strain can enlarge c/a of tetragonal MAPbI_3 ^{45,206} and enhance the FE state's energetic advantage over the AFE states. To verify this hypothesis, we calculated ΔE_{AFE-FE} and c/a with respect to biaxial strain and uniaxial strain from -3% to $+3\%$, with negative (positive) values defined as compressive (tensile) strain. As discussed earlier, the AFE3 configuration has a very high energy and severe distortion, we therefore exclude this configuration in our following

discussion. In our calculations, lattice parameters in ab -plane are fixed, while c and all the atomic positions are fully relaxed.

The calculated energy difference between AFE1 (AFE2) and the FE state is shown in green (red) in Figure 4.4, labeled as $\Delta E_{AFE1-FE}$ ($\Delta E_{AFE2-FE}$). The calculated c/a is shown in black for structural analysis. Note that the c/a are extracted from the FE state, because FE and AFE states under the same strain have negligible differences in c after optimization. Our calculations reveal the following conclusions.

(1) For both biaxial strain and uniaxial strain cases, ΔE_{AFE-FE} generally decreases from compressive strain to tensile strain, and $\Delta E_{AFE2-FE}$ decreases faster than $\Delta E_{AFE1-FE}$. Under compressive strains (from -3% to 0%), the AFE1 state is energetically more favorable than the AFE2 state, and $\Delta E_{AFE1-FE}$ can be as large as 81 meV (for biaxial strain) or 56 meV (for uniaxial strain), implying robust ferroelectric dipole orderings. Under tensile strains (from 0% to $+3\%$), the AFE2 state has a lower total energy, and $\Delta E_{AFE2-FE}$ can be lower than -15 meV (for biaxial strain) or close to zero (for uniaxial strain), implying paraelectric dipole orderings.

(2) The aspect ratio c/a also decreases from compressive strain to tensile strain, showing a strong correlation with ΔE_{AFE-FE} for both biaxial strain and uniaxial strain cases. As a and b decrease under biaxial compressive strain (as a decreases under uniaxial compressive strain), c and c/a always increase. The consequent larger c/a , as indicated earlier, makes MA flipping rotation more difficult. As expected, the FE state's energetic advantage over the AFE states is enhanced based on change of c/a .

In short, compressive biaxial or uniaxial strain increases the energetic advantage of the FE state over the AFE states, while tensile strain decreases it. Hence, strain engineering is one way to enhance the tendency of ferroelectric dipole ordering in tetragonal MAPbI₃.

4.3.5 Doping Engineering

In addition to strain engineering, herein we propose another way to enhance ferroelectric dipole ordering through doping engineering. That is, to substitute I with smaller halogen anions, such as Br or Cl. This hypothesis is based on the argument that substitutional doping with smaller ions exerts natural compressive strain on unit cells.^{207,208} Moreover, doping can also induce lattice strains that are less possible through the application of external forces.²⁰⁹ There are two kinds of I sites in tetragonal MAPbI₃: one on the PbI₂ layers, and the other on the MAI layers. Br (Cl) doping on the PbI₂ layers shortens Pb-halogen bonds in the *ab*-plane, and reduces the *a* and *b* lattice parameters; while the doping on the MAI layers shortens Pb-halogen bonds along the *c* axis, and reduces the *c* lattice parameter. Therefore, in order to increase *c/a*, the ideal doping should be on the PbI₂ layers rather than the MAI layers. In fact, our calculations show that Br doping on the PbI₂ layers is energetically more favorable than that on the MAI layers by 16 meV. Additionally, there are eight I anions on the PbI₂ layers per unit cell while four on the MAI layers, implying that there is a higher probability for the doping to substitute I on the PbI₂ layers. These findings indicate that substitutional Br (Cl) anions prefer to go to the PbI₂ layers, and are able to increase *c/a*. By taking Br-doped MAPbI₃ as an example, we calculated $\Delta E_{AFE1-FE}$, $\Delta E_{AFE2-FE}$, and *c/a*. These values are plotted with respect to doping concentration (c_{Br}) in Figure 4.5a. Our results indicate the following conclusions.

(1) The energy differences, $\Delta E_{AFE1-FE}$ and $\Delta E_{AFE2-FE}$, first increase then decrease as c_{Br} increases, and they have a maximum value at $c_{Br} \approx 60\%$. At the peak, the AFE1 state has a lower total energy than the AFE2 state. The corresponding $\Delta E_{AFE1-FE}$ is as large as 75 meV, which means that the FE state can be stabilized at room temperature. At $c_{Br} > 60\%$, ΔE_{AFE-FE} decreases. At $c_{Br} = 100\%$, the compound becomes MAPbBr₃, and ΔE_{AFE-FE} has a minimum value of 4.88 meV, indicating that there is no spontaneous dipole alignment in pristine MAPbBr₃. In fact, a prior experimental study on MAPbBr₃ showed that MAPbBr₃ is centrosymmetric and non-polar,³⁰ which is in excellent agreement with our results. Overall, in the wide doping

concentration range, $30\% < c_{Br} < 80\%$, the FE state has a larger energetic advantage than the AFE states relative to the undoped MAPbI_3 .

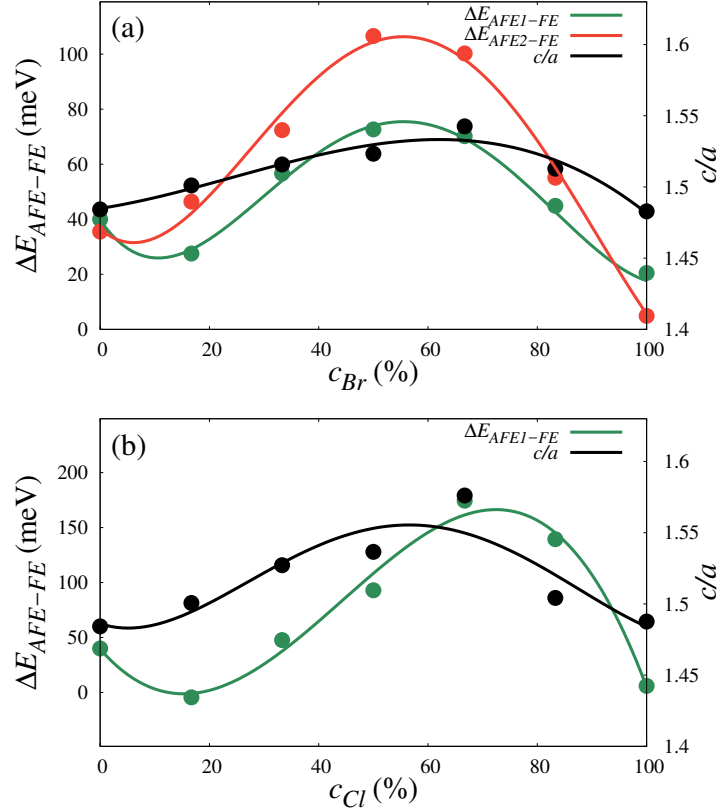


Figure 4.5: Energy difference between each AFE structure and the FE structure (ΔE_{AFE-FE}) (in green and red) and cell aspect ratio (c/a) (in black) versus (a) Br doping concentration (c_{Br}) and (b) Cl doping concentration (c_{Cl}).

(2) The cell aspect ratio, c/a , has a similar trend as ΔE_{AFE-FE} and has a maximum value at $c_{Br} = 67\%$. This phenomenon can be explained as follows. The Br anions were first doped in the PbI_2 layers at $0\% \leq c_{Br} \leq 67\%$, which is similar to the case of ab -plane compressive strain. The Br doping in the PbI_2 layers leads to a reduction of the lattice parameters a and b , and thus increases c/a . The increase in c/a enhances the relative stability of the FE state. At $c_{Br} > 67\%$, Br anions begin to substitute I anions in the MAI layers. The shortened Pb-halogen bonds along the c axis decreases c/a . As c_{Br} increases up to 100%, c/a is eventually close to the value of pristine MAPbBr_3 . In one word, the similar trend of c/a and ΔE_{AFE-FE} implies that the doping

engineering has similar effect as the strain engineering.

Besides Br doping, we also calculated ΔE_{AFE-FE} and c/a for Cl doping. The results are plotted with respect to Cl doping concentration (c_{Cl}) in Figure 4.5b. c/a and $\Delta E_{AFE1-FE}$ show a similar trend as the Br doping results. One notable difference from Br doping is that Cl doping induces more significant changes in c/a and ΔE_{AFE-FE} . We attribute this difference to the smaller size of Cl ions compared to Br ions. In addition, because Cl ions are substantially smaller than I ions, there is severe structural distortion of Cl-doped MAPbI₃ structures, especially for the AFE2 structures. Due to this distortion, total energy of the AFE2 structures and resulting $\Delta E_{AFE2-FE}$ values are unreasonably high. When considering energetic advantage of the FE state, only the more stable AFE state (AFE1) matters. Therefore, the $\Delta E_{AFE2-FE}$ values are not plotted here.

In short, substitutional anion doping with smaller anions effectively enhances the tendency of FE dipole ordering in tetragonal MAPbI₃. In fact, prior studies have shown that Cl doping reduces charge recombination in lead iodide hybrid perovskites,^{210,211} which support our doping engineering results. Moreover, we expect that, by substitutional cation doping such as partially replacing MA with larger FA cations, the c -axis and c/a will also increase, and a similar effect of FE dipole ordering enhancement can also be achieved. Interestingly, this conclusion of dopant-mediated FE enhancement shows good agreement with the fact that high-performance solar cells always incorporate mixed-halide hybrid perovskites such as MAPbI_{3-x}Cl_x, MAPbI_{3-x}Br_x, and MA_{1-x}FA_xPbI₃.²¹²⁻²¹⁴

4.4 Conclusion

In summary, ferroelectric dipole ordering of MA cations in MAPbI₃ were studied from first-principles calculations. First, we investigated two types of MA cation rotations, including in-phase and out-of-phase rotations, and calculated their energy barriers. Second, the energetic

advantage of the FE state relative to the AFE states was determined. Last, we explored means to further enhance the FE dipole ordering. The results can be summarized as below:

(1) The in-phase non-flipping rotation of MA cations is accessible in both cubic and tetragonal phases, while the in-phase flipping rotation is energetically prohibited in the tetragonal phase. The larger the cell aspect ratio c/a is, the less likely MA flipping rotation becomes.

(2) The out-of-phase flipping rotation of MA cations in tetragonal MAPbI₃ tends to form FE dipole ordering.

(3) The FE dipole ordering state is energetically more favorable than the AFE states, with a small energetic advantage of 36 meV. Polarization contributed by FE dipole ordering in tetragonal MAPbI₃ was calculated to be 3.15 $\mu\text{C}/\text{cm}^2$.

(4) Based on change of c/a , compressive strain and substitutional doping with smaller anions can both enhance the energetic advantage of the FE dipole ordering state in tetragonal MAPbI₃.

In short, this work reveals the rotational behavior of MA cations and their spontaneous formation of FE dipole ordering in tetragonal MAPbI₃, and proposes strain engineering and doping engineering as two approaches to enhancing tendency of the FE state formation. We feel that this work provides some key insights into design principles of high-efficiency solar cells based on hybrid halide perovskites.

4.5 Acknowledgments

Chapter 4, in full, is a reprint of the material “Enhancing Ferroelectric Dipole Ordering in Organic–Inorganic Hybrid Perovskite CH₃NH₃PbI₃: Strain and Doping Engineering” as it appears in The Journal of Physical Chemistry C. Yuheng Li, Maziar Behtash, Joseph Wong, Kesong Yang, 122, 177-184, 2018. The dissertation author was the primary investigator and author of this paper.

Chapter 5

First-Principles Investigation of Epitaxial Stabilization and Strain Engineering of α -FAPbI₃

In Chapter 4, we discuss first-principles investigation of ferroelectric dipole ordering property in MAPbI₃, and propose strain and doping engineering as effective ways to enhance the unique property. In this chapter, we discuss energetic and electronic properties of FAPbI₃, and how epitaxial growth and strain engineering improve these properties. Note that this chapter only reports the first-principles calculations extracted from our experimental and theoretical collaboration. Both of Chapter 4 and Chapter 5 represent first-principles materials understanding and optimization of hybrid halide perovskites for optoelectronic applications.

5.1 Introduction

Formamidinium lead iodide (FAPbI₃) has a high-temperature photoactive α phase adopting the cubic perovskite crystal structure. However, α -FAPbI₃ suffers from rapid and spontaneous

phase transition to the photoinactive δ -FAPbI₃ at low temperature, restricting its application in optoelectronic devices.⁶ The current stabilization methods for α -FAPbI₃ mainly utilize doping of small ions, which compensate the internal strain that drives the phase transition.²¹⁵ However, doping of external chemical species would naturally alter the material properties, and could result in undesired electronic properties like enlarged bandgaps.²¹⁶

Unlike the conventional doping methods, epitaxial stabilization is a novel stabilization method for halide perovskites.⁶ In heterogeneous growth, coherent interfaces can form if the film and the substrate are close in structure and dimension. Such coherent interfaces show substantially lower interfacial energy than incoherent ones. Because the system always minimizes its Gibbs free energy, the interface can make the nucleus crystal structure of the grown film material different from its equilibrium bulk structure. In this case, epitaxial stabilization is achieved.²¹⁷ Through compositional control of substrates, the epitaxial growth could also achieve strain engineering of the structural and electronic properties of the film material. In this study, we use first-principles calculations to investigate the thermodynamic terms in nucleation of α - and δ -FAPbI₃ on MAPbBr₃ substrate. The difference between the two systems' total energy change during the nucleation processes demonstrate epitaxial stabilization of α -FAPbI₃. In addition, we explore the effect of epitaxial strains on the structural and electronic properties of the halide perovskites.

5.2 Computational Details

First-principles density functional theory calculations were performed using the Vienna ab initio Simulation Package (VASP).¹⁷⁹ Electron-ion interactions were described using the Projector Augmented Wave pseudopotential.¹⁸⁰ The electron-electron exchange-correlation functional was treated using the Generalized Gradient Approximation parametrized by Perdew, Burke and Ernzerhof.⁸³ For bandgap calculations, spin-orbit coupling was incorporated owing to the heavy

element Pb, and the hybrid functionals within Heyd-Scuseria-Ernzerhof formalism with 25% Hartree-Fock exchange were employed. A cutoff energy of 400 eV for the plane-wave basis set was used. All structures were fully optimized until all components of the residual forces were smaller than 0.01 eV \AA^{-1} . The convergence threshold for self-consistent-field iteration was set at 10^{-5} eV . For optimization of the cubic lattice parameter, a Γ -centred $3 \times 3 \times 3$ k -point mesh was used. A denser k -point mesh of $4 \times 4 \times 4$ was used to obtain accurate energies and electronic structures for strained cells. For optimization and static calculations of the heterostructural models, Γ -centred $4 \times 4 \times 1$ and $5 \times 5 \times 1$ k -point meshes were used, respectively.

5.3 Results and Discussion

5.3.1 Epitaxial Stabilization of α -FAPbI₃

First-principles calculations were performed to investigate epitaxial stabilization of α -FAPbI₃ with respect to δ -FAPbI₃ on MAPbBr₃ substrates. A typical model of epitaxial stabilization calculations compares the total energy changes of nucleating the two phases on the substrate.²¹⁸ Equation (1) shows an expression of this model for this specific system:

$$\Delta E^{\alpha-\delta} = (\Delta E_f^\alpha - \Delta E_f^\delta)d + (\Delta E_s^\alpha - \Delta E_s^\delta)d + (\sigma^{\alpha||S} - \sigma^{\delta||S}), \quad (5.1)$$

where the terms on the right-hand side for phase i ($i = \alpha, \delta$) are bulk formation energy (ΔE_f^i), strain energy (ΔE_s^i), and interfacial energy ($\sigma^{i||S}$, S means substrate) terms. Here, we use area-specific bulk energy terms (ΔE_f^i and ΔE_s^i) by setting the film thickness to $d = 1 \text{ nm}$. The sum of the three energy-difference terms is the total energy difference between strained α -FAPbI₃ and δ -FAPbI₃ ($\Delta E^{\alpha-\delta}$). A negative $\Delta E^{\alpha-\delta}$ indicates that growth of α -FAPbI₃ is energetically more favorable than δ -FAPbI₃ on the MAPbBr₃ substrate, and thus the metastable α -FAPbI₃ is epitaxially stabilized. Calculation details and results for each energy term are discussed below.

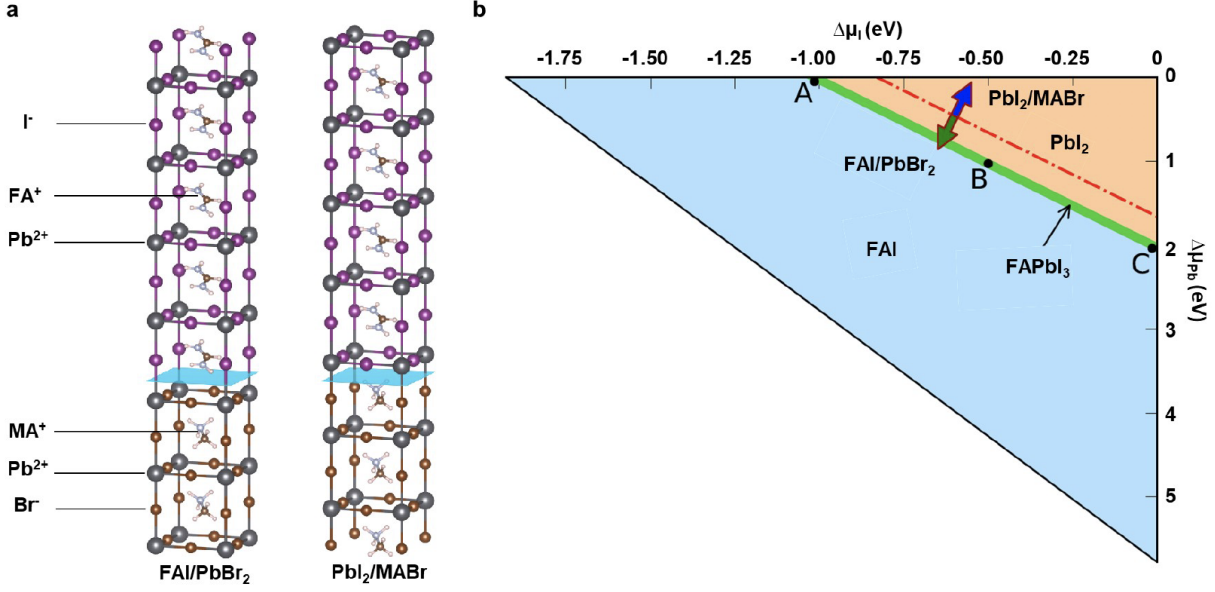


Figure 5.1: First-principles calculations of epitaxial stabilization. a, Schematic heterostructural models used to calculate the epitaxial α -FAPbI₃ (001)/MAPbBr₃ (001) interface. The two interface terminations studied are FAI/PbBr₂ and PbI₂/MABr. In each model, the blue plane indicates the interface, the upper section indicates the FAPbI₃ film, and the lower section indicates the MAPbBr₃ substrate. b, Calculated phase diagram for α -FAPbI₃ and epitaxial α -FAPbI₃ (001)/MAPbBr₃ interface. The long, narrow region marked in green depicts the thermodynamically stable range for equilibrium growth of α -FAPbI₃ under different I and Pb chemical potentials. Outside this region, the compound decomposes into FAI or PbI₂. Three representative points A ($\Delta\mu_I = -1.02$ eV, $\Delta\mu_{Pb} = 0$ eV), B ($\Delta\mu_I = -0.50$ eV, $\Delta\mu_{Pb} = -1.03$ eV), and C ($\Delta\mu_I = 0$ eV, $\Delta\mu_{Pb} = -2.04$ eV) are selected for calculating the interfacial energy. The red dashed line separates the phase diagram into stability regions of the two different interfacial terminations in a. μ represents the chemical potentials of the corresponding atoms.

The bulk formation energy (ΔE_f^i) is the energy difference between bulk i -FAPbI₃ and its elemental components, as shown in Equation (2):

$$\Delta E_f^i = E_i - E_{FA} - E_{Pb} - 3E_I. \quad (5.2)$$

Because we are dealing with polymorphs with the same composition, the elemental components for both α and δ phases are the same. The total energy of the FA⁺ cation is calculated based on an isolated molecule. Total energies of Pb and I are calculated using their most stable crystal structures, with a space group of $Fm\bar{3}m$ and $Cmce$, respectively. By setting the film thickness

to 1 nm, we get area-specific bulk formation energies $\Delta E_f^\alpha = -2.279 \times 10^{-1} \text{ eV \AA}^{-2}$ and $\Delta E_f^\delta = -2.31 \times 10^{-1} \text{ eV \AA}^{-2}$. The results indicate that δ -FAPbI₃ is more stable, which agrees with the experimental findings that δ -FAPbI₃ is more stable than α -FAPbI₃ at room temperature.²¹⁹

The strain energy of i -FAPbI₃ (ΔE_s^i) is induced by constraints from the substrate due to epitaxial nucleation and lattice mismatch. It equals to the energy difference between the films with and without the strain (Equation (3)).

$$\Delta E_s^i = E_i^{strained} - E_i. \quad (5.3)$$

In the case of α -FAPbI₃, we have confirmed in the experiments that both MAPbBr₃ substrate and α -FAPbI₃ film are (001) oriented. Our calculations also show that lattice constants of α -FAPbI₃ and MAPbBr₃ have a relatively large mismatch of 6%. Therefore, we can explicitly obtain $E_\alpha^{strained}$ in Equation (3) by calculating α -FAPbI₃ with 6% bi-axial compressive strain along ab -axes. The area-specific ΔE_s^α is calculated to be $1.2 \times 10^{-2} \text{ eV \AA}^{-2}$.

In the case of δ -FAPbI₃, the possible growth model is not straightforward. Therefore, we perform a search for the lattice plane of minimal lattice mismatch with MAPbBr₃ (001). The hexagonal (001) close-packed plane of δ -FAPbI₃ has dimensions of $a = b = 8.62 \text{ \AA}$ and $\gamma = 120^\circ$. Based on this plane, the termination we found that is most compatible with MAPbBr₃ (001) substrate has a large vector strain of 13.2% and 3.43° , and an area strain of 18.3%. This obviously exceeds the strain threshold for a coherent interface, which is usually below 10%.²¹⁸ We thus consider δ -FAPbI₃ forms incoherent interface with MAPbBr₃ (001). A film with the incoherent interface is not constrained by the substrate and the strain energy ΔE_s^δ is therefore 0.

To calculate the interfacial energy for α -FAPbI₃ (001)/MAPbBr₃ (001) ($\sigma^{\alpha||S}$), we build heterostructural models consisting of m layers of substrate and n layers of film. The two heterostructural models are shown in Fig. 5.1a. They represent two different terminations, namely FAI/PbBr₂ ($m = 5, n = 9$) and PbI₂/MABr ($m = 5, n = 11$). Note that only nine layers of film

material are shown in each structure for clarity.

The other two possible terminations for the α -FAPbI₃ (001)/MAPbBr₃ (001) interfaces are FAI/MABr and PbI₂/PbBr₂ (not shown here). Through initial analysis of bonding characteristics, we find that these terminations cannot form ionic bonds between the film and the substrate like the Pb-I (Pb-Br) bonds in FAI/PbBr₂ (PbI₂/MABr). ‘Physical contacts’ like FAI/MABr and PbI₂/PbBr₂²²⁰ at the interface are less stable than ‘chemical contacts’ like FAI/PbBr₂ and PbI₂/MABr. Therefore, we only focus on FAI/PbBr₂ and PbI₂/MABr in this investigation.

After the heterostructural models are confirmed, the interfacial energy can be calculated by subtracting the bulk energy of all components in the heterostructural model. Specifically, interfacial energy equations for these two heterostructural models are shown as Equations (4) and (5).

$$\sigma_{TERM1}^{\alpha||S} = \frac{1}{2A} (E_{HS1} - 2 \times E_{MAPbBr_3} - 4 \times E_{FAPbI_3}^{strain} - \mu_{Pb}^{MAPbBr_3} - 2 \times \mu_{Br}^{MAPbBr_3} - \mu_{FA}^{FAPbI_3} - \mu_I^{FAPbI_3}) \quad (5.4)$$

$$\sigma_{TERM2}^{\alpha||S} = \frac{1}{2A} (E_{HS2} - 2 \times E_{MAPbBr_3} - 5 \times E_{FAPbI_3}^{strain} - \mu_{MA}^{MAPbBr_3} - \mu_{Br}^{MAPbBr_3} - \mu_{Pb}^{FAPbI_3} - 2 \times \mu_I^{FAPbI_3}) \quad (5.5)$$

where E_{HS} is the total energy of the heterostructural model, E_{MAPbBr_3} is the total energy of the strain-free MAPbBr₃ lattice, $E_{FAPbI_3}^{strain}$ is the total energy of the strained α -FAPbI₃ lattice, and μ represents the chemical potentials of the corresponding atoms/molecules. Each of the heterostructural models contains two identical interfaces, and A is the interfacial area.

On the right-hand side, the trailing terms represent the bulk energy of each component in the heterostructure. For example, there are nine layers of α -FAPbI₃ in FAI/PbBr₂, which equals to four intact α -FAPbI₃ unit cells (each has two layers) plus one extra layer of FAI. The extra or un-stoichiometric components require the determination of their chemical potentials in the corresponding film or substrate material. Here we show in detail how we obtained chemical

potentials of un-stoichiometric α -FAPbI₃ components.

$$\Delta\mu_{FA} + \Delta\mu_{Pb} + 3\Delta\mu_I = \Delta H(FAPbI_3) = -5.78 \text{ eV} \quad (5.6)$$

$$\Delta\mu_{Pb} + 2\Delta\mu_I < \Delta H(PbI_2) = -2.02 \text{ eV} \quad (5.7)$$

$$\Delta\mu_{FA} + \Delta\mu_I < \Delta H(FAI) = -3.74 \text{ eV} \quad (5.8)$$

According to thermodynamic stability limits expressed in Equations (6) - (8), we plot the phase diagram for α -FAPbI₃ against the chemical potential change $\Delta\mu_I$ and $\Delta\mu_{Pb}$. Fig. 5.1b shows the phase diagram, and the long, narrow green region indicates the thermodynamic stability region for the synthesis of α -FAPbI₃. We select three representative points throughout the whole region for the following calculations: A ($\Delta\mu_I = -1.02 \text{ eV}$, $\Delta\mu_{Pb} = 0 \text{ eV}$), B ($\Delta\mu_I = -0.50 \text{ eV}$, $\Delta\mu_{Pb} = -1.03 \text{ eV}$), and C ($\Delta\mu_I = 0 \text{ eV}$, $\Delta\mu_{Pb} = -2.04 \text{ eV}$).

Similarly, we obtain the phase diagram for MAPbBr₃ substrate (not shown) and select one representative point P ($\Delta\mu_{Br} = -0.70 \text{ eV}$, $\Delta\mu_{Pb} = -1.47 \text{ eV}$) in the middle of the thermodynamically stable range. The values of point P are used as constants in Equations (4) and (5) for the un-stoichiometric MAPbBr₃ components.

We also added the stability limit for FAI/PbBr₂ and PbI₂/MABr in the phase diagram (Fig. 5.1b). As the red dashed line shows, FAI/PbBr₂ is more stable in the region below this limit, and it covers the whole stability range of α -FAPbI₃. Therefore, we only need to calculate the interfacial energy for FAI/PbBr₂, and the results are $2.86 \times 10^{-4} \text{ eV \AA}^{-2}$, $4.29 \times 10^{-4} \text{ eV \AA}^{-2}$, and $2.86 \times 10^{-4} \text{ eV \AA}^{-2}$ at A, B, and C points, respectively. Interestingly, the composition of interfacial terminations and their preferred chemical potential conditions agree with each other. For the δ -FAPbI₃/MAPbBr₃ (001) interface, the interfacial energy $\sigma^{\delta||S}$ is given as $6.242 \times 10^{-2} \text{ eV \AA}^{-2}$ (i.e., 1 Jm^{-2}), a typical value for incoherent interfaces.²¹⁸

Results for all energy terms in Equation (1) are summarized in Table 5.1. The calculated

Table 5.1: Thermodynamic terms relevant to epitaxial nucleation of α -FAPbI₃ and δ -FAPbI₃ on cubic MAPbBr₃ substrates. The bulk formation energy (ΔE_f), strain energy (ΔE_s), interfacial energy (σ), total energy change (ΔE), and the difference between the two phases ($\Delta E^{\alpha-\delta}$) are in eV \AA^{-2} . The value marked with * indicates that the interface between the substrate and the δ -FAPbI₃ is considered incoherent, and the interfacial energy term is set at $1 \text{ J m}^{-2} = 6.242 \times 10^{-2} \text{ eV \AA}^{-2}$.

	α -FAPbI ₃			δ -FAPbI ₃
	A	B	C	–
ΔE_f		-22.79×10^{-2}		-23.10×10^{-2}
ΔE_s		1.20×10^{-2}		0
σ	0.0286×10^{-2}	0.0429×10^{-2}	0.0286×10^{-2}	$6.242 \times 10^{-2*}$
ΔE	-21.5614×10^{-2}	-21.5471×10^{-2}	-21.5614×10^{-2}	-16.858×10^{-2}
$\Delta E^{\alpha-\delta}$	-4.7034×10^{-2}	-4.6891×10^{-2}	-4.7034×10^{-2}	–

total energy change of nucleating α -FAPbI₃ is around $-2.155 \times 10^{-1} \text{ eV \AA}^{-2}$ (regardless of chemical potential conditions), while the value for δ -FAPbI₃ is $-1.6858 \times 10^{-1} \text{ eV \AA}^{-2}$. Apparently, $\Delta E^{\alpha-\delta}$ has a negative value of around $-4.7 \times 10^{-2} \text{ eV \AA}^{-2}$ (i.e., -0.75 Jm^{-2}), which indicates epitaxial stabilization of α -FAPbI₃ with respect to δ -FAPbI₃ on MAPbBr₃ substrates. This result is comparable to prior successful prediction of epitaxial stabilization.

From Table 5.1, we can see that the bulk formation energy is the largest term but yields a small difference ($3.1 \times 10^{-3} \text{ eV \AA}^{-2}$) between α -FAPbI₃ and δ -FAPbI₃. The strain energy term is in favor of δ -FAPbI₃ by a large value of $1.2 \times 10^{-2} \text{ eV \AA}^{-2}$. The main contribution to $\Delta E^{\alpha-\delta}$ is from interfacial energy, which is above $6 \times 10^{-2} \text{ eV \AA}^{-2}$ and decides the overall energy preference. Notably, to accurately determine energetics using DFT calculations, we apply a large interfacial mismatch (strain = -6%) to calculate the strain energy term for α -FAPbI₃. However, the calculations represent an upper limit of strain's influence and guarantee a negative $\Delta E^{\alpha-\delta}$ in lower-strain circumstances. Strains below 6% would definitely yield a ΔE_s^α less than $1.2 \times 10^{-2} \text{ eV \AA}^{-2}$ and a more negative $\Delta E^{\alpha-\delta}$, which better ensures epitaxial stabilization of α -FAPbI₃. Another experimental variable is the substrate composition. We use MAPbBr₃ as the substrate in the heterostructural model to calculate the interfacial energies, but in experiments we also use

mixed-halide substrates with Cl composition up to $\text{MAPbCl}_{1.50}\text{Br}_{1.50}$. This will not change the conclusion of the discussions here because the substrate energy is excluded in the calculation of the interfacial energy, as shown in Equations (4) and (5).

Besides, the consideration of the stabilization mechanism is based on the system with both the α -FAPbI₃ and substrate lattices rather than just focusing on the α -FAPbI₃ lattice alone. Two different heterostructures (i.e., the α -FAPbI₃/substrate and the δ -FAPbI₃/substrate) are used to study the interfacial energy of nucleus crystallization during the epitaxial growth. The structure with lower interfacial energy will be more favorable during nucleus crystallization and, thus, more favorable to form. Calculation results show that the interfacial energy of the α -FAPbI₃/substrate ($0.0286 \times 10^{-2} \text{ eV } \text{\AA}^{-2}$) is much lower than that of the δ -FAPbI₃/substrate ($6.242 \times 10^{-2} \text{ eV } \text{\AA}^{-2}$). Therefore, the total energy of the α -FAPbI₃/substrate system is much smaller than that of the δ -FAPbI₃/substrate system because of the interfacial energy benefit, which stabilizes the epitaxial α -FAPbI₃ on the substrate. Additionally, the phase transition depends on not only the energy landscapes of both phases (phases before/after phase transition), but also the energy barrier between the two phases. This is where the epitaxial constraint from the substrate comes into play. In order to make the phase transition to happen, the α -FAPbI₃ need to break the ionic bonds with the substrate, which represents a very high energy barrier. Therefore, due to the synergistic effects of strain and epitaxial constraint, the α -FAPbI₃ is stable for long term as observed in this study. In summary, our calculations show reliable and robust validation of the epitaxial stabilization of α -FAPbI₃.

5.3.2 Strained α -FAPbI₃

First-principles calculations allow a better understanding of the structural deformation and prediction of any emerging new properties. Cubic α -FAPbI₃ unit cells are calculated with the N-N axis of the FA⁺ cation along (001), (101), and (111), respectively (left panel of Fig. 5.2a). These three low Miller index directions represent FA's typical orientations, and their calculated

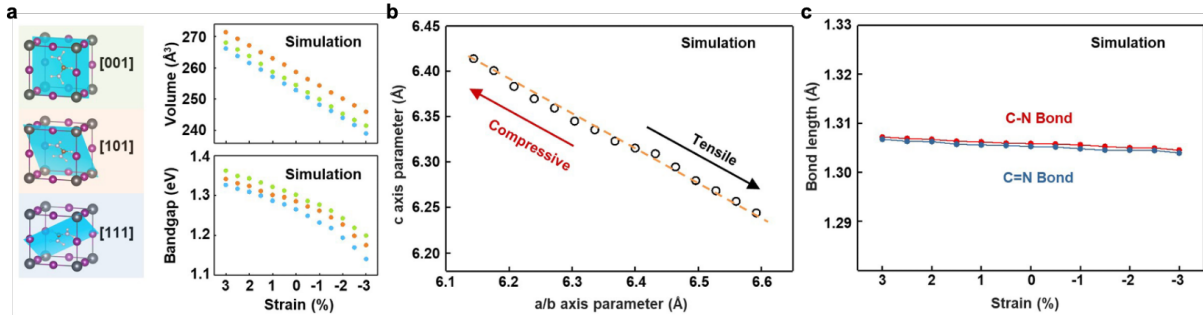


Figure 5.2: First-principles calculations of the strained α -FAPbI₃ unit cell under different strains. a, Evolution of lattice volume and bandgap as a function of strain for three α -FAPbI₃ lattices with different FA⁺ organic cation orientations. For the bandgap calculations, spin-orbit coupling is incorporated owing to the heavy element Pb, and the hybrid functionals within Heyd-Scuseria-Ernzerhof formalism with 25% Hartree-Fock exchange are employed. b, The *c* axis length of the unit cell when biaxially straining the *a/b* axes. The slope of the fitted line shows a Poisson's ratio of about 0.3. c, C-N and C=N bond lengths at different strain levels. Calculation results show that the deformation of the FA⁺ skeleton is very small under the applied biaxial strain.

total energies could reveal potential orientation preferences. As the first step, we optimized the cubic lattice parameter *a* for each orientation to obtain the lowest total energy. Our calculations show $a = 6.35 \text{ \AA}$ for the FA along (001), $a = 6.40 \text{ \AA}$ for the FA along (101), and $a = 6.37 \text{ \AA}$ for the FA along (111). The optimized structure with the FA along (101) has the lowest total energy of -52.73 eV, and the optimized structure with the FA along (001) shows the highest total energy of -52.68 eV. The total energy difference between these two structures is within 50 meV, and thus the structural model with FA along (101) direction was used in our calculations.

Then we applied bi-axial strains in the *ab*-plane of the optimized structure for each orientation. The range is from 3% tensile strain to -3% compressive strain. The strained cells keep their original FA orientation after optimization along the *z*-direction. For bandgap calculations, spin-orbit coupling (SOC) was incorporated due to the heavy element Pb, and hybrid functionals within Heyd-Scuseria-Ernzerhof (HSE) formalism with 25% Hartree-Fock (HF) exchange were employed. The calculated bandgap energy (lower right of Fig. 5.2a) and cell volume (upper right of Fig. 5.2a) are displayed as a function of the bi-axial strain. The cell volume decreases as the strain changes from tensile to compressive for each FA orientation. This is a result of

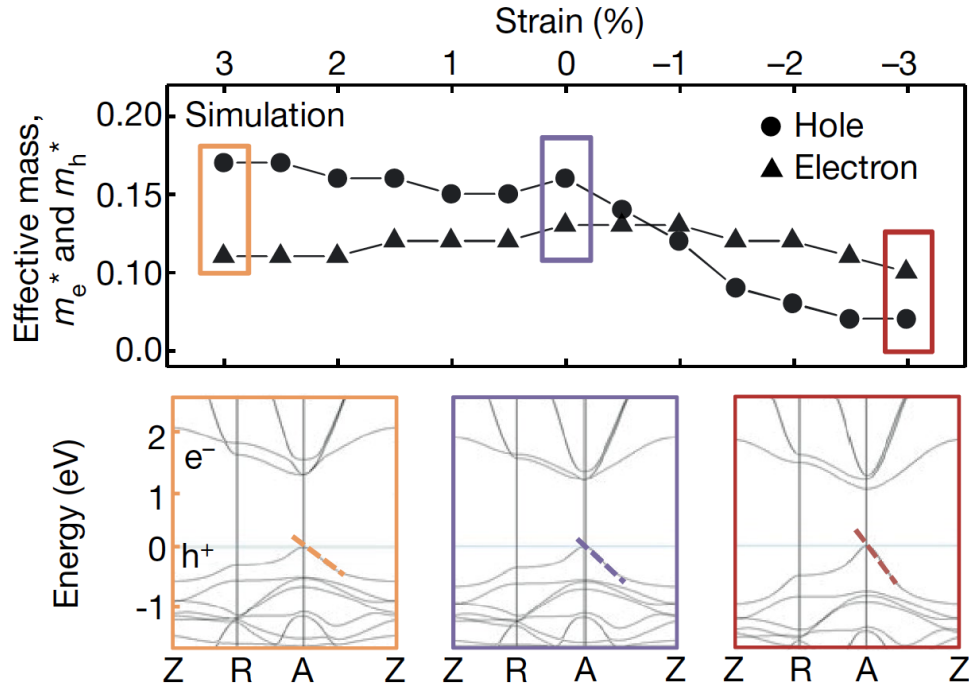


Figure 5.3: Calculated effective masses of the carriers at different strains, and electronic band structures under three strain levels (3%, 0%, and -3%). The electron effective mass (m_e^*) remains relatively stable with the change in strain, while the hole effective mass (m_h^*) decreases with increasing compressive strain. The dashed lines represent the dispersivity of the valence band; a less dispersive valence band structure indicates a smaller hole effective mass. The Z, R and A points are high-symmetry points in the first Brillouin zone of the tetragonal lattice. Bottom panels with colored borders represent three typical examples with different strains.

the decreased a and b and slightly increased c . The bandgap decreases as well when the strain changes from tensile to compressive for each FA orientation.

Fig. 5.2b shows the out-of-plane lattice deformation with different in-plane strain levels. A Poisson's ratio of around 0.3 can be calculated, consistent with the experimental value by reciprocal space mapping. Meanwhile, C-N and C=N bond lengths in FA⁺ cation with different strain levels (Fig. 5.2c) show no obvious changes with the strain, indicating a weak interaction between the FA⁺ cation and the inorganic Pb-I framework.

To investigate the effect of strain on carrier dynamics in α -FAPbI₃, we analyzed the variation of charged carrier mobility via predicting effective masses of charged carriers from first-principles calculations. In the calculations, the mean free time of carriers was assumed to be

a constant, and the reversely proportional relationship between the effective mass and charged carrier mobility was used. Carrier effective masses are determined by the curvature of the highest energy at the VBM for holes and lowest energy at the CBM for electrons in the k space. Figure 5.3 shows the calculated electron and hole effective masses of α -FAPbI₃ under different strain levels. Electronic band structures of α -FAPbI₃ under 3%, 0%, and -3% are also shown in the lower panels of Fig. 5.3. Results indicate that the hole effective mass m_h^* decreases when strain goes from tensile to compressive, while the electron effective mass m_e^* barely changes with the strain. The trend of m_h^* can be revealed from the curvature of the highest energy point of the VBM, which gets less dispersive with increasing compressive strain. This is due to the fact that the VBM that determines m_h^* mainly consists of Pb 6s and I 5p orbitals. Under tensile strain, the distance between Pb and I atoms increase and therefore the Pb-I bond interaction is weakened, thus leading to the increase of effective mass. In contrast, the hole mobility will increase under compressive strain due to the enhanced Pb-I bond interaction and the decreased effective mass. However, the CBM that determines the electron effective mass mainly consist of Pb p orbitals is less sensitive to the deformation of Pb-I bonds, which is why m_e^* barely changes with applied strain.²²¹

5.4 Conclusion

In summary, we studied epitaxial growth and effects of strains on the halide perovskite α -FAPbI₃. Our calculations demonstrated the epitaxial stabilization by calculating detailed thermodynamic terms in the epitaxial nucleation process. Among the thermodynamic terms, interfacial energy dominates the energy advantage of α -FAPbI₃ during epitaxial nucleation. We also show that strains control the crystal structure, the bandgap, and the hole effective mass. The strained epitaxial growth is thus demonstrated to enhance the stability and optoelectronic properties of α -FAPbI₃. This work is expected to inspire stabilization of other metastable

perovskites with appropriate optoelectronic applications.

5.5 Acknowledgements

Chapter 5, in part, is a reprint of the material “Strain Engineering and Epitaxial Stabilization of Halide Perovskites” as it appears in Nature. Yimu Chen, Yusheng Lei, Yuheng Li, Yugang Yu, Jinze Cai, Ming-Hui Chiu, Rahul Rao, Yue Gu, Chunfeng Wang, Woojin Choi, Hongjie Hu, Chonghe Wang, Yang Li, Jiawei Song, Jingxin Zhang, Baiyan Qi, Muyang Lin, Zhuorui Zhang, Ahmad E. Islam, Benji Maruyama, Shadi Dayeh, Lain-Jong Li, Kesong Yang, Yu-Hwa Lo, Sheng Xu, 577, 209-215, 2020. The dissertation author was a co-author of this paper.

Chapter 6

Conclusion and Outlook

6.1 Outlook on High-Throughput Design of Halide Perovskites and Beyond for Optoelectronics

As discussed in Chapters 1-3, many promising candidates have been predicted from high-throughput computational materials design. However, additional efforts are still needed to examine their synthesizability, validate their properties, and realize optoelectronic devices based on these materials. In addition, next-step computational screening efforts could be done to explore novel materials structures and to further improve the efficiency of HT materials design, for example, using the emerging machine learning (ML) approach. On the basis of these considerations, we highlight possible future research directions as below:

i) Stable and lead-free halide semiconductors that exhibit similar exceptional properties as lead halide perovskites could revolutionize many fields including the solar cell industry. Table 1.1-1.4 summarize promising alternative materials to lead halide perovskites predicted from HT computational design, which can be classified into four categories. Generally, these materials need more detailed characterization and specific development for their applications in optoelectronic devices through additional experimental efforts, along with more accurate computational/theoretical

studies. The IVA-element based single perovskites have been enumerated by early HT studies, and a large number of experiments have demonstrated their advantages and disadvantages (Table 1.1). Despite the elimination of toxicity in these perovskites, oxidation of divalent Ge or Sn ions poses ambient stability issues. For other element-based single perovskites, most search efforts considered various B-site cations solely with the perovskite structure and did not compare the candidates' stability or synthesizability with their competing phases in other possible structures. This leads to the fact that most predicted compositions crystallize in non-perovskite structures, and that the candidates do not have much experimental validation in Table 1.2. For double perovskites, because of the large chemical search space induced by their quaternary composition, there are much more prediction results than the other three categories of materials, and several predicted compounds have been successfully synthesized (Table 1.3). However, some predicted compounds like A_2GeSnX_6 double perovskites are less inspiring because they are simple combinations of IVA element-based single perovskites. In addition, some double perovskite predictions also have the problem of stability overestimation. One example is the predicted family of $A_2In(I)M(III)X_6$ ($M = Bi, Sb$) double perovskites. Theoretical and experimental studies proved that these perovskites are intrinsically unstable with respect to oxidation into In(III)-based compounds, and that the HT predictions neglected redox reactions as decomposition pathways.⁷⁴ Another example is the HT prediction of Cu(I)-based double perovskites. Indeed, Cu(I) atoms tend to form $[CuX_4]$ tetrahedra instead of $[CuX_6]$ octahedra as in perovskite structures, as proved by theoretical and experimental efforts.⁷⁵ Notably, there is a special class of materials called mixed-valence perovskites (e.g. In(I)-In(III) and Au(I)-Au(III) perovskites). These perovskites have ternary compositions of single perovskites but the +1/+3 valence states of metal ions in double perovskites. Although predicted by HT studies, In(I)-In(III) perovskites have the same chemical stability problem of In(I) oxidation as in In(I)-based double perovskites. A later computational study also showed that they have indirect and too small bandgaps, and that local mixed-valence In(I)-In(III) configuration in In(I)-Bi(III) double perovskites induces deep defect states.²²² Similarly, another study showed

that the predicted Au(I)-Au(III) perovskites have two-dimensional electronic properties including highly anisotropic band structures and flat conduction band and valence band at the band edges.²²³

ii) As large-scale materials data have been generated from the HT studies, screening of candidates for other optoelectronic applications, including transistors, lasers, and wide-bandgap top-cell materials in perovskite-silicon tandem solar cells, can be achieved with reduced computational cost. These materials data also enable the training of ML algorithms to reveal the undiscovered trends and materials design principles for halide optoelectronics.

iii) HT computational design based on perovskite-derived structures is a promising direction and have started lately. These structures could show intrinsically higher thermodynamic stability than perovskite structures. Besides the single-perovskite derivatives reviewed, there are still many versatile prototype structures such as double perovskites and low-dimensional perovskites. The prior materials design in these perovskite-derived structures have been proven successful from the experimental synthesis of some candidate materials (Table 1.4). Also, an appropriate application of ML approach in these novel structures could further speed up the materials discovery process. However, it is noted that most ML models in the reviewed topic deal with perovskites only, and features that effectively account for different structures are scarce, and the inclusion of various prototype structures in the ML approach could be challenging but also interesting.

iv) Although HT computational design is a powerful tool to discover novel materials at low cost, unreasonable process design (e.g. calculations of redundant materials that can be pre-excluded by basic chemical rules) may result in unnecessary cost of computation resources and ineffective prediction results. As more and more HT materials screening studies become available for perovskite-related optoelectronics, some general protocols that regulate the methodologies, levels of theory, and the examination of materials stability should be considered by the HT computation community. These protocols are important for the robustness and reliability of the screening results and more informative for guiding experimental studies. For example, as an

essential property in computational prediction, thermodynamic stability should be rigorously analyzed by calculating decomposition enthalpy with respect to all possible pathways or by analyzing energy above the convex hull with phase diagrams. The ongoing development of automation toolkit and standard materials libraries will also greatly help apply such protocols in the HT studies.

6.2 Conclusion

Organic-inorganic hybrid lead halide perovskites hold great promise as next-generation solar-cell and light-emitting materials. However, they are faced with two critical issues hindering their large-scale commercialization, namely low stability and the toxicity of lead. Besides, their high efficiencies and working mechanisms require deep theoretical understanding. In this dissertation, we focus on design of stable and non-toxic halide perovskite alternatives to solve the two issues, and we also investigate and optimize their materials properties for applications in solar cells and light-emitting diodes.

In the first project, we have demonstrated a unique high-throughput approach to the discovery of hybrid halide compounds related to perovskites for optoelectronic applications. The design process has screened a comprehensive quantum materials repository containing 4507 hybrid compounds using a series of electronic and energetic descriptors including difference of formation enthalpy, decomposition enthalpy, bandgap, charge carrier effective masses, and exciton binding energy to select promising candidates for optoelectronic applications. A total number of 23 candidates for light-emitting diodes and 13 candidates for solar energy conversion were selected. These candidates adopt five prototype structures, including tetragonal structure consisting of layers of corner sharing $B^{II}X_6$ (tI14), hexagonal structure consisting of corrugated layers of corner-sharing $B^{III}X_6$ (hP14), hexagonal structure consisting of dimers of face-sharing $B^{III}X_6$ (hP28), tetragonal structure consisting of isolated $B^{IV}X_6$ (tI18), and cubic structure

consisting of isolated $B^{IV}X_6$ (cF36). The tI14 candidates contain $B^{II}=\text{Ge, Sn}$; the hP14 and hP28 candidates contain $B^{III}=\text{Ga, In, Sb, Bi}$; and the tI18 and cF36 candidates contain $B^{IV}=\text{Zr, Te, Sn, and Hf}$. It is important to note that this approach is transformative to the discovery of other types of functional materials.

In the second project, we continue the screening process by using high-throughput first-principles electronic structure calculations. We have systemically studied the stability diagrams, defect tolerance, and absorption coefficients for the screened lead-free 29 candidate hybrid semiconductors for optoelectronic applications. The calculated stability diagram outlines the thermodynamically stable range for the equilibrium growth of the predicted compound with different chemical potentials. The defect tolerance was evaluated from the calculated defect formation energies and transition levels. Out of the selected 29 compounds, 15 candidates show high defect tolerance. The absorption coefficients were calculated from the dielectric functions. These computational studies provide detailed guidance on the further experimental synthesis and characterization of these lead-free hybrid compounds, with a potential to facilitate the development of novel optoelectronic devices.

The first two projects focus on materials design of lead halide perovskite alternatives to intrinsically solve the stability and toxicity issues. In the last two projects, we focus on individual materials to understand their specific structural, energetic, and electronic properties, and propose methods to optimize these properties for improved performance in optoelectronic applications.

In the third project, ferroelectric dipole ordering of MA cations in MAPbI_3 were studied from first-principles calculations. First, we investigated two types of MA cation rotations, including in-phase and out-of-phase rotations, and calculated their energy barriers. Second, the energetic advantage of the FE state relative to the AFE states was determined. Last, we explored means to further enhance the FE dipole ordering. We have found that The larger the cell aspect ratio c/a is, the less likely MA flipping rotation becomes. Moreover, the out-of-phase flipping rotation of MA cations in tetragonal MAPbI_3 tends to form FE dipole ordering. The FE

dipole ordering state is energetically more favorable than the AFE states, with a small energetic advantage of 36 meV. Polarization contributed by FE dipole ordering in tetragonal MAPbI₃ was calculated to be 3.15 $\mu\text{C}/\text{cm}^2$. Based on change of c/a , compressive strain and substitutional doping with smaller anions can both enhance the energetic advantage of the FE dipole ordering state in tetragonal MAPbI₃. This work could provide some key insights into design principles of high-efficiency solar cells based on hybrid halide perovskites.

In the fourth project, we studied epitaxial growth and effects of strains on halide perovskites α -FAPbI₃. Our calculations demonstrated the epitaxial stabilization by calculating detailed thermodynamic terms in the epitaxial nucleation process. Among the thermodynamic terms, interfacial energy dominates the energy advantage of α -FAPbI₃ during epitaxial nucleation. We also show that strains control the crystal structure, the bandgap, and the hole effective mass. The strained epitaxial growth is thus demonstrated to enhance the stability and optoelectronic properties of α -FAPbI₃.

In summary, our first-principles study of hybrid halide perovskites and beyond has led us to discovery of novel optoelectronic materials, as well as fundamental understanding and optimization of the structural, energetic, and electronic properties of halide perovskites. Ultimately, our research is motivated by an explicit goal of solving challenges and propelling real-world applications of halide perovskites and beyond in optoelectronics. We expect that the discovered materials will facilitate cheap and high-efficiency next-generation solar cells and light-emitting diodes, and that the understanding and optimization strategies will provide theoretical insights for improving the material performance in the optoelectronic applications.

6.3 Acknowledgements

Chapter 6, in part, is a reprint of the material “High-Throughput Computational Design of Halide Perovskites and Beyond for Optoelectronics” as it appears in WIREs Computational

Molecular Science. Yuheng Li, Kesong Yang, e1500, 2020. The dissertation author was the primary investigator and author of this paper.

Appendix A

Prototype Structures, Anisotropic Effective Masses, and AIMD results for HT Materials Design

Table A.1: Calculated properties for the reference compound MASnBr_3 (cP5) using different functionals: lattice parameters (in \AA), electron (hole) effective masses m_e^* (m_h^*) near the CBM (VBM), reduced effective mass (μ), and decomposition enthalpy (ΔH_d , in eV/f.u.). The experimentally measured lattice parameters are $a = 5.837 \text{ \AA}$ and $c = 5.853 \text{ \AA}$.

Functional	Lattice Parameters			m_e^*	m_h^*	μ	ΔH_d
	a	b	c				
PBE	5.9538	5.9144	6.0039	0.31	0.18	0.11	0.26
vdW.D3	5.8446	5.8208	5.8533	0.32	0.12	0.09	0.22
optB86b	5.8289	5.8059	5.8473	0.32	0.14	0.10	0.21

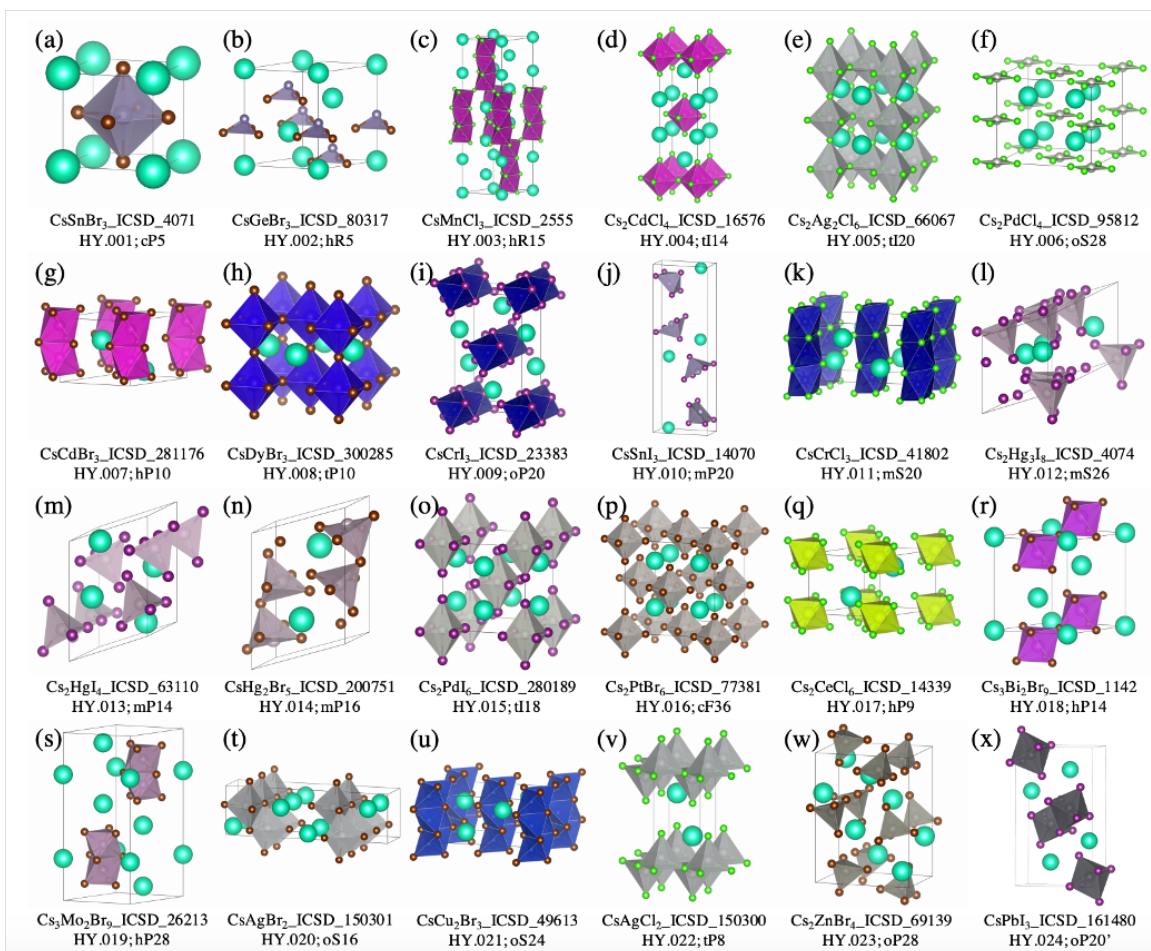
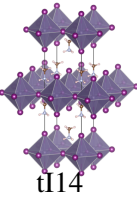
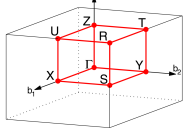
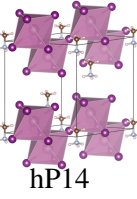
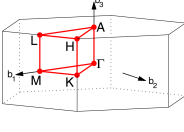
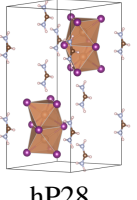
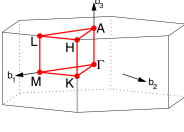
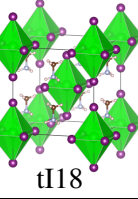
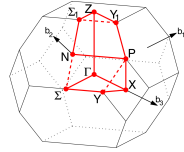


Figure A.1: Structures of the 24 perovskite-derived inorganic metal halide compounds ($\text{Cs}_x\text{B}_y\text{X}_z$) used as structural prototypes (HY.001-HY.024) to build the hybrid metal halide compound repository. The conventional-cell structures are shown in polyhedral style from the standard orientation of crystal shape using VESTA. ICSD number and Pearson symbol of each inorganic compound are given.

Table A.2: Calculated electron and hole effective masses along major directions for the anisotropic tI14, hP14, hP28, and tI18 candidates. † denotes effective masses calculated with SOC.

Prototype Structure	Brillouin Zone	Candidates	$\Gamma - Z$		$\Gamma - X$	
			m_e^*	m_h^*	m_e^*	m_h^*
 tI14		(MA) ₂ GeBr ₄	0.89	2.04	0.11	0.23
		(MA) ₂ GeI ₄	0.80	38.73	0.10	0.23
		(MA) ₂ SnCl ₄	3.37	3.20	0.14	0.23
		(MA) ₂ SnBr ₄	4.36	2.29	0.10	0.16
		(MA) ₂ SnI ₄	4.12	8.38	0.09	0.15
		(FA) ₂ SnBr ₄	2.41	1.76	0.12	0.18
		(AD) ₂ GeI ₄	0.82	1.72	0.10	0.56
		(AD) ₂ SnBr ₄	1.07	1.89	0.13	0.26
		(AD) ₂ SnI ₄	1.17	1.19	0.10	0.22
		 hP14		(MA) ₃ In ₂ I ₉	0.46	12.74
(MA) ₃ Sb ₂ Br ₉	0.33			0.41	0.52	2.66
(MA) ₃ Sb ₂ I ₉	0.38			0.31	0.33	0.31
(MA) ₃ Bi ₂ I ₉	0.41†			1.21†	0.63†	0.82†
(FA) ₃ Ga ₂ I ₉	2.37			50.87	0.76	1.17
(FA) ₃ In ₂ Br ₉	0.57			6.17	2.02	0.23
(FA) ₃ In ₂ I ₉	0.52			9.03	1.68	0.57
(FA) ₃ Bi ₂ I ₉	1.06†			10.46†	0.26†	0.75†
(AD) ₃ Sb ₂ Br ₉	0.50			0.43	0.65	1.65
(AD) ₃ Sb ₂ I ₉	0.36			0.31	0.40	2.94
(AD) ₃ Bi ₂ I ₉	0.51			0.66	0.46	1.26
 hP28				(FA) ₃ Sb ₂ I ₉	2.00	6.96
		(AD) ₃ In ₂ I ₉	0.92	1.63	1.27	1.40
 tI18		(MA) ₂ ZrI ₆	0.80	1.59	8.46	0.98
		(AD) ₂ HfI ₆	3.20†	0.80†	2.54†	1.73†
		(AD) ₂ SnBr ₆	0.51	1.24	0.52	1.76
		(AD) ₂ TeBr ₆	1.69	2.17	2.15	1.03

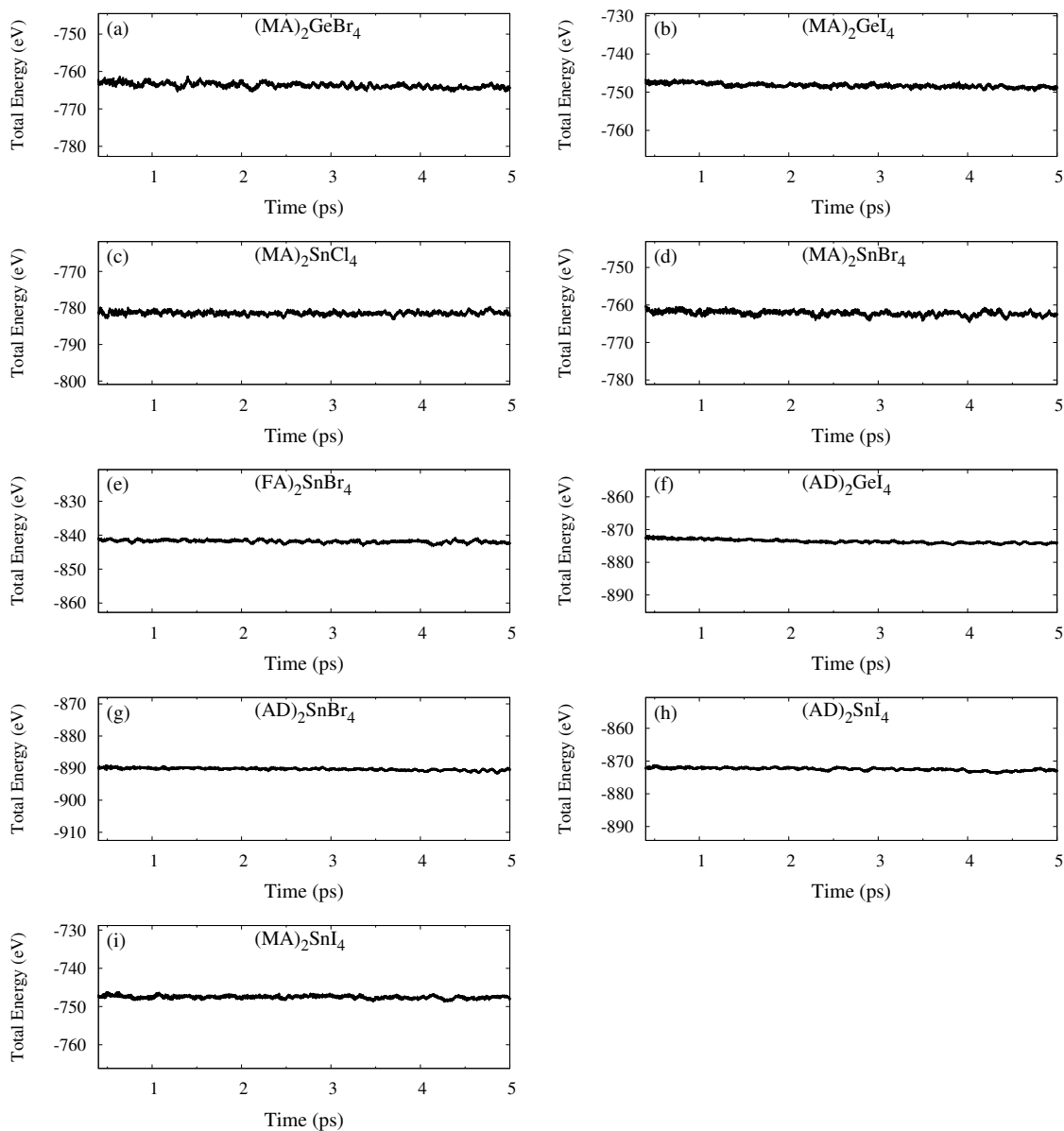


Figure A.2: Total energy during 5ps *ab-initio* molecular dynamics (AIMD) simulations at 300K for all the screened tI14 compounds. In this and subsequent figures, the Pearson symbols of analogue inorganic compounds including tI14, hP14, tI18, cF36, and hP28 are used to distinguish the prototypes of the screened hybrid inorganic-organic materials.

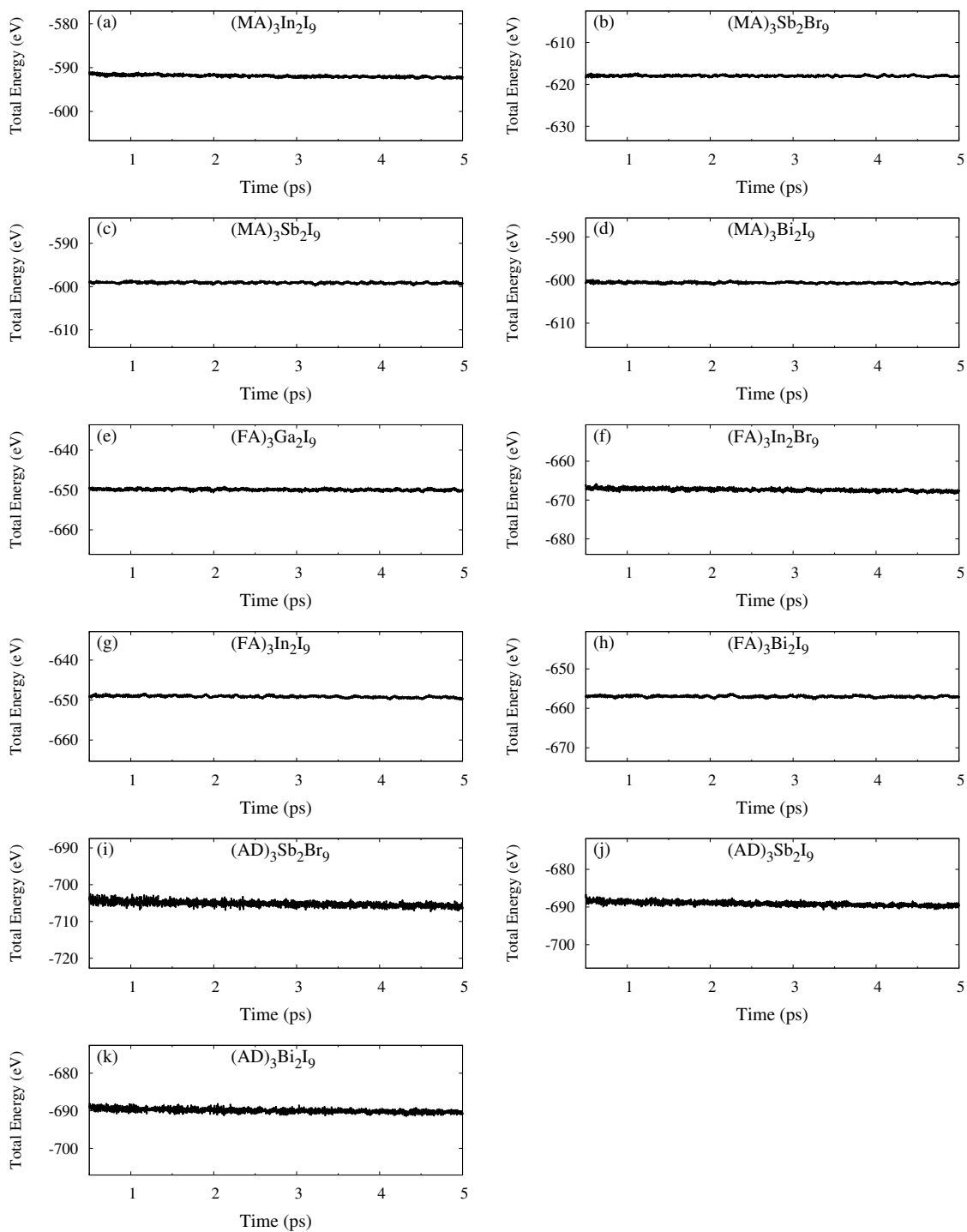


Figure A.3: Total energy during 5ps *ab-initio* molecular dynamics (AIMD) simulations at 300K for all the screened hP14 compounds.

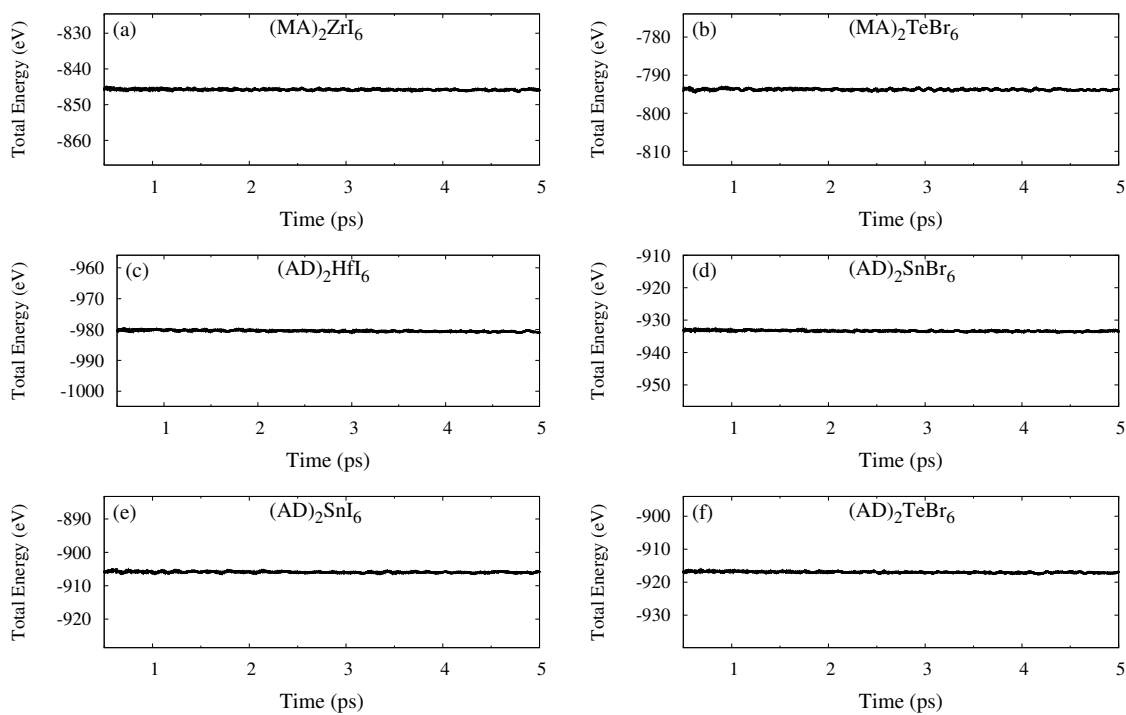


Figure A.4: Total energy during 5ps *ab-initio* molecular dynamics (AIMD) simulations at 300K for all the screened tI18 compounds.

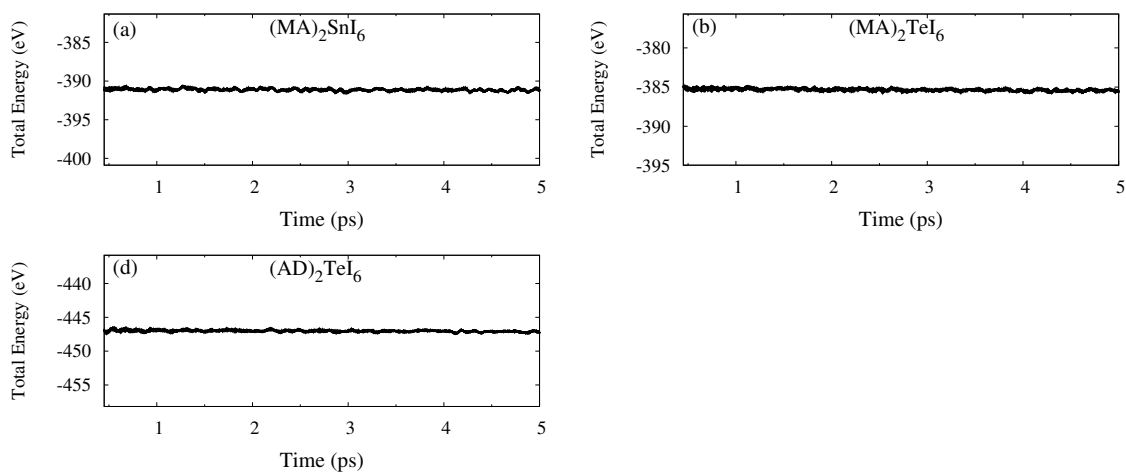


Figure A.5: Total energy during 5ps *ab-initio* molecular dynamics (AIMD) simulations at 300K for all the screened cF36 compounds.

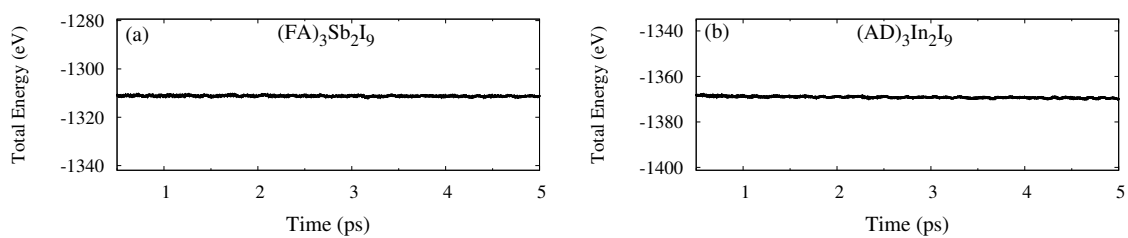


Figure A.6: Total energy during 5ps *ab-initio* molecular dynamics (AIMD) simulations at 300K for all the screened hP28 compounds.

Appendix B

Phase Diagrams, Defect Tolerance, and Absorption Coefficients for the 29 Perovskite Derivatives

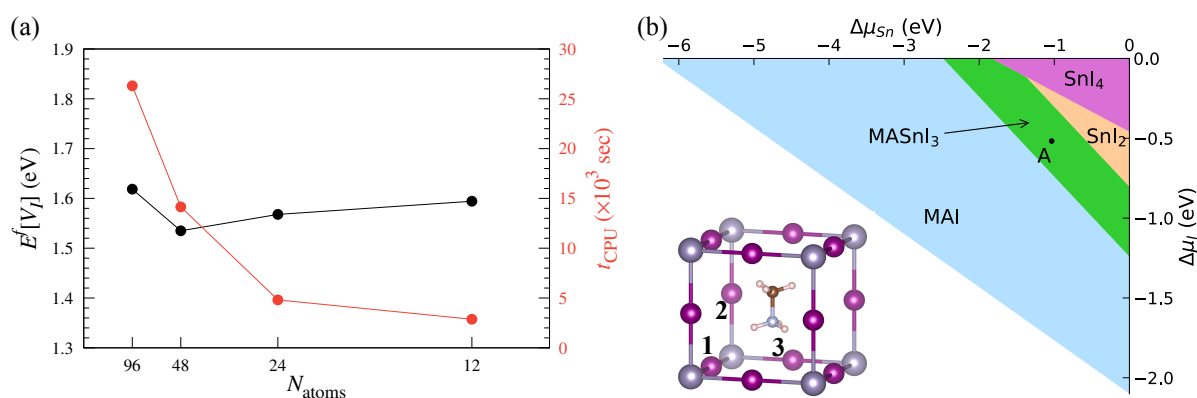


Figure B.1: (a) Defect formation energies of iodine vacancy ($E^f[V_I]$) in $MASnI_3$ perovskite and calculation CPU time (t_{CPU}) as functions of the inverse number of atoms (N_{atoms}). (b) Crystal structure of the cubic unit cell and the stability diagram of $MASnI_3$. There are three inequivalent iodine sites in the unit cell (noted 1, 2, and 3). Chemical potential at A ($\Delta\mu_I = -0.518$ eV, $\Delta\mu_{Sb} = -1.035$ eV) is used in formation energy calculations.

Table B.1: Cell sizes for defect calculations of exemplary compounds in the five prototype structures.

Compound (structure)	MA ₂ SnI ₄ (tI14)	MA ₃ Bi ₂ I ₉ (hP14)	FA ₃ Sb ₂ I ₉ (hP28)	MA ₂ ZrI ₆ (tI18)	MA ₂ TeI ₆ (cF36)
a (Å)	6.12	8.35	8.02	8.18	11.67
b (Å)	6.11	16.69	8.32	8.19	11.51
c (Å)	20.00	11.00	23.18	12.37	12.58
N_{atoms}	42	70	70	46	92

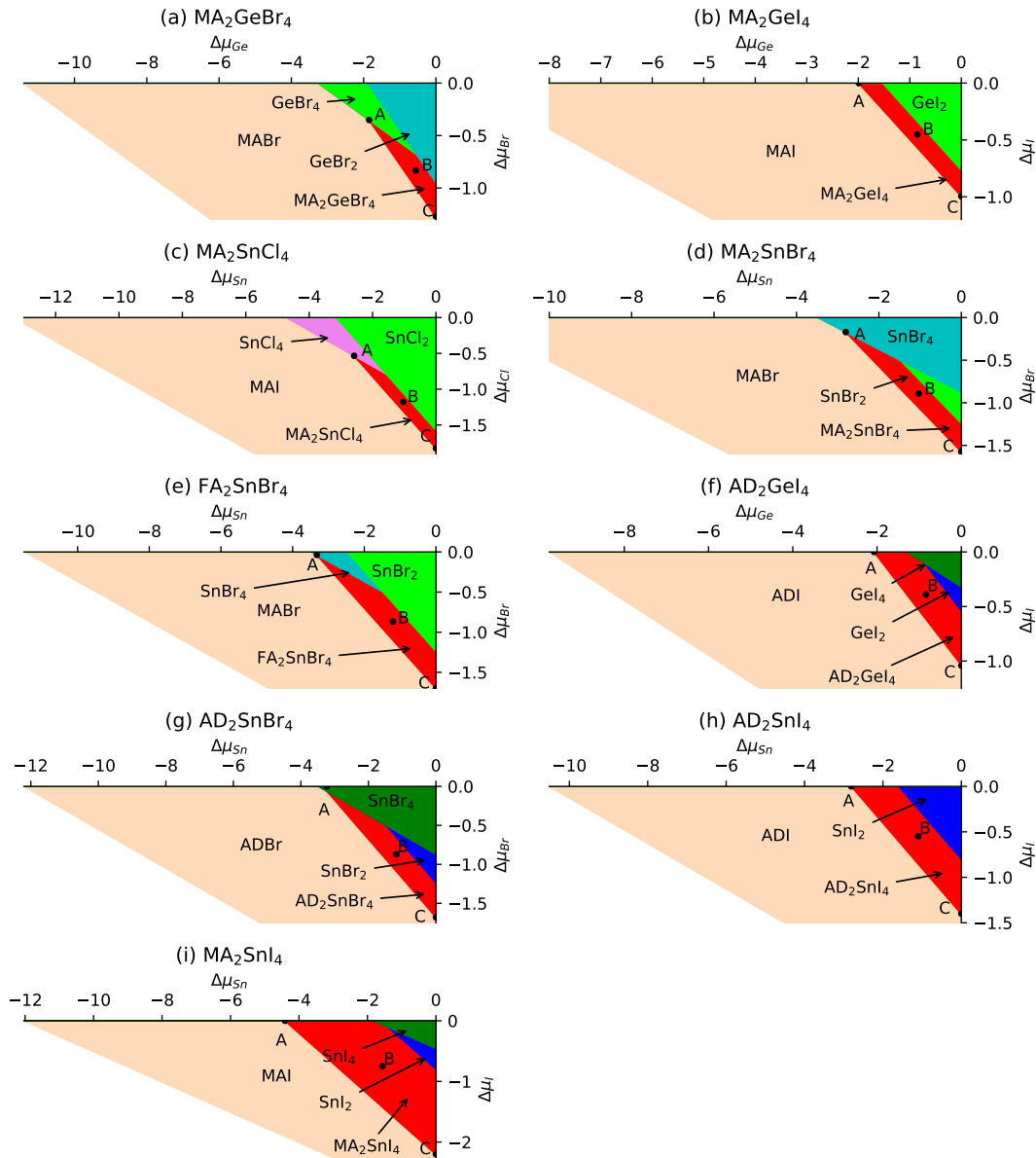


Figure B.2: Calculated stability diagram for tI14 compounds. In this and subsequent stability diagram figures, the region in red depicts the thermodynamically stable range for equilibrium growth of the compound with respect to the chemical potential of inorganic cations and halide anions. Outside this region, the compound decomposes into various type of decomposers. The three representative points A, B, and C are selected to calculate the defect formation energies. The Pearson symbols of analogue inorganic compounds including tI14, hP14, tI18, cF36, and hP28 are used to distinguish the prototypes of the screened hybrid inorganic-organic materials.

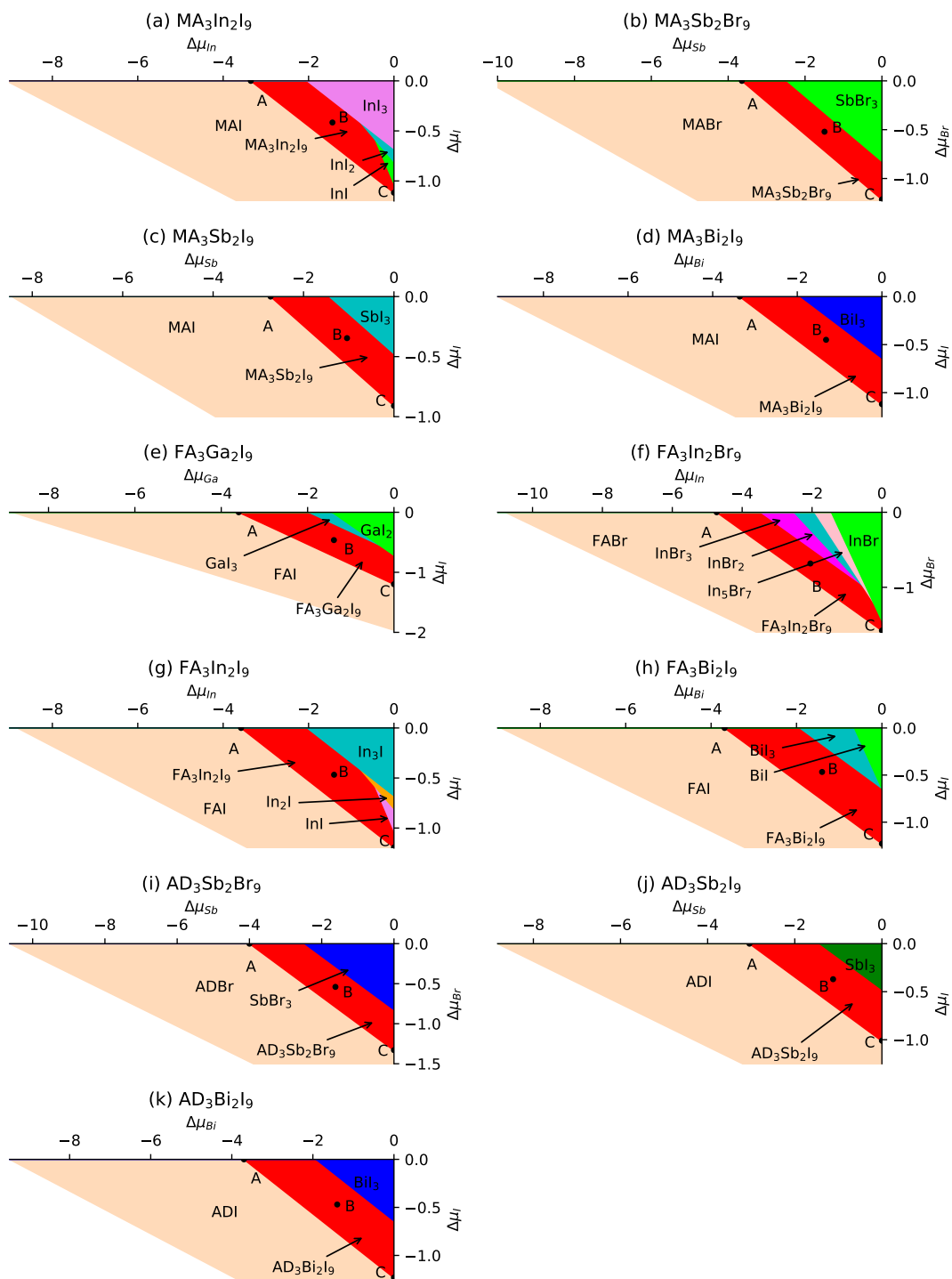


Figure B.3: Calculated stability diagram of hP14 compounds.

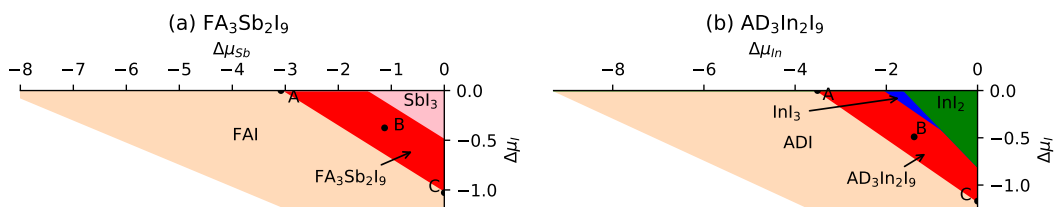


Figure B.4: Calculated stability diagram of hp28 compounds.

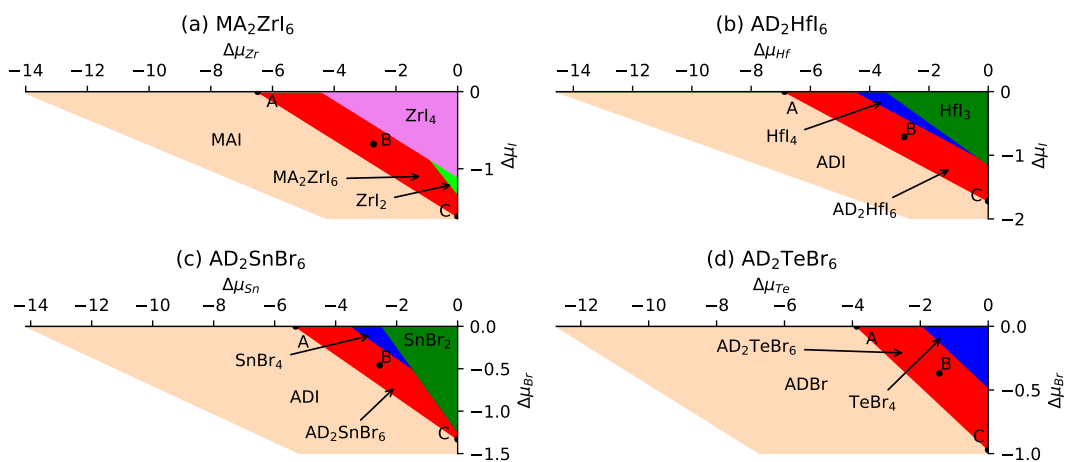


Figure B.5: Calculated stability diagram of tl18 compounds.

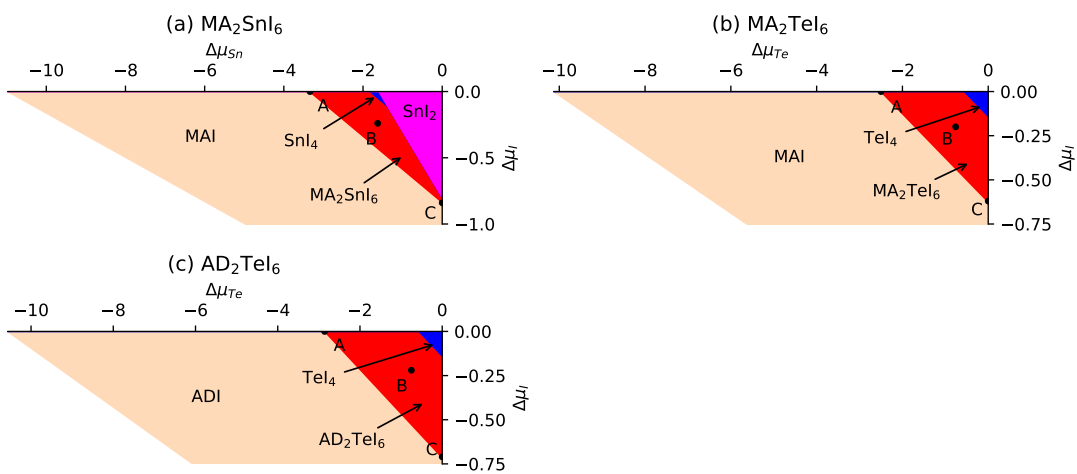


Figure B.6: Calculated stability diagram of cf36 compounds.

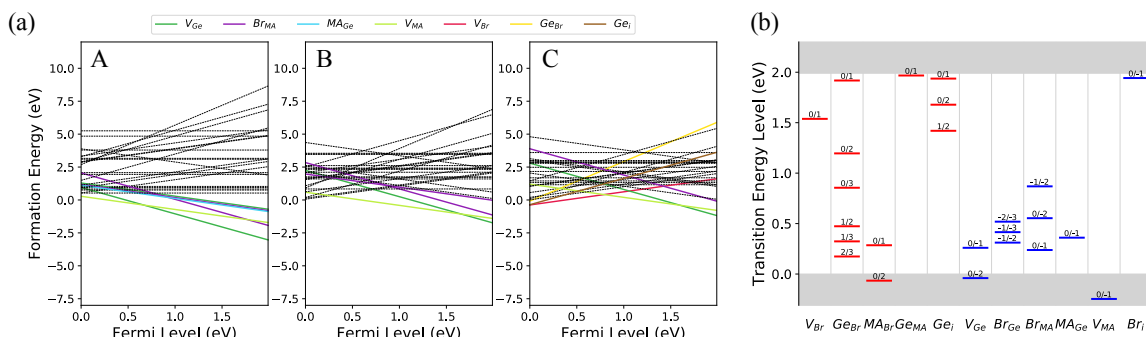


Figure B.7: Calculated (a) defect formation energy and (b) transition energy levels for MA₂GeBr₄ (tI14). In this and subsequent figures, the formation energies of intrinsic point defects are plotted at chemical potentials A, B, and C, respectively. Defects with formation energies above 0 eV throughout the band gap range are shown as dashed lines. The transition energy levels of intrinsic donors and acceptors are plotted in red and blue, respectively.

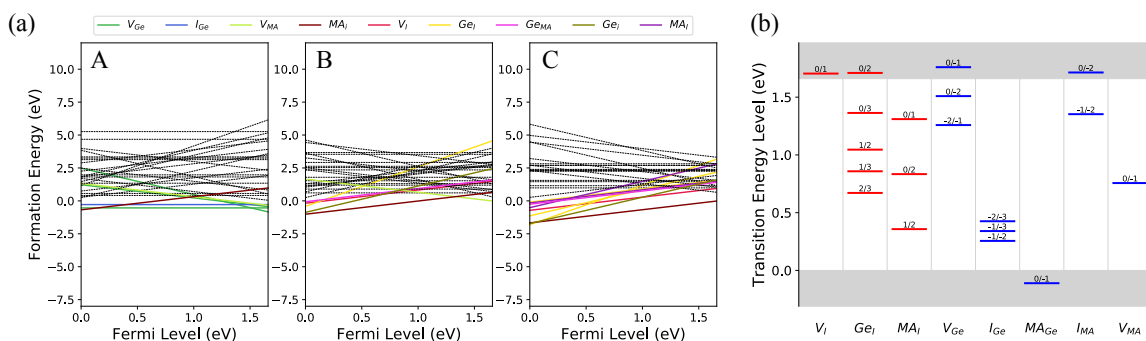


Figure B.8: Calculated (a) defect formation energy and (b) transition energy levels for MA₂GeI₄ (tI14).

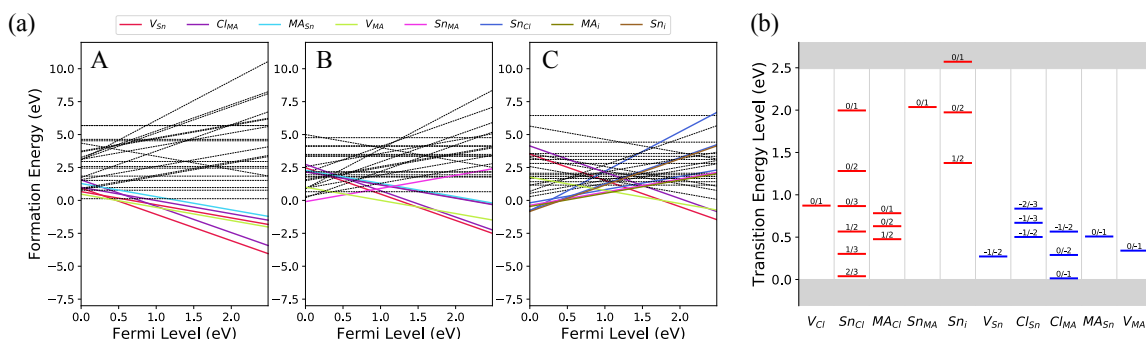


Figure B.9: Calculated (a) defect formation energy and (b) transition energy levels for MA₂SnCl₄ (tI14).

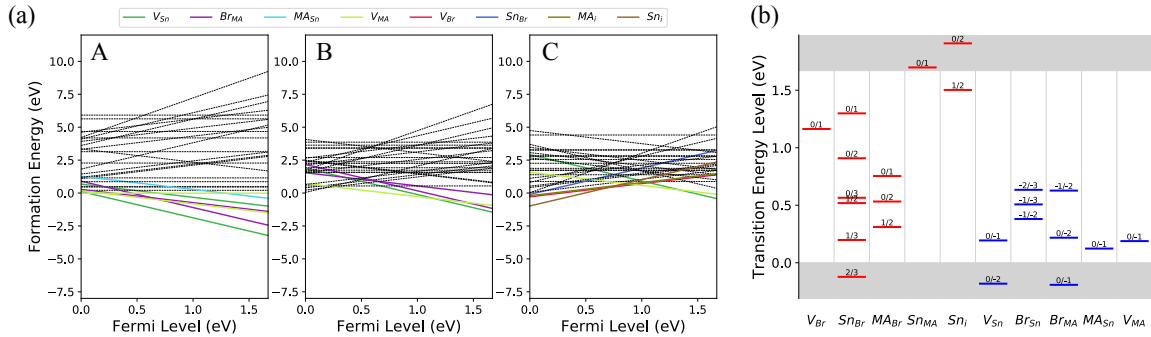


Figure B.10: Calculated (a) defect formation energy and (b) transition energy levels for MA₂SnBr₄ (tI14).

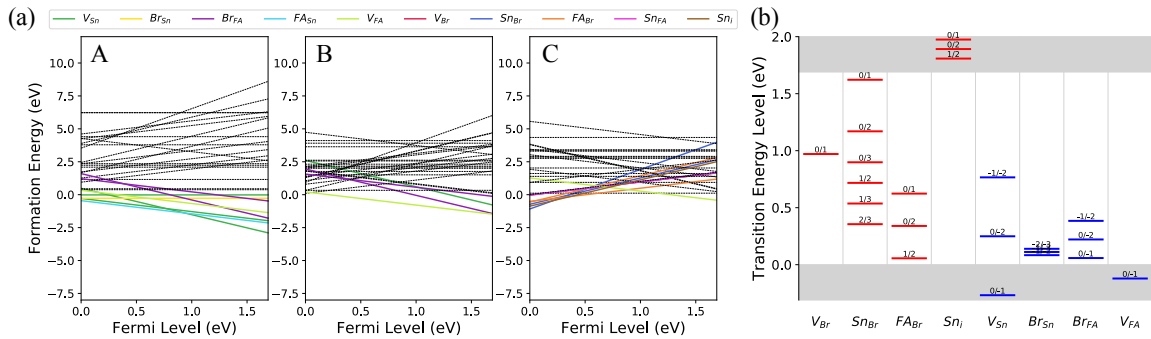


Figure B.11: Calculated (a) defect formation energy and (b) transition energy levels for FA₂SnBr₄ (tI14).

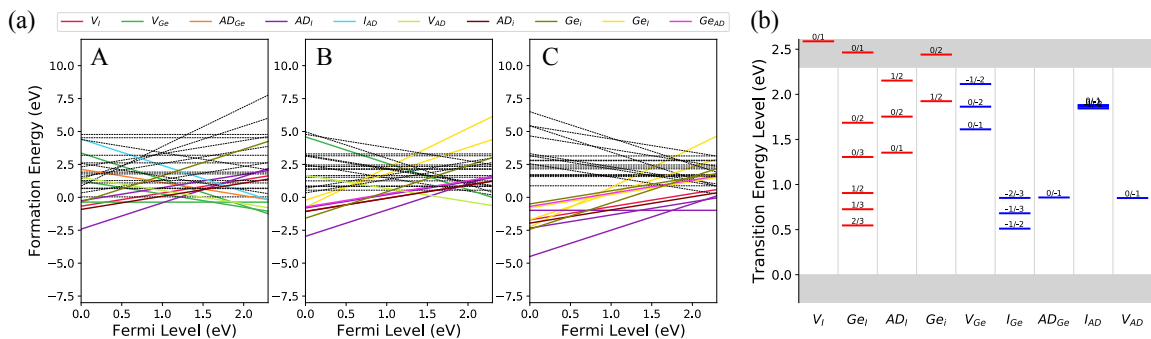


Figure B.12: Calculated (a) defect formation energy and (b) transition energy levels for AD₂GeI₄ (tI14).

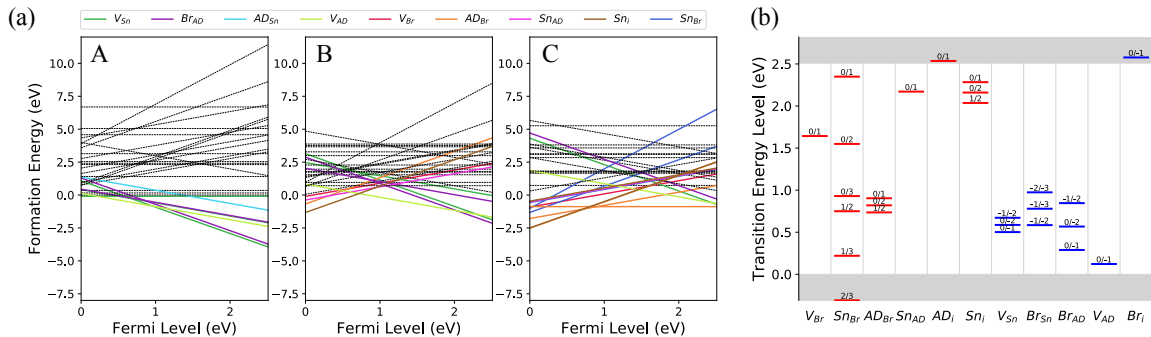


Figure B.13: Calculated (a) defect formation energy and (b) transition energy levels for AD_2SnBr_4 (tI14).

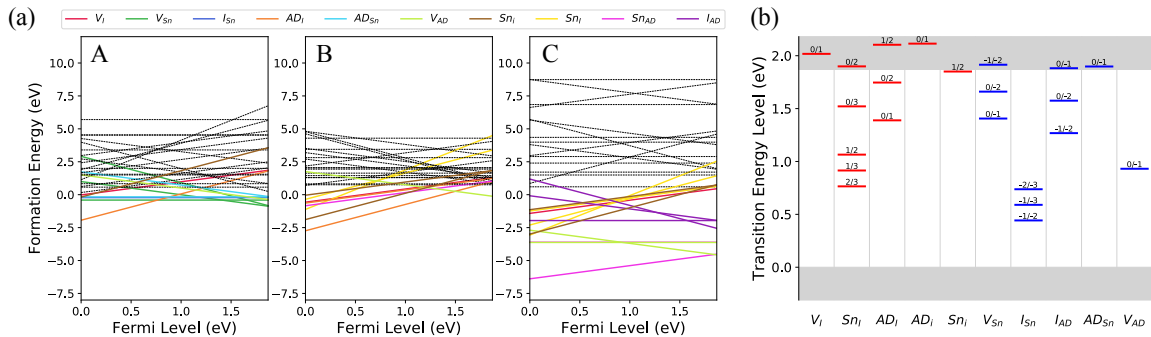


Figure B.14: Calculated (a) defect formation energy and (b) transition energy levels for AD_2SnI_4 (tI14).

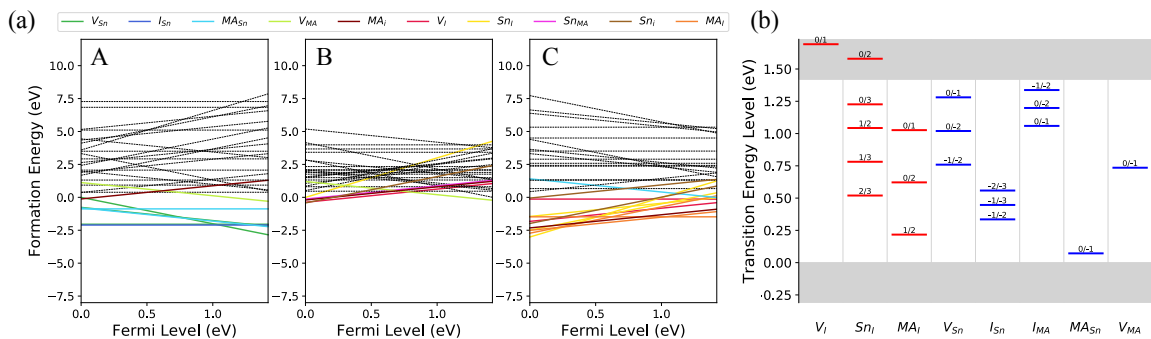


Figure B.15: Calculated (a) defect formation energy and (b) transition energy levels for MA_2SnI_4 (tI14).

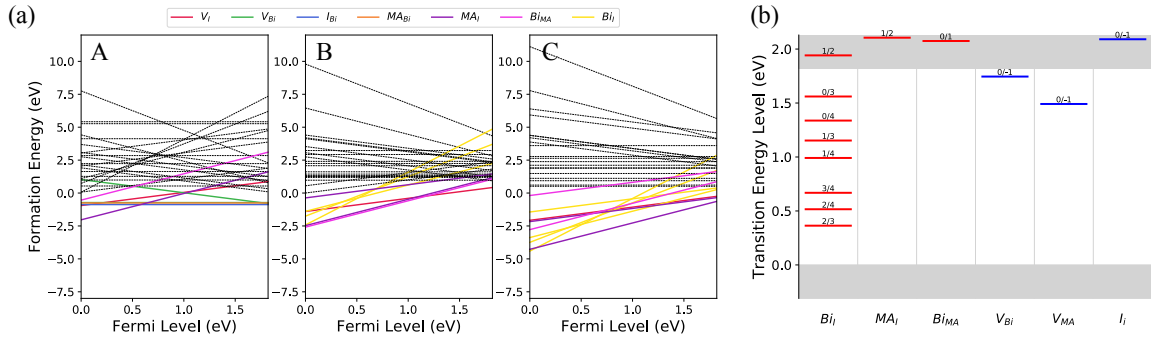


Figure B.19: Calculated (a) defect formation energy and (b) transition energy levels for MA₃Bi₂I₉ (hP14).

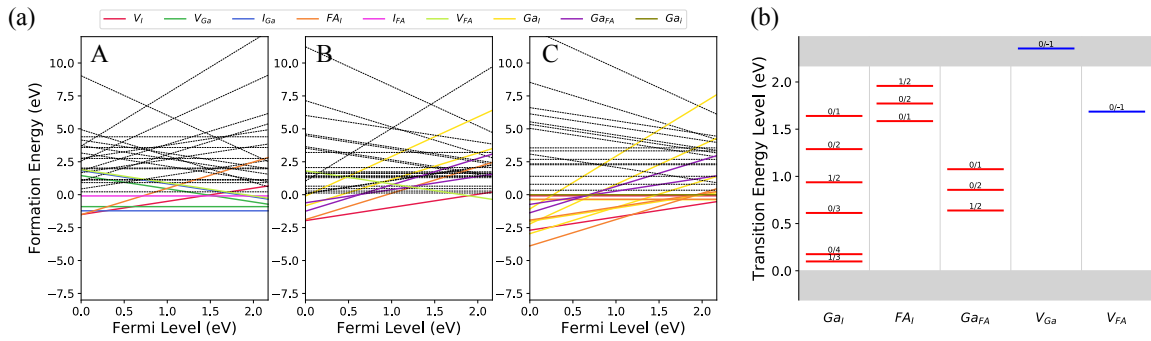


Figure B.20: Calculated (a) defect formation energy and (b) transition energy levels for FA₃Ga₂I₉ (hP14).

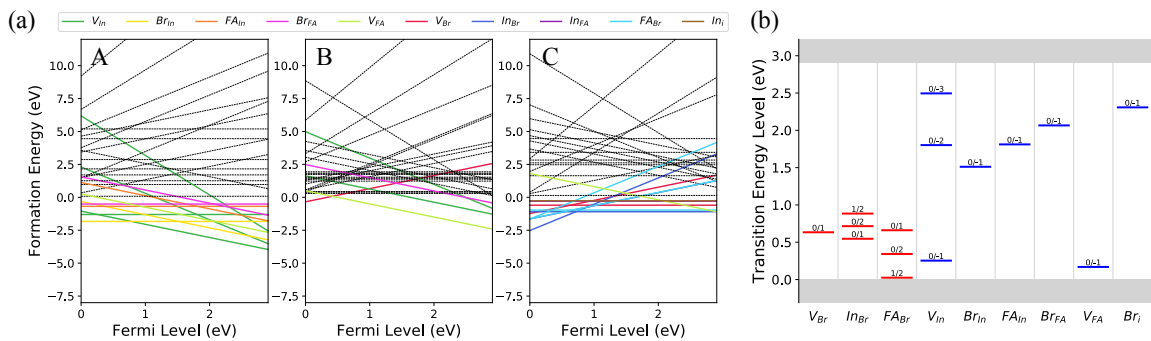


Figure B.21: Calculated (a) defect formation energy and (b) transition energy levels for FA₃In₂Br₉ (hP14).

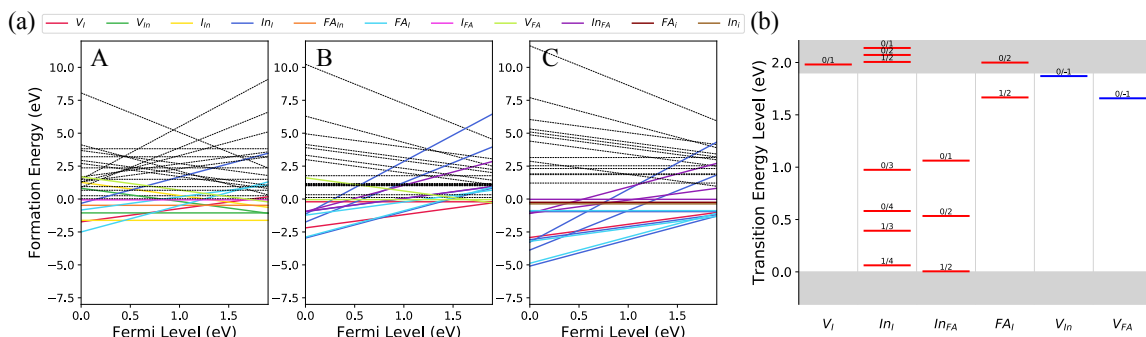


Figure B.22: Calculated (a) defect formation energy and (b) transition energy levels for $FA_3In_2I_9$ (hP14).

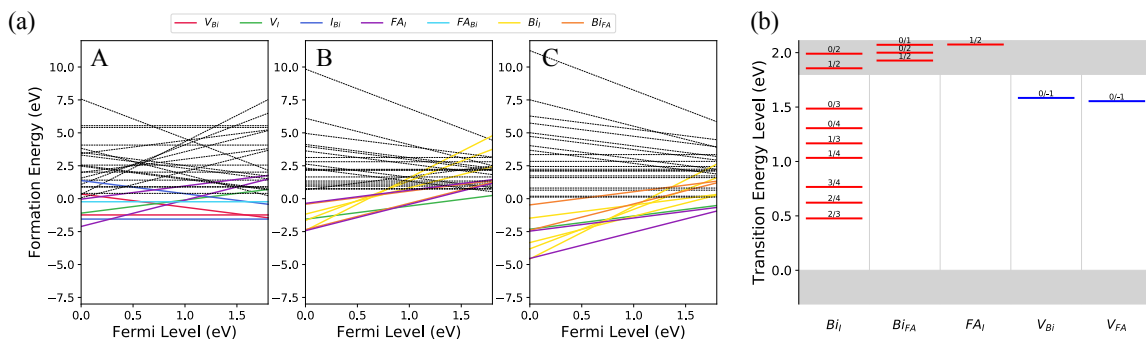


Figure B.23: Calculated (a) defect formation energy and (b) transition energy levels for $FA_3Bi_2I_9$ (hP14).

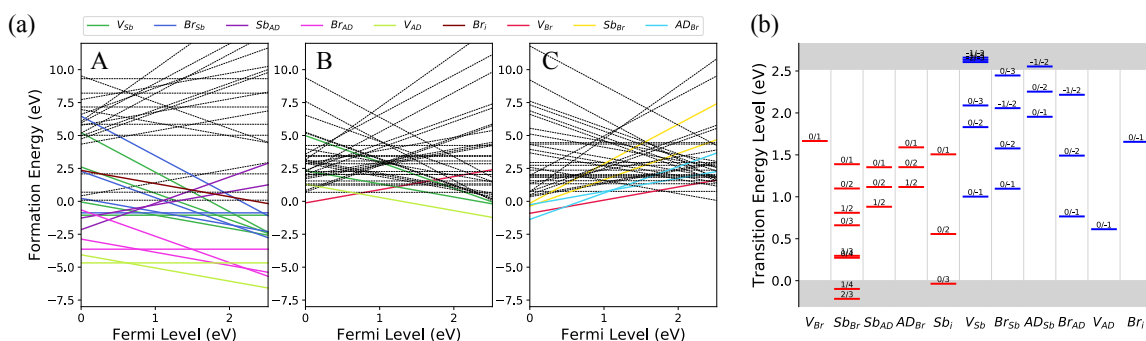


Figure B.24: Calculated (a) defect formation energy and (b) transition energy levels for $AD_3Sb_2Br_9$ (hP14).

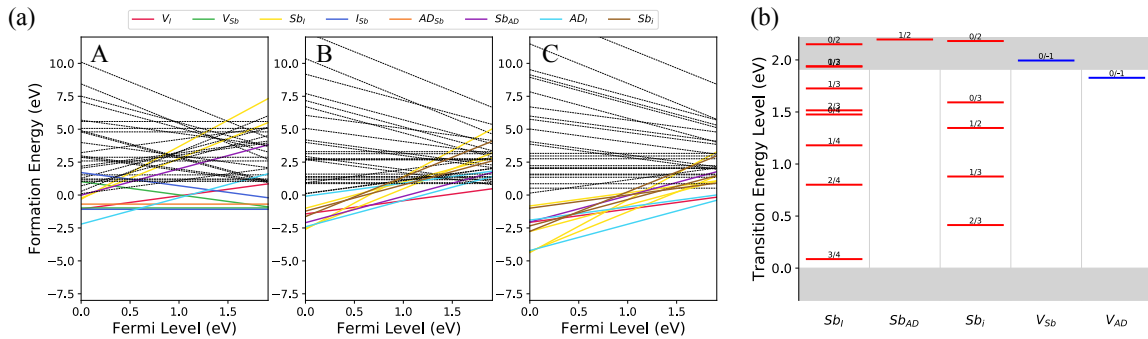


Figure B.25: Calculated (a) defect formation energy and (b) transition energy levels for $AD_3Sb_2I_9$ (hP14).

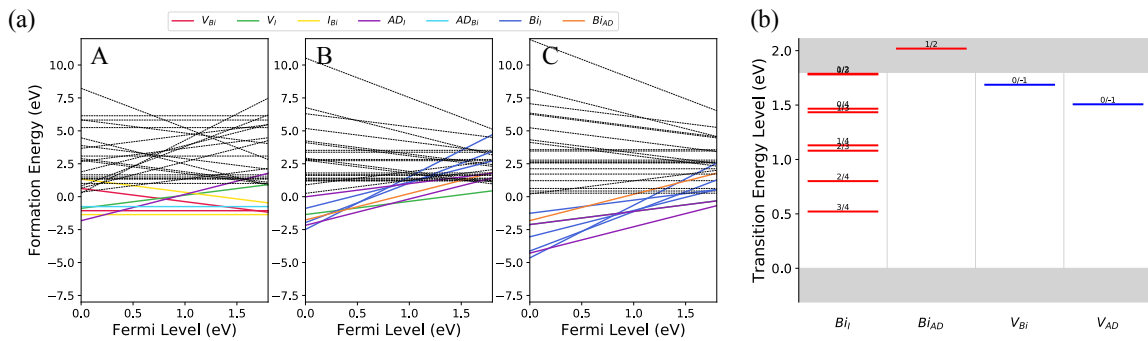


Figure B.26: Calculated (a) defect formation energy and (b) transition energy levels for $AD_3Bi_2I_9$ (hP14).

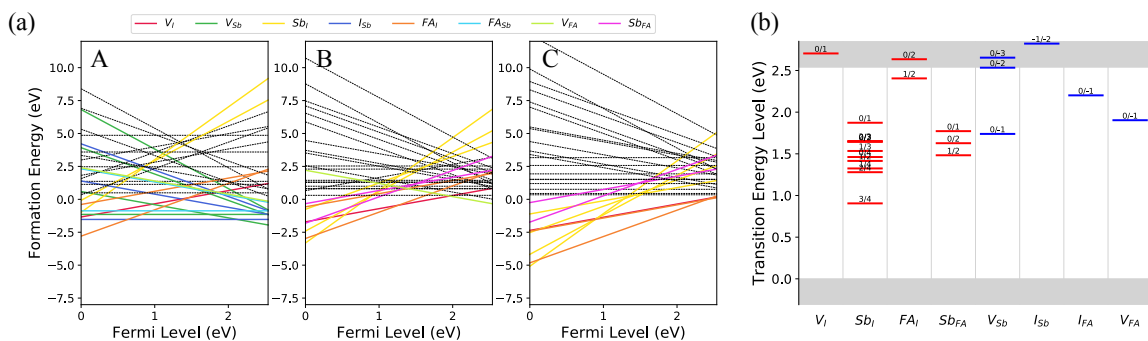


Figure B.27: Calculated (a) defect formation energy and (b) transition energy levels for $FA_3Sb_2I_9$ (hP28).

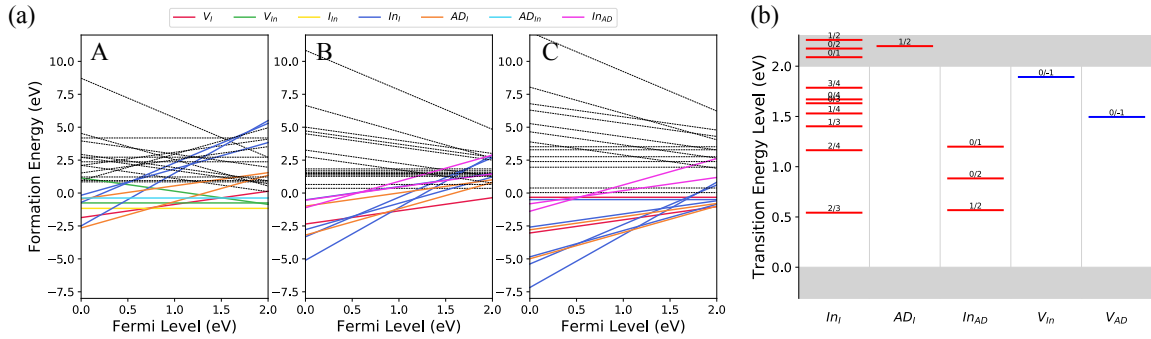


Figure B.28: Calculated (a) defect formation energy and (b) transition energy levels for $AD_3In_2I_9$ (hP14).

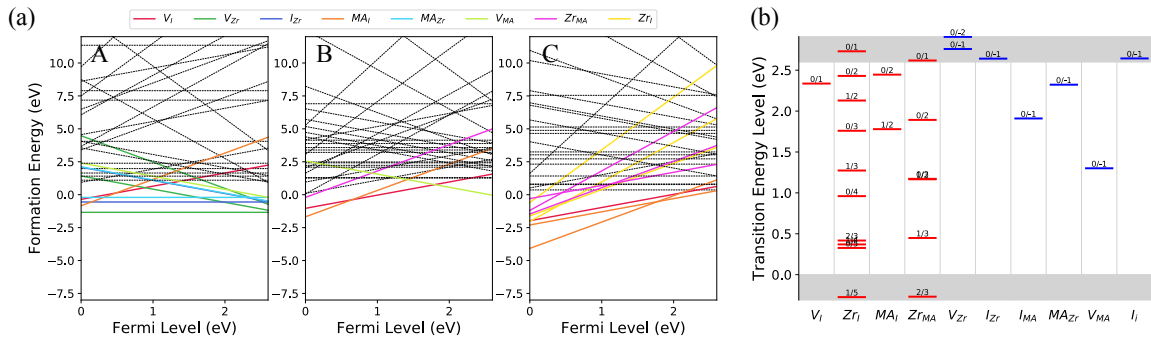


Figure B.29: Calculated (a) defect formation energy and (b) transition energy levels for MA_2ZrI_6 (tI18).

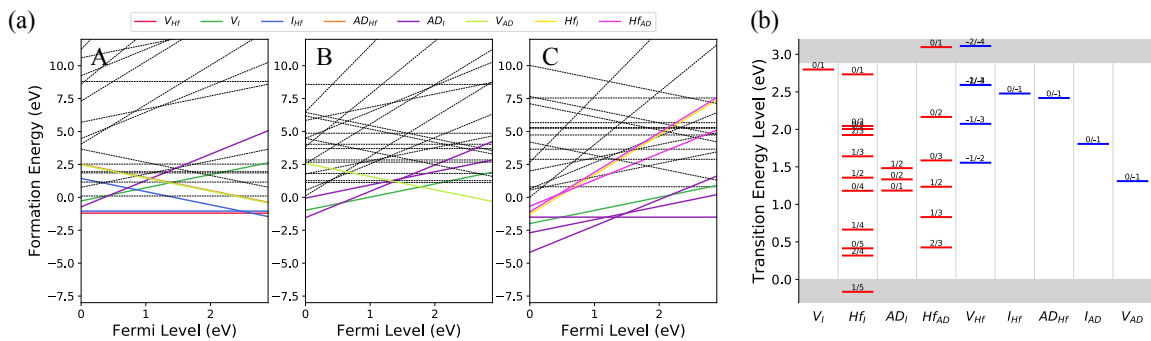


Figure B.30: Calculated (a) defect formation energy and (b) transition energy levels for AD_2HfI_6 (tI18).

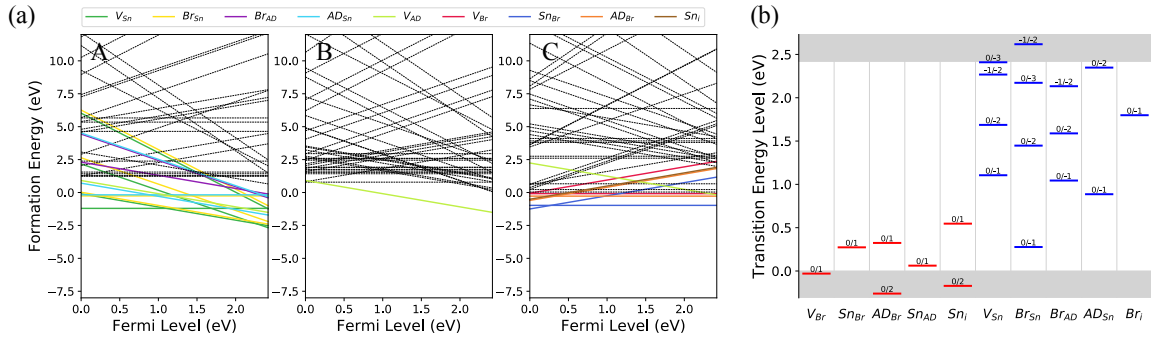


Figure B.31: Calculated (a) defect formation energy and (b) transition energy levels for AD_2SnBr_6 (tI18).

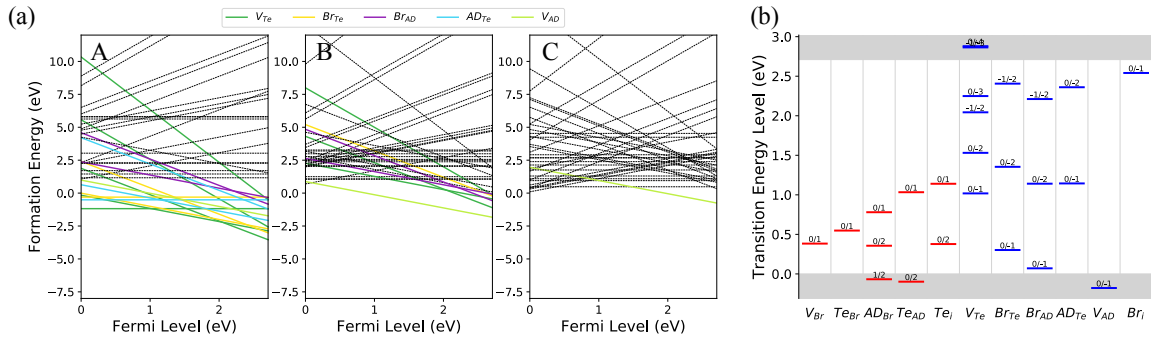


Figure B.32: Calculated (a) defect formation energy and (b) transition energy levels for AD_2TeBr_6 (tI18).

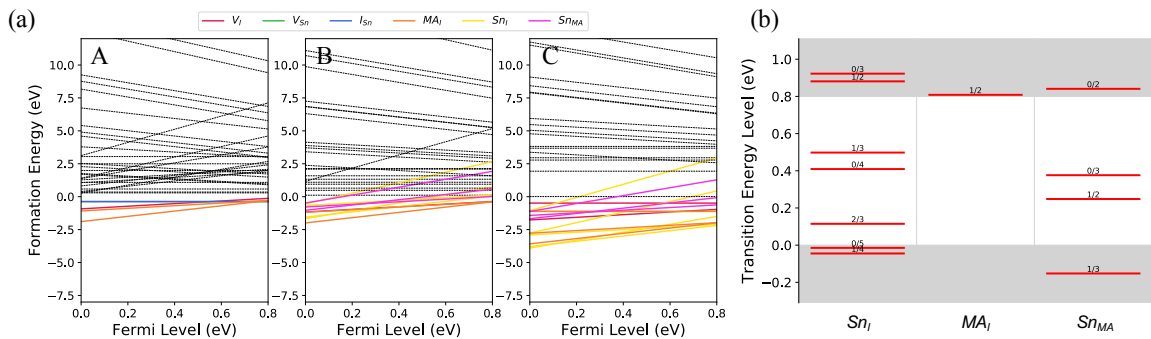


Figure B.33: Calculated (a) defect formation energy and (b) transition energy levels for MA_2SnI_6 (cF36).

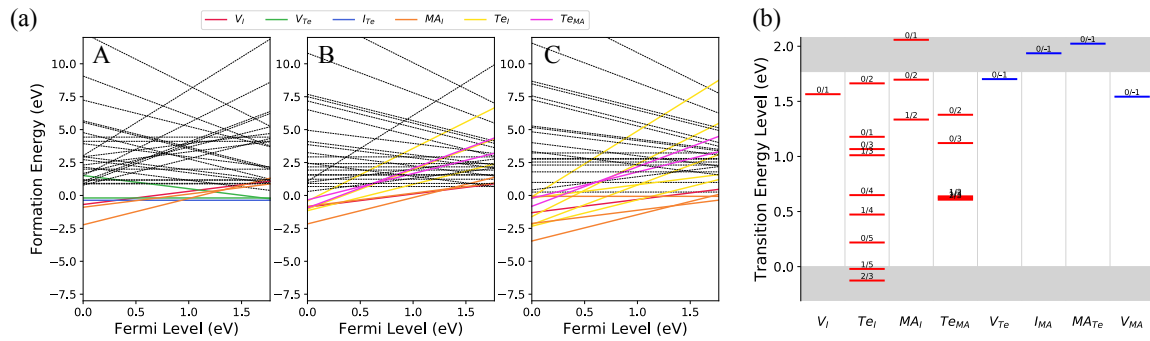


Figure B.34: Calculated (a) defect formation energy and (b) transition energy levels for MA_2TeI_6 (cF36).

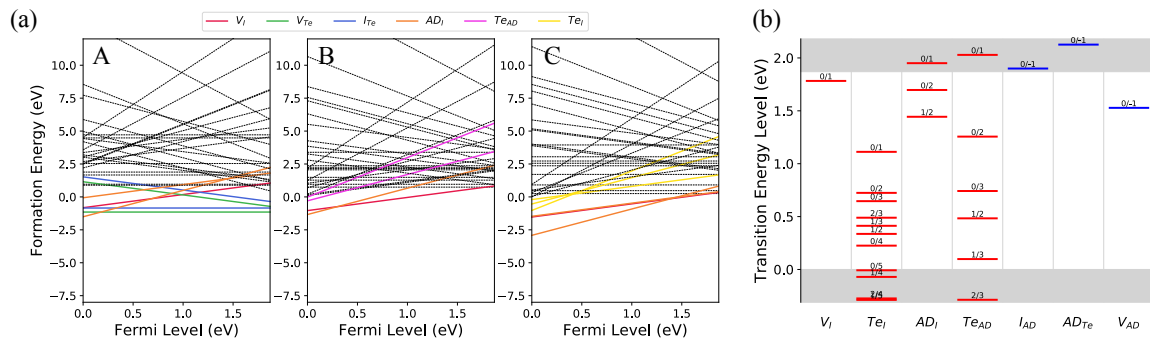


Figure B.35: Calculated (a) defect formation energy and (b) transition energy levels for AD_2TeI_6 (cF36).

Table B.2: Defect tolerance level determination for the tI14 compounds: List of defects that have low formations energies and create deep transition energy levels for these compounds at different synthesis chemical conditions A, B, and C. If all such defects can be prevented for one compound at some chemical condition(s), the compound has high defect tolerance. If such defects cannot be prevented for one compound at any chemical condition, the compound has low defect tolerance.

Compound ($A_xB_yX_z$)	Defect (q1/q2 @ Transition Level)			Defect Tolerance Level
	A (X-rich/B-poor)	B (X/B-moderate)	C (X-poor/B-rich)	
MA ₂ GeBr ₄	$Br_{MA}(-1/-2@0.87)$	–	–	high
MA ₂ GeI ₄	–	–	$Ge_I(2/3@0.67)$	high
MA ₂ SnCl ₄	$V_{Sn}(-1/-2@0.27)$ $Cl_{MA}(-1/-2@0.57)$ $V_{MA}(0/-1@0.34)$	$V_{Sn}(-1/-2@0.27)$ $Cl_{MA}(-1/-2@0.57)$ $V_{MA}(0/-1@0.34)$	$V_{Sn}(-1/-2@0.27)$	low
MA ₂ SnBr ₄	$Br_{MA}(-1/-2@0.63)$ $V_{MA}(0/-1@0.19)$	–	–	high
MA ₂ SnI ₄	$V_{Sn}(0/-2@1.02)$	–	$Sn_I(1/2@1.04)(2/3@0.52)$ $MA_I(0/1@1.03)(1/2@0.22)$	high
FA ₂ SnBr ₄	$V_{Sn}(-1/-2@0.77)$ $Br_{FA}(-1/-2@0.38)$	$Br_{FA}(-1/-2@0.38)$	–	high
AD ₂ GeI ₄	$AD_I(0/2@1.75)$	$AD_I(0/2@1.75)$ $Ge_i(1/2@1.92)$	$Ge_i(1/2@0.91)(2/3@0.55)$ $AD_I(0/2@1.75)$ $Ge_i(1/2@1.92)$	low
AD ₂ SnBr ₄	$V_{Sn}(0/-1@0.50)(-1/-2@0.67)$ $Br_{AD}(0/-1@0.29)(-1/-2@0.85)$	$V_{Sn}(-1/-2@0.67)$ $Br_{AD}(-1/-2@0.85)$ $Sn_i(1/2@2.04)$	$Sn_{Br}(1/2@0.75)$ $AD_{Br}(0/1@0.90)(1/2@0.74)$ $Sn_i(1/2@2.04)$	low
AD ₂ SnI ₄	–	–	$Sn_I(1/2@1.06)(2/3@0.76)$ $I_{AD}(0/-2@1.57)$ $V_{AD}(0/-1@0.93)$	high

Table B.3: Defect tolerance level determination for the hP14 compounds.

Compound ($A_xB_yX_z$)	Defect ($q1/q2$ @ Transition Level)			Defect Tolerance Level
	A (X-rich/B-poor)	B (X/B-moderate)	C (X-poor/B-rich)	
MA ₃ In ₂ I ₉	$MA_I(1/2@1.53)$	$In_I(1/2@1.44)$ $MA_I(1/2@1.53)$	$In_I(1/2@1.44)$ $MA_I(1/2@1.53)$	low
MA ₃ Sb ₂ Br ₉	$V_{Sb}(0/-1@0.85)$ $Br_{Sb}(0/-1@1.43)(-1/-2@1.77)$ $MA_{Sb}(-1/-2@2.35)$	$V_{MA}(0/-1@0.82)$	$MA_{Br}(1/2@0.89)$	low
MA ₃ Sb ₂ I ₉	–	$Sb_I(2/4@0.86)$ $Sb_i(1/2@1.10)(2/3@0.24)$	$Sb_I(2/4@0.86)$ $Sb_i(1/2@1.10)(2/3@0.24)$	high
MA ₃ Bi ₂ I ₉	–	$Bi_I(2/4@0.52)$	$Bi_I(2/4@0.52)$	high
FA ₃ Ga ₂ I ₉	$FA_I(0/2@1.77)$	$FA_I(0/2@1.77)$ $Ga_{FA}(1/2@0.64)$	$Ga_I(0/1@1.64)(1/2@0.94)$ $FA_I(0/2@1.77)$ $Ga_{FA}(1/2@0.64)$	low
FA ₃ In ₂ Br ₉	$Br_{In}(0/-1@1.51)$ $FA_{In}(0/-1@1.81)$ $Br_{FA}(0/-1@2.07)$	–	$V_{Br}(0/1@0.63)$ $In_{Br}(0/2@0.72)$ $FA_{Br}(0/1@0.66)$	high
FA ₃ In ₂ I ₉	$FA_I(1/2@1.67)$	$FA_I(1/2@1.67)$	$FA_I(1/2@1.67)$	low
FA ₃ Bi ₂ I ₉	$V_{Bi}(0/-1@1.58)$	$Bi_I(2/4@0.62)$	$Bi_I(2/4@0.62)$	low
AD ₃ Sb ₂ Br ₉	$V_{Sb}(0/-1@1.00)$ $Br_{Sb}(0/-1@1.10)(-1/-2@2.06)$ $Sb_{AD}(0/1@1.35)(1/2@0.88)$ $Br_{AD}(0/-1@0.77)(-1/-2@2.22)$	$V_{AD}(0/-1@0.61)$	$AD_{Br}(1/2@1.12)$	low
AD ₃ Sb ₂ I ₉	–	$Sb_I(2/3@1.52)$ $Sb_i(1/2@1.35)(2/3@0.41)$	$Sb_I(2/3@1.52)$ $Sb_i(1/2@1.35)(2/3@0.41)$	high
AD ₃ Bi ₂ I ₉	–	$Bi_I(2/3@1.08)(3/4@0.52)$	$Bi_I(2/3@1.08)(3/4@0.52)$	high

Table B.4: Defect tolerance level determination for the hP28 compounds.

Compound ($A_xB_yX_z$)	Defect (q1/q2 @ Transition Level)			Defect Tolerance Level
	A (X-rich/B-poor)	B (X/B-moderate)	C (X-poor/B-rich)	
FA ₃ Sb ₂ I ₉	$V_{Sb}(0/-1@1.74)$	$Sb_I(1/3@1.53)(3/4@0.91)$ $Sb_{FA}(1/2@1.48)$	$Sb_I(3/4@0.91)$ $Sb_{FA}(1/2@1.48)$	low
AD ₃ In ₂ I ₉	$In_I(2/4@1.16)$	$In_I(2/4@1.16)$	$In_I(2/4@1.16)$ $In_{AD}(1/2@0.57)$	low

Table B.5: Defect tolerance level determination for the tI18 compounds.

Compound ($A_xB_yX_z$)	Defect (q1/q2 @ Transition Level)			Defect Tolerance Level
	A (X-rich/B-poor)	B (X/B-moderate)	C (X-poor/B-rich)	
MA ₂ ZrI ₆	–	$MA_I(1/2@1.78)$	$V_I(0/1@2.34)$ $Zr_I(1/2@2.13)(2/3@0.42)$ $MA_I(1/2@1.78)$ $Zr_{MA}(1/2@1.17)$	high
AD ₂ HfI ₆	$Hf_I(0/-1@2.48)$	$AD_I(0/2@1.33)$	$Hf_I(1/3@1.64)$ $AD_I(0/2@1.33)$	low
AD ₂ SnBr ₆	$V_{Sn}(0/-1@1.11)$ $Br_{Sn}(0/-1@0.28)$ $AD_{Sn}(0/-1@0.89)$	–	$Sn_{Br}(0/1@0.27)$	high
AD ₂ TeBr ₆	$V_{Te}(0/-1@1.02)(-1/-2@2.04)$ $Br_{Te}(0/-1@0.30)(-1/-2@2.41)$ $AD_{Te}(0/-1@1.14)$	–	–	high

Table B.6: Defect tolerance level determination for the cF36 compounds.

Compound ($A_xB_yX_z$)	Defect (q1/q2 @ Transition Level)			Defect Tolerance Level
	A (X-rich/B-poor)	B (X/B-moderate)	C (X-poor/B-rich)	
MA ₂ SnI ₆	–	$Sn_I(2/3@0.11)$	$Sn_I(2/3@0.11)$ $Sn_{MA}(1/2@0.25)$	high
MA ₂ TeI ₆	$MA_I(1/2@1.33)$	$MA_I(1/2@1.33)$	$V_I(0/1@1.56)$ $MA_I(1/2@1.33)$	low
AD ₂ TeI ₆	$AD_I(1/2@1.44)$	$AD_I(1/2@1.44)$	$AD_I(1/2@1.44)$	low

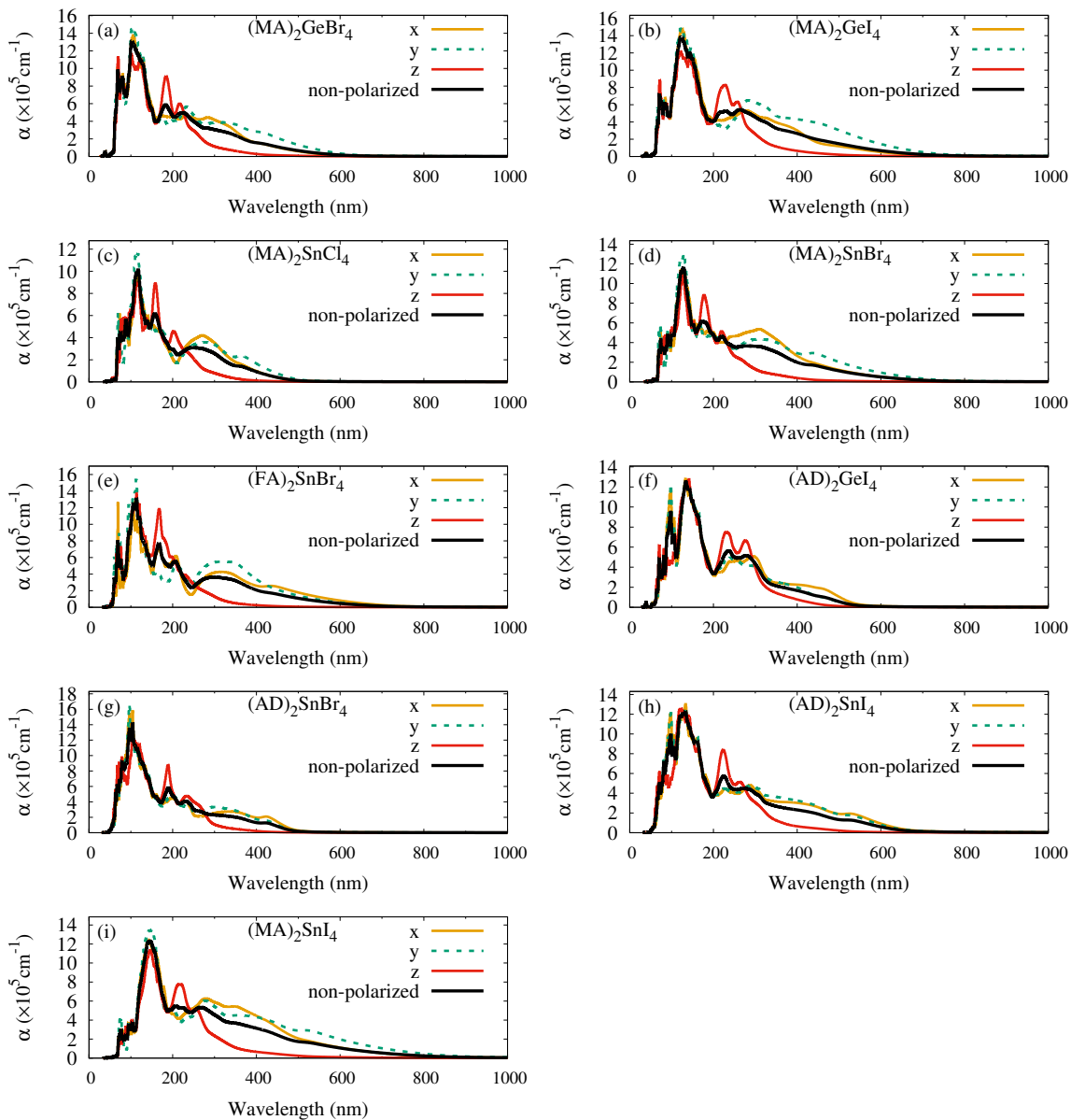


Figure B.36: Calculated optical absorption coefficients (α) for all the “tI14” compounds. In this and subsequent figures, the Pearson symbols of analogue inorganic compounds including tI14, hP14, tI18, cF36, and hP28 are used to distinguish the prototypes of the screened hybrid inorganic-organic materials.

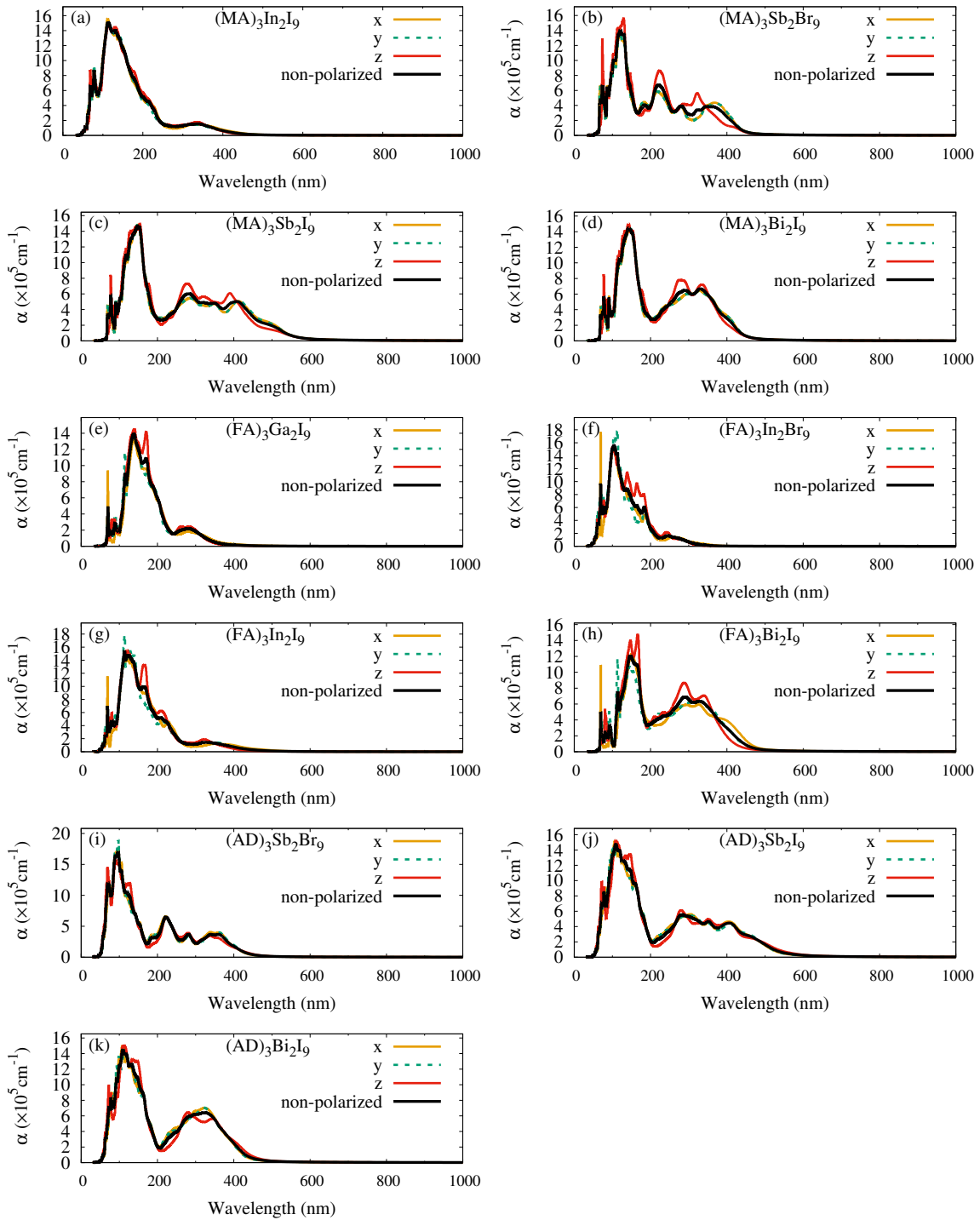


Figure B.37: Calculated optical absorption coefficients (α) for all the hP14 compounds.

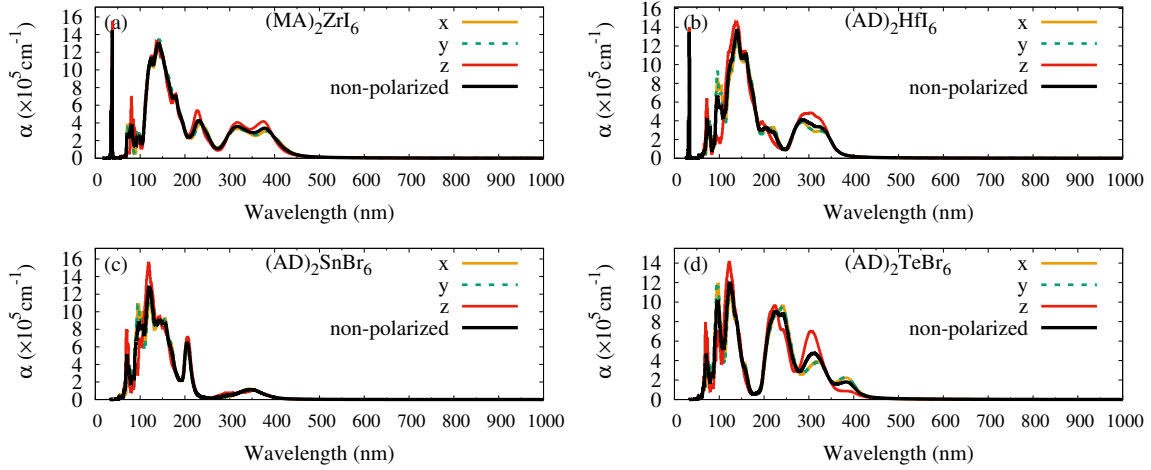


Figure B.38: Calculated optical absorption coefficients (α) for all the tI18 compounds.

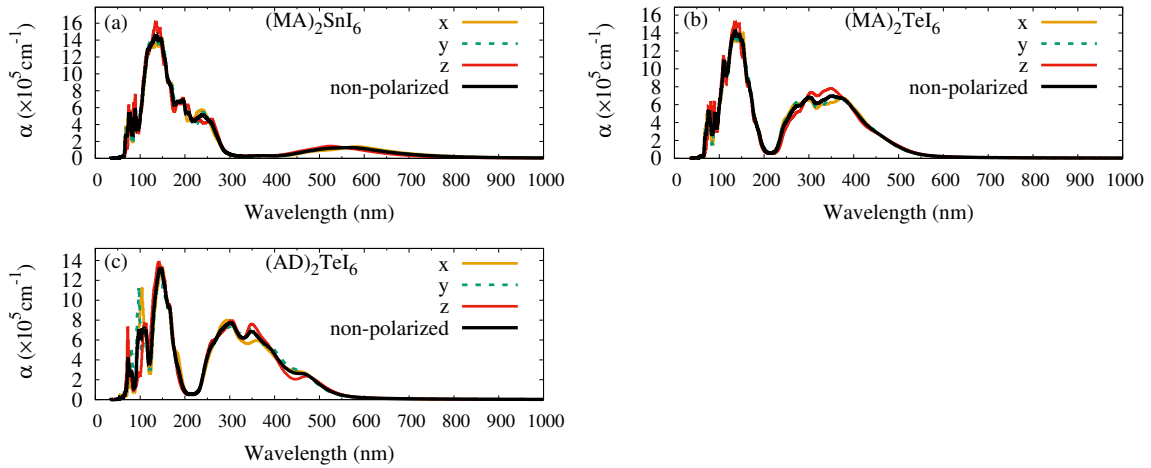


Figure B.39: Calculated optical absorption coefficients (α) for all the cF36 compounds.

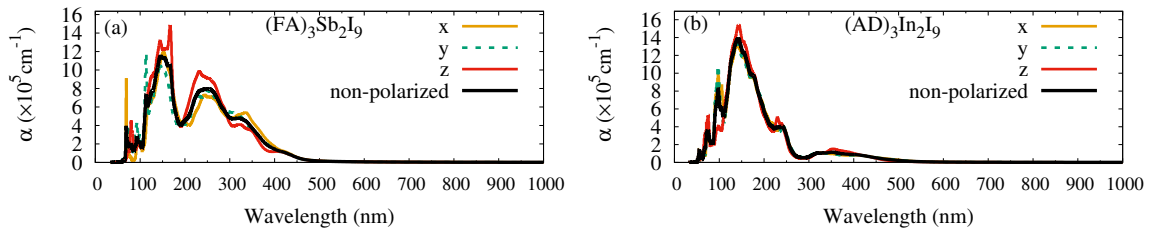


Figure B.40: Calculated optical absorption coefficients (α) for all the hP28 compounds.

References

- [1] A. Kojima, K. Teshima, Y. Shirai, and T. Miyasaka, *Organometal Halide Perovskites as Visible-Light Sensitizers for Photovoltaic Cells*, *J. Am. Chem. Soc.* **131**, 6050–6051 (2009).
- [2] N. J. Jeon, J. H. Noh, W. S. Yang, Y. C. Kim, S. Ryu, J. Seo, and S. I. Seok, *Compositional Engineering of Perovskite Materials for High-Performance Solar Cells*, *Nature* **517**, 476–480 (2015).
- [3] D. P. McMeekin, G. Sadoughi, W. Rehman, G. E. Eperon, M. Saliba, M. T. Hörantner, A. Haghighirad, N. Sakai, L. Korte, B. Rech, M. B. Johnston, L. M. Herz, and H. J. Snaith, *A Mixed-Cation Lead Mixed-Halide Perovskite Absorber for Tandem Solar Cells*, *Science* **351**, 151–155 (2016).
- [4] H. Zhou, Q. Chen, G. Li, S. Luo, T.-b. Song, H.-S. Duan, Z. Hong, J. You, Y. Liu, and Y. Yang, *Interface Engineering of Highly Efficient Perovskite Solar Cells*, *Science* **345**, 542–546 (2014).
- [5] S. A. Veldhuis, P. P. Boix, N. Yantara, M. Li, T. C. Sum, N. Mathews, and S. G. Mhaisalkar, *Perovskite Materials for Light-Emitting Diodes and Lasers*, *Adv. Mater.* **28**, 6804–6834 (2016).
- [6] Y. Chen, Y. Lei, Y. Li, Y. Yu, J. Cai, M.-H. Chiu, R. Rao, Y. Gu, C. Wang, W. Choi, H. Hu, C. Wang, Y. Li, J. Song, J. Zhang, B. Qi, M. Lin, Z. Zhang, A. E. Islam, B. Maruyama, S. Dayeh, L.-J. Li, K. Yang, Y.-H. Lo, and S. Xu, *Strain Engineering and Epitaxial Stabilization of Halide Perovskites*, *Nature* **577**, 209–215 (2020).
- [7] Y. Lei, Y. Chen, R. Zhang, Y. Li, Q. Yan, S. Lee, Y. Yu, H. Tsai, W. Choi, K. Wang, Y. Luo, Y. Gu, X. Zheng, C. Wang, C. Wang, H. Hu, Y. Li, B. Qi, M. Lin, Z. Zhang, S. A. Dayeh, M. Pharr, D. P. Fenning, Y.-H. Lo, J. Luo, K. Yang, J. Yoo, W. Nie, and S. Xu, *A Fabrication Process for Flexible Single-Crystal Perovskite Devices*, *Nature* **583**, 790–795 (2020).
- [8] NREL, *Best Research-Cell Efficiency Chart* (2020). [Online; accessed April 8, 2020].
- [9] K. Lin, J. Xing, L. N. Quan, F. P. G. de Arquer, X. Gong, J. Lu, L. Xie, W. Zhao, D. Zhang, C. Yan, W. Li, X. Liu, Y. Lu, J. Kirman, E. H. Sargent, Q. Xiong, and Z. Wei, *Perovskite*

- Light-Emitting Diodes with External Quantum Efficiency Exceeding 20 Per Cent*, Nature **562**, 245 (2018).
- [10] M. Grätzel, *The Light and Shade of Perovskite Solar Cells*, Nat. Mater. **13**, 838–842 (2014).
- [11] A. K. Jena, A. Kulkarni, and T. Miyasaka, *Halide Perovskite Photovoltaics: Background, Status, and Future Prospects*, Chem. Rev. **119**, 3036–3103 (2019).
- [12] Q. Dong, Y. Fang, Y. Shao, P. Mulligan, J. Qiu, L. Cao, and J. Huang, *Electron-Hole Diffusion Lengths > 175 μm in Solution-Grown $\text{CH}_3\text{NH}_3\text{PbI}_3$ Single Crystals*, Science **347**, 967–970 (2015).
- [13] G. Xing, N. Mathews, S. Sun, S. S. Lim, Y. M. Lam, M. Grätzel, S. Mhaisalkar, and T. C. Sum, *Long-Range Balanced Electron- and Hole-Transport Lengths in Organic–Inorganic $\text{CH}_3\text{NH}_3\text{PbI}_3$* , Science **342**, 344–347 (2013).
- [14] C. Wehrenfennig, G. E. Eperon, M. B. Johnston, H. J. Snaith, and L. M. Herz, *High Charge Carrier Mobilities and Lifetimes in Organolead Trihalide Perovskites*, Adv. Mater. **26**, 1584–1589 (2014).
- [15] Y. Li, M. Behtash, J. Wong, and K. Yang, *Enhancing Ferroelectric Dipole Ordering in Organic-Inorganic Hybrid Perovskite $\text{CH}_3\text{NH}_3\text{PbI}_3$: Strain and Doping Engineering*, J. Phys. Chem. C **122**, 177–184 (2018).
- [16] W.-J. Yin, T. Shi, and Y. Yan, *Unusual Defect Physics in $\text{CH}_3\text{NH}_3\text{PbI}_3$ Perovskite Solar Cell Absorber*, Appl. Phys. Lett. **104**, 063903 (2014).
- [17] A. Walsh, D. O. Scanlon, S. Chen, X. Gong, and S.-H. Wei, *Self-Regulation Mechanism for Charged Point Defects in Hybrid Halide Perovskites*, Angew. Chem. Int. Ed. **54**, 1791–1794 (2015).
- [18] A. T. Barrows, A. J. Pearson, C. K. Kwak, A. D. Dunbar, A. R. Buckley, and D. G. Lidzey, *Efficient Planar Heterojunction Mixed-Halide Perovskite Solar Cells Deposited via Spray-Deposition*, Energy Environ. Sci. **7**, 2944–2950 (2014).
- [19] H. Zhu, K. Miyata, Y. Fu, J. Wang, P. P. Joshi, D. Niesner, K. W. Williams, S. Jin, and X.-Y. Zhu, *Screening in Crystalline Liquids Protects Energetic Carriers in Hybrid Perovskites*, Science **353**, 1409–1413 (2016).
- [20] H. Zhu, M. T. Trinh, J. Wang, Y. Fu, P. P. Joshi, K. Miyata, S. Jin, and X.-Y. Zhu, *Organic Cations Might Not Be Essential to the Remarkable Properties of Band Edge Carriers in Lead Halide Perovskites*, Adv. Mater. **29**, 1603072 (2017).
- [21] K. Miyata, D. Meggiolaro, M. T. Trinh, P. P. Joshi, E. Mosconi, S. C. Jones, F. De Angelis, and X.-Y. Zhu, *Large Polarons in Lead Halide Perovskites*, Sci. Adv. **3**, e1701217 (2017).

- [22] J. M. Frost, K. T. Butler, F. Brivio, C. H. Hendon, M. Van Schilfgaarde, and A. Walsh, *Atomistic Origins of High-Performance in Hybrid Halide Perovskite Solar Cells*, *Nano Lett.* **14**, 2584–2590 (2014).
- [23] A. Stroppa, C. Quarti, F. De Angelis, and S. Picozzi, *Ferroelectric Polarization of $CH_3NH_3PbI_3$: a Detailed Study Based on Density Functional Theory and Symmetry Mode Analysis*, *J. Phys. Chem. Lett.* **6**, 2223–2231 (2015).
- [24] F. Zheng, H. Takenaka, F. Wang, N. Z. Koocher, and A. M. Rappe, *First-Principles Calculation of the Bulk Photovoltaic Effect in $CH_3NH_3PbI_3$ and $CH_3NH_3PbI_{3-x}Cl_x$* , *J. Phys. Chem. Lett.* **6**, 31–37 (2014).
- [25] Z. Fan, J. Xiao, K. Sun, L. Chen, Y. Hu, J. Ouyang, K. P. Ong, K. Zeng, and J. Wang, *Ferroelectricity of $CH_3NH_3PbI_3$ Perovskite*, *J. Phys. Chem. Lett.* **6**, 1155–1161 (2015).
- [26] Y. Kutes, L. Ye, Y. Zhou, S. Pang, B. D. Huey, and N. P. Padture, *Direct Observation of Ferroelectric Domains in Solution-Processed $CH_3NH_3PbI_3$ Perovskite Thin Films*, *J. Phys. Chem. Lett.* **5**, 3335–3339 (2014).
- [27] H.-S. Kim, S. K. Kim, B. J. Kim, K.-S. Shin, M. K. Gupta, H. S. Jung, S.-W. Kim, and N.-G. Park, *Ferroelectric Polarization in $CH_3NH_3PbI_3$ Perovskite*, *J. Phys. Chem. Lett.* **6**, 1729–1735 (2015).
- [28] M. T. Weller, O. J. Weber, P. F. Henry, A. M. Di Pumpo, and T. C. Hansen, *Complete Structure and Cation Orientation in the Perovskite Photovoltaic Methylammonium Lead Iodide between 100 and 352 K*, *Chem. Commun.* **51**, 4180–4183 (2015).
- [29] G. Sharada, P. Mahale, B. P. Kore, S. Mukherjee, M. S. Pavan, C. De, S. Ghara, A. Sundaresan, A. Pandey, T. N. G. Row, and D. D. Sarma, *Is $CH_3NH_3PbI_3$ Polar?*, *J. Phys. Chem. Lett.* **7**, 2412–2419 (2016).
- [30] Y. Rakita, E. Meirzadeh, T. Bendikov, V. Kalchenko, I. Lubomirsky, G. Hodes, D. Ehre, and D. Cahen, *$CH_3NH_3PbBr_3$ Is Not Pyroelectric, Excluding Ferroelectric-Enhanced Photovoltaic Performance*, *APL Mater.* **4**, 051101 (2016).
- [31] Y. Rakita, O. Bar-Elli, E. Meirzadeh, H. Kaslasi, Y. Peleg, G. Hodes, I. Lubomirsky, D. Oron, D. Ehre, and D. Cahen, *Tetragonal $CH_3NH_3PbI_3$ Is Ferroelectric*, *Proc. Natl. Acad. Sci.* **114**, E5504–E5512 (2017).
- [32] D. Bryant, N. Aristidou, S. Pont, I. Sanchez-Molina, T. Chotchunangatchaval, S. Wheeler, J. R. Durrant, and S. A. Haque, *Light and Oxygen Induced Degradation Limits the Operational Stability of Methylammonium Lead Triiodide Perovskite Solar Cells*, *Energy Environ. Sci.* **9**, 1655–1660 (2016).
- [33] B. Conings, J. Drijkoningen, N. Gauquelin, A. Babayigit, J. D’Haen, L. D’Olieslaeger, A. Ethirajan, J. Verbeeck, J. Manca, E. Mosconi, F. D. Angelis, and H. Boyen, *Intrinsic*

- Thermal Instability of Methylammonium Lead Trihalide Perovskite*, *Adv. Energy Mater.* **5**, 1500477 (2015).
- [34] F. Giustino and H. J. Snaith, *Toward Lead-Free Perovskite Solar Cells*, *ACS Energy Lett.* **1**, 1233–1240 (2016).
- [35] S. Chakraborty, W. Xie, N. Mathews, M. Sherburne, R. Ahuja, M. Asta, and S. G. Mhaisalkar, *Rational Design: A High-Throughput Computational Screening and Experimental Validation Methodology for Lead-Free and Emergent Hybrid Perovskites*, *ACS Energy Lett.* **2**, 837–845 (2017).
- [36] C. Huo, B. Cai, Z. Yuan, B. Ma, and H. Zeng, *Two-Dimensional Metal Halide Perovskites: Theory, Synthesis, and Optoelectronics*, *Small Methods* **1**, 1600018 (2017).
- [37] A. Jodlowski, D. Rodríguez-Padrón, R. Luque, and G. de Miguel, *Alternative Perovskites for Photovoltaics*, *Adv. Energy Mater.* **8**, 1703120 (2018).
- [38] Q. Xu, D. Yang, J. Lv, Y.-Y. Sun, and L. Zhang, *Perovskite Solar Absorbers: Materials by Design*, *Small Methods* **2**, 1700316 (2018).
- [39] X.-G. Zhao, D. Yang, J.-C. Ren, Y. Sun, Z. Xiao, and L. Zhang, *Rational Design of Halide Double Perovskites for Optoelectronic Applications*, *Joule* **2**, 1662–1673 (2018).
- [40] Z. Xiao, Z. Song, and Y. Yan, *From Lead Halide Perovskites to Lead-Free Metal Halide Perovskites and Perovskite Derivatives*, *Adv. Mater.* **31**, 1803792 (2019).
- [41] J. Greeley, T. F. Jaramillo, J. Bonde, I. Chorkendorff, and J. K. Nørskov, *Computational High-Throughput Screening of Electrocatalytic Materials for Hydrogen Evolution*, *Nat. Mater.* **5**, 909–913 (2006).
- [42] G. Ceder, *Opportunities and Challenges for First-Principles Materials Design and Applications to Li Battery Materials*, *MRS Bull.* **35**, 693–701 (2010).
- [43] S. Wang, Z. Wang, W. Setyawan, N. Mingo, and S. Curtarolo, *Assessing the Thermoelectric Properties of Sintered Compounds via High-Throughput Ab-Initio Calculations*, *Phys. Rev. X* **1**, 021012 (2011).
- [44] R. Armiento, B. Kozinsky, M. Fornari, and G. Ceder, *Screening for High-Performance Piezoelectrics Using High-Throughput Density Functional Theory*, *Phys. Rev. B* **84**, 014103 (2011).
- [45] K. Yang, W. Setyawan, S. Wang, M. B. Nardelli, and S. Curtarolo, *A Search Model for Topological Insulators with High-Throughput Robustness Descriptors*, *Nat. Mater.* **11**, 614–619 (2012).
- [46] S. Curtarolo, G. L. W. Hart, M. B. Nardelli, N. Mingo, S. Sanvito, and O. Levy, *The High-Throughput Highway to Computational Materials Design*, *Nat. Mater.* **12**, 191–201 (2013).

- [47] R. Armiento, B. Kozinsky, G. Hautier, M. Fornari, and G. Ceder, *High-Throughput Screening of Perovskite Alloys for Piezoelectric Performance and Thermodynamic Stability*, Phys. Rev. B **89**, 134103 (2014).
- [48] R. Gautier, X. Zhang, L. Hu, L. Yu, Y. Lin, T. O. Sunde, D. Chon, K. R. Poeppelmeier, and A. Zunger, *Prediction and Accelerated Laboratory Discovery of Previously Unknown 18-Electron ABX Compounds*, Nat. Chem. **7**, 308 (2015).
- [49] G. Brunin, F. Ricci, V.-A. Ha, G.-M. Rignanese, and G. Hautier, *Transparent Conducting Materials Discovery Using High-Throughput Computing*, npj Comput. Mater. **5**, 63 (2019).
- [50] S. Sanvito, C. Oses, J. Xue, A. Tiwari, M. Zic, T. Archer, P. Tozman, M. Venkatesan, M. Coey, and S. Curtarolo, *Accelerated Discovery of New Magnets in the Heusler Alloy Family*, Sci. Adv. **3**, e1602241 (2017).
- [51] K. Yang, S. Nazir, M. Behtash, and J. Cheng, *High-Throughput Design of Two-Dimensional Electron Gas Systems Based on Polar/Nonpolar Perovskite Oxide Heterostructures*, Sci. Rep. **6**, 34667 (2016).
- [52] K. Yang, *High-Throughput Design of Functional Materials Using Materials Genome Approach*, Chin. Phys. B **27**, 128103 (2018).
- [53] J. Cheng and K. Yang, *Design of Two-Dimensional Electron Gas Systems via Polarization Discontinuity from Large-Scale First-Principles Calculations*, J. Mater. Chem. C **6**, 6680–6690 (2018).
- [54] S. Curtarolo, W. Setyawan, S. Wang, J. Xue, K. Yang, R. H. Taylor, L. J. Nelson, G. L. W. Hart, S. Sanvito, M. B. Nardelli, N. Mingo, and O. Levy, *AFLOWLIB.ORG: A Distributed Materials Properties Repository from High-Throughput ab Initio Calculations*, Comput. Mater. Sci. **58**, 227–235 (2012).
- [55] S. P. Ong, W. D. Richards, A. Jain, G. Hautier, M. Kocher, S. Cholia, D. Gunter, V. L. Chevrier, K. A. Persson, and G. Ceder, *Python Materials Genomics (pymatgen): A Robust, Open-Source Python Library for Materials Analysis*, Comput. Mater. Sci. **68**, 314–319 (2013).
- [56] A. H. Larsen, J. J. Mortensen, J. Blomqvist, I. E. Castelli, R. Christensen, M. Dułak, J. Friis, M. N. Groves, B. Hammer, C. Hargus, E. D. Hermes, P. C. Jennings, P. B. Jensen, J. Kermode, J. R. Kitchin, E. L. Kolsbjerg, J. Kubal, K. Kaasbjerg, S. Lysgaard, J. B. Maronsson, T. Maxson, T. Olsen, L. Pastewka, A. Peterson, C. Rostgaard, J. Schiøtz, O. Schütt, M. Strange, K. S. Thygesen, T. Vegge, L. Vilhelmsen, M. Walter, Z. Zeng, and K. W. Jacobsen, *The Atomic Simulation Environment—A Python Library for Working with Atoms*, J. Phys.: Condens. Matter **29**, 273002 (2017).
- [57] X. Yang, Z. Wang, X. Zhao, J. Song, M. Zhang, and H. Liu, *MatCloud: A High-Throughput Computational Infrastructure for Integrated Management of Materials Simulation, Data and Resources*, Comput. Mater. Sci. **146**, 319–333 (2018).

- [58] A. Jain, S. P. Ong, G. Hautier, W. Chen, W. D. Richards, S. Dacek, S. Cholia, D. Gunter, D. Skinner, G. Ceder, and K. A. Persson, *Commentary: The Materials Project: A Materials Genome Approach to Accelerating Materials Innovation*, *APL Mater.* **1**, 011002 (2013).
- [59] J. E. Saal, S. Kirklin, M. Aykol, B. Meredig, and C. Wolverton, *Materials Design and Discovery with High-Throughput Density Functional Theory: The Open Quantum Materials Database (OQMD)*, *JOM* **65**, 1501–1509 (2013).
- [60] D. D. Landis, J. S. Hummelshoj, S. Nestorov, J. Greeley, M. Dulak, T. Bligaard, J. K. Nørskov, and K. W. Jacobsen, *The Computational Materials Repository*, *Comput. Sci. Eng.* **14**, 51–57 (2012).
- [61] Y. Li and K. Yang, *High-Throughput Computational Design of Halide Perovskites and Beyond for Optoelectronics*, *WIREs Comput. Mol. Sci.* **Early View**, e1500 (2020).
- [62] D. Yang, J. Lv, X. Zhao, Q. Xu, Y. Fu, Y. Zhan, A. Zunger, and L. Zhang, *Functionality-Directed Screening of Pb-Free Hybrid Organic–Inorganic Perovskites with Desired Intrinsic Photovoltaic Functionalities*, *Chem. Mater.* **29**, 524–538 (2017).
- [63] Y. Cai, W. Xie, Y. T. Teng, P. C. Harikesh, B. Ghosh, P. Huck, K. A. Persson, N. Mathews, S. G. Mhaisalkar, M. Sherburne, and M. Asta, *High-Throughput Computational Study of Halide Double Perovskite Inorganic Compounds*, *Chem. Mater.* **31**, 5392–5401 (2019).
- [64] C. J. Bartel, J. M. Clary, C. Sutton, D. Vigil-Fowler, B. R. Goldsmith, A. M. Holder, and C. B. Musgrave, *Inorganic Halide Double Perovskites with Optoelectronic Properties Modulated by Sublattice Mixing*, *J. Am. Chem. Soc.* **142**, 5135–5145 (2020).
- [65] Q. Chen, N. De Marco, Y. M. Yang, T.-B. Song, C.-C. Chen, H. Zhao, Z. Hong, H. Zhou, and Y. Yang, *Under the Spotlight: The Organic–Inorganic Hybrid Halide Perovskite for Optoelectronic Applications*, *Nano. Today* **10**, 355–396 (2015).
- [66] G. Kieslich, S. Sun, and A. K. Cheetham, *Solid-State Principles Applied to Organic–Inorganic Perovskites: New Tricks for an Old Dog*, *Chem. Sci.* **5**, 4712–4715 (2014).
- [67] G. Kieslich, S. Sun, and A. K. Cheetham, *An Extended Tolerance Factor Approach for Organic–Inorganic Perovskites*, *Chem. Sci.* **6**, 3430–3433 (2015).
- [68] R. D. Shannon, *Revised Effective Ionic Radii and Systematic Studies of Interatomic Distances in Halides and Chalcogenides*, *Acta Crystallogr. Sect. A* **32**, 751–767 (1976).
- [69] W. Travis, E. Glover, H. Bronstein, D. Scanlon, and R. Palgrave, *On the Application of the Tolerance Factor to Inorganic and Hybrid Halide Perovskites: a Revised System*, *Chem. Sci.* **7**, 4548–4556 (2016).
- [70] C. J. Bartel, C. Sutton, B. R. Goldsmith, R. Ouyang, C. B. Musgrave, L. M. Ghiringhelli, and M. Scheffler, *New Tolerance Factor to Predict the Stability of Perovskite Oxides and Halides*, *Sci. Adv.* **5**, eaav0693 (2019).

- [71] N.-G. Park, M. Grätzel, T. Miyasaka, K. Zhu, and K. Emery, *Towards Stable and Commercially Available Perovskite Solar Cells*, *Nat. Energy*. **1**, 16152 (2016).
- [72] Y. Li and K. Yang, *High-Throughput Computational Design of Organic-Inorganic Hybrid Halide Semiconductors Beyond Perovskites for Optoelectronics*, *Energy Environ. Sci.* **12**, 2233–2243 (2019).
- [73] X.-G. Zhao, J.-H. Yang, Y. Fu, D. Yang, Q. Xu, L. Yu, S.-H. Wei, and L. Zhang, *Design of Lead-Free Inorganic Halide Perovskites for Solar Cells via Cation-Transmutation*, *J. Am. Chem. Soc.* **139**, 2630–2638 (2017).
- [74] Z. Xiao, K.-Z. Du, W. Meng, J. Wang, D. B. Mitzi, and Y. Yan, *Intrinsic Instability of $Cs_2In(I)M(III)X_6$ ($M = Bi, Sb$; $X = \text{Halogen}$) Double Perovskites: A Combined Density Functional Theory and Experimental Study*, *J. Am. Chem. Soc.* **139**, 6054–6057 (2017).
- [75] Z. Xiao, K.-Z. Du, W. Meng, D. B. Mitzi, and Y. Yan, *Chemical Origin of the Stability Difference between Copper(I)- and Silver(I)-Based Halide Double Perovskites*, *Angew. Chem.* **129**, 12275–12279 (2017).
- [76] S. Hu, B. Xia, Y.-P. Lin, T. Katase, J. Fujioka, T. Kamiya, H. Hosono, K.-Z. Du, and Z. Xiao, *p-Type Transparent Quadruple Perovskite Halide Conductors: Fact or Fiction?*, *Adv. Fun. Mater.* p. 1909906 (2020).
- [77] M. R. Filip, X. Liu, A. Miglio, G. Hautier, and F. Giustino, *Phase Diagrams and Stability of Lead-Free Halide Double Perovskites $Cs_2BB'X_6$: $B = Sb$ and Bi , $B' = Cu, Ag$, and Au , and $X = Cl, Br$, and I* , *J. Phys. Chem. C* **122**, 158–170 (2018).
- [78] S. P. Ong, L. Wang, B. Kang, and G. Ceder, *Li-Fe-P-O₂ Phase Diagram from First Principles Calculations*, *Chem. Mater.* **20**, 1798–1807 (2008).
- [79] Z. Huo, S.-H. Wei, and W.-J. Yin, *High-Throughput Screening of Chalcogenide Single Perovskites by First-Principles Calculations for Photovoltaics*, *J. Phys. D: Appl. Phys.* **51**, 474003 (2018).
- [80] S. Lu, Q. Zhou, Y. Ouyang, Y. Guo, Q. Li, and J. Wang, *Accelerated Discovery of Stable Lead-Free Hybrid Organic-Inorganic Perovskites via Machine Learning*, *Nat. Commun.* **9**, 3405 (2018).
- [81] A. Polman, M. Knight, E. C. Garnett, B. Ehrler, and W. C. Sinke, *Photovoltaic Materials: Present Efficiencies and Future Challenges*, *Science* **352**, aad4424 (2016).
- [82] W. Shockley and H. J. Queisser, *Detailed Balance Limit of Efficiency of P-N Junction Solar Cells*, *J. Appl. Phys.* **32**, 510–519 (1961).
- [83] J. P. Perdew, K. Burke, and M. Ernzerhof, *Generalized Gradient Approximation Made Simple*, *Phys. Rev. Lett.* **77**, 3865–3868 (1996).

- [84] J. Heyd, G. E. Scuseria, and M. Ernzerhof, *Hybrid Functionals Based on a Screened Coulomb Potential*, *J. Chem. Phys.* **118**, 8207–8215 (2003).
- [85] J. Even, L. Pedesseau, J.-M. Jancu, and C. Katan, *Importance of Spin–Orbit Coupling in Hybrid Organic/Inorganic Perovskites for Photovoltaic Applications*, *J. Phys. Chem. Lett.* **4**, 2999–3005 (2013).
- [86] G. Giorgi, J.-I. Fujisawa, H. Segawa, and K. Yamashita, *Small Photocarrier Effective Masses Featuring Ambipolar Transport in Methylammonium Lead Iodide Perovskite: A Density Functional Analysis*, *J. Phys. Chem. Lett.* **4**, 4213–4216 (2013).
- [87] Z. Xiao, W. Meng, J. Wang, D. B. Mitzi, and Y. Yan, *Searching for Promising New Perovskite-Based Photovoltaic Absorbers: the Importance of Electronic Dimensionality*, *Mater. Horizons* **4**, 206–216 (2017).
- [88] L.-y. Huang and W. R. Lambrecht, *Electronic Band Structure, Phonons, and Exciton Binding Energies of Halide Perovskites CsSnCl₃, CsSnBr₃, and CsSnI₃*, *Phys. Rev. B* **88**, 165203 (2013).
- [89] W.-J. Yin, J.-H. Yang, J. Kang, Y. Yan, and S.-H. Wei, *Halide Perovskite Materials for Solar Cells: A Theoretical Review*, *J. Mater. Chem. A* **3**, 8926–8942 (2015).
- [90] Z. Xiao and Y. Yan, *Progress in Theoretical Study of Metal Halide Perovskite Solar Cell Materials*, *Adv. Energy Mater.* **7**, 1701136 (2017).
- [91] S. Saha, T. P. Sinha, and A. Mookerjee, *Electronic Structure, Chemical Bonding, and Optical Properties of Paraelectric BaTiO₃*, *Phys. Rev. B* **62**, 8828–8834 (2000).
- [92] L. Wu, P. Lu, Y. Li, Y. Sun, J. Wong, and K. Yang, *First-Principles Characterization of Two-Dimensional (CH₃(CH₂)₃NH₃)₂(CH₃NH₃)_{n-1}Ge_nI_{3n+1} Perovskite*, *J. Mater. Chem. A* **6**, 24389–24396 (2018).
- [93] Y. Li, D. Maldonado-Lopez, V. Ríos Vargas, J. Zhang, and K. Yang, *Stability Diagrams, Defect Tolerance, and Absorption Coefficients of Hybrid Halide Semiconductors: High-Throughput First-Principles Characterization*, *J. Chem. Phys.* **152**, 084106 (2020).
- [94] G. Giorgi, K. Yamashita, and M. Palummo, *Nature of the Electronic and Optical Excitations of Ruddlesden–Popper Hybrid Organic–Inorganic Perovskites: The Role of the Many-Body Interactions*, *J. Phys. Chem. Lett.* **9**, 5891–5896 (2018).
- [95] Y. Cho and T. C. Berkelbach, *Optical Properties of Layered Hybrid Organic–Inorganic Halide Perovskites: A Tight-Binding GW-BSE Study*, *J. Phys. Chem. Lett.* **10**, 6189–6196 (2019).
- [96] C. Freysoldt, B. Grabowski, T. Hickel, J. Neugebauer, G. Kresse, A. Janotti, and C. G. Van de Walle, *First-Principles Calculations for Point Defects in Solids*, *Rev. Mod. Phys.* **86**, 253 (2014).

- [97] Y. Kumagai and F. Oba, *Electrostatics-Based Finite-Size Corrections for First-Principles Point Defect Calculations*, Phys. Rev. B **89**, 195205 (2014).
- [98] S. Lany and A. Zunger, *Assessment of Correction Methods for the Band-Gap Problem and for Finite-Size Effects in Supercell Defect Calculations: Case Studies for ZnO and GaAs*, Phys. Rev. B **78**, 235104 (2008).
- [99] D. Broberg, B. Medasani, N. E. Zimmermann, G. Yu, A. Canning, M. Haranczyk, M. Asta, and G. Hautier, *PyCDT: A Python Toolkit for Modeling Point Defects in Semiconductors and Insulators*, Comput. Phys. Commun. **226**, 165–179 (2018).
- [100] X. He, Z. Xiao, T. Katase, K. Ide, H. Hosono, and T. Kamiya, *Intrinsic and Extrinsic Defects in Layered Nitride Semiconductor SrTiN₂*, J. Phys. Chem. C **123**, 19307–19314 (2019).
- [101] A. A. Emery, J. E. Saal, S. Kirklin, V. I. Hegde, and C. Wolverton, *High-Throughput Computational Screening of Perovskites for Thermochemical Water Splitting Applications*, Chem. Mater. **28**, 5621–5634 (2016).
- [102] T. Krishnamoorthy, H. Ding, C. Yan, W. L. Leong, T. Baikie, Z. Zhang, M. Sherburne, S. Li, M. Asta, N. Mathews, and S. G. Mhaisalkar, *Lead-Free Germanium Iodide Perovskite Materials for Photovoltaic Applications*, J. Mater. Chem. A **3**, 23829–23832 (2015).
- [103] M. Kuok, L. Tan, Z. Shen, C. Huan, and K. Mok, *A Raman Study of RbSnBr₃*, Solid State Commun. **97**, 497–501 (1996).
- [104] D. H. Fabini, G. Laurita, J. S. Bechtel, C. C. Stoumpos, H. A. Evans, A. G. Kontos, Y. S. Raptis, P. Falaras, A. Van der Ven, M. G. Kanatzidis, and R. Seshadri, *Dynamic Stereochemical Activity of the Sn²⁺ Lone Pair in Perovskite CsSnBr₃*, J. Am. Chem. Soc. **138**, 11820–11832 (2016).
- [105] X. Wu, W. Song, Q. Li, X. Zhao, D. He, and Z. Quan, *Synthesis of Lead-Free CsGeI₃ Perovskite Colloidal Nanocrystals and Electron Beam-Induced Transformations*, Chem. Asian J. **13**, 1654–1659 (2018).
- [106] L.-C. Tang, J. Y. Huang, C. Chang, M. Lee, and L. Liu, *New Infrared Nonlinear Optical Crystal CsGeBr₃: Synthesis, Structure and Powder Second-Harmonic Generation Properties*, J. Phys.: Condens. Matter **17**, 7275 (2005).
- [107] C. C. Stoumpos, C. D. Malliakas, and M. G. Kanatzidis, *Semiconducting Tin and Lead Iodide Perovskites with Organic Cations: Phase Transitions, High Mobilities, and Near-Infrared Photoluminescent Properties*, Inorganic chemistry **52**, 9019–9038 (2013).
- [108] M. H. Kumar, S. Dharani, W. L. Leong, P. P. Boix, R. R. Prabhakar, T. Baikie, C. Shi, H. Ding, R. Ramesh, M. Asta, M. Graetzel, S. G. Mhaisalkar, and N. Mathews, *Lead-Free Halide Perovskite Solar Cells with High Photocurrents Realized Through Vacancy Modulation*, Adv. Mater. **26**, 7122–7127 (2014).

- [109] S. Sharma, N. Weiden, and A. Weiss, *Phase Transitions in CsSnCl₃ and CsPbBr₃ An NMR and NQR Study*, *Zeitschrift Für Naturforschung A* **46**, 329–336 (1991).
- [110] N. K. Noel, S. D. Stranks, A. Abate, C. Wehrenfennig, S. Guarnera, A.-A. Haghighirad, A. Sadhanala, G. E. Eperon, S. K. Pathak, M. B. Johnston, A. Petrozza, L. M. Herz, and H. J. Snaith, *Lead-Free Organic–Inorganic Tin Halide Perovskites for Photovoltaic Applications*, *Energy Environ. Sci.* **7**, 3061–3068 (2014).
- [111] F. Hao, C. C. Stoumpos, D. H. Cao, R. P. Chang, and M. G. Kanatzidis, *Lead-Free Solid-State Organic–Inorganic Halide Perovskite Solar Cells*, *Nat. Photon.* **8**, 489 (2014).
- [112] W. Liao, D. Zhao, Y. Yu, N. Shrestha, K. Ghimire, C. R. Grice, C. Wang, Y. Xiao, A. J. Cimaroli, R. J. Ellingson, N. J. Podraza, K. Zhu, R.-G. Xiong, and Y. Yan, *Fabrication of Efficient Low-Bandgap Perovskite Solar Cells by Combining Formamidinium Tin Iodide with Methylammonium Lead Iodide*, *J. Am. Chem. Soc.* **138**, 12360–12363 (2016).
- [113] T. Nakajima and K. Sawada, *Discovery of Pb-Free Perovskite Solar Cells via High-Throughput Simulation on the K Computer*, *J. Phys. Chem. Lett.* **8**, 4826–4831 (2017).
- [114] R. Jacobs, G. Luo, and D. Morgan, *Materials Discovery of Stable and Nontoxic Halide Perovskite Materials for High-Efficiency Solar Cells*, *Adv. Fun. Mater.* **29**, 1804354 (2019).
- [115] M. R. Filip and F. Giustino, *Computational Screening of Homovalent Lead Substitution in Organic–Inorganic Halide Perovskites*, *J. Phys. Chem. C* **120**, 166–173 (2016).
- [116] K. M. McCall, D. Friedrich, D. G. Chica, W. Cai, C. C. Stoumpos, G. C. Alexander, S. Deemyad, B. W. Wessels, and M. G. Kanatzidis, *Perovskites with a Twist: Strong In¹⁺ Off-Centering in the Mixed-Valent CsInX₃ (X= Cl, Br)*, *Chem. Mater.* **31**, 9554–9566 (2019).
- [117] R. Ali, G.-J. Hou, Z.-G. Zhu, Q.-B. Yan, Q.-R. Zheng, and G. Su, *Predicted Lead-Free Perovskites for Solar Cells*, *Chem. Mater.* **30**, 718–728 (2018).
- [118] L. Debbichi, S. Lee, H. Cho, A. M. Rappe, K.-H. Hong, M. S. Jang, and H. Kim, *Mixed Valence Perovskite Cs₂Au₂I₆: A Potential Material for Thin-Film Pb-Free Photovoltaic Cells with Ultrahigh Efficiency*, *Adv. Mater.* **30**, 1707001 (2018).
- [119] G. García-Espejo, D. Rodríguez-Padrón, R. Luque, L. Camacho, and G. de Miguel, *Mechanochemical Synthesis of Three Double Perovskites: Cs₂AgBiBr₆, (CH₃NH₃)₂TlBiBr₆ and Cs₂AgSbBr₆*, *Nanoscale* **11**, 16650–16657 (2019).
- [120] Y.-J. Li, T. Wu, L. Sun, R.-X. Yang, L. Jiang, P.-F. Cheng, Q.-Q. Hao, T.-J. Wang, R.-F. Lu, and W.-Q. Deng, *Lead-Free and Stable Antimony–Silver-Halide Double Perovskite (CH₃NH₃)₂AgSbI₆*, *RSC Adv.*, **7**, 35175–35180 (2017).

- [121] Y. Bekenstein, J. C. Dahl, J. Huang, W. T. Osowiecki, J. K. Swabeck, E. M. Chan, P. Yang, and A. P. Alivisatos, *The Making and Breaking of Lead-Free Double Perovskite Nanocrystals of Cesium Silver–Bismuth Halide Compositions*, *Nano Lett.* **18**, 3502–3508 (2018).
- [122] S. E. Creutz, E. N. Crites, M. C. De Siena, and D. R. Gamelin, *Colloidal Nanocrystals of Lead-Free Double-Perovskite (Elpasolite) Semiconductors: Synthesis and Anion Exchange to Access New Materials*, *Nano Lett.* **18**, 1118–1123 (2018).
- [123] X.-G. Zhao, D. Yang, Y. Sun, T. Li, L. Zhang, L. Yu, and A. Zunger, *Cu–In Halide Perovskite Solar Absorbers*, *J. Am. Chem. Soc.* **139**, 6718–6725 (2017).
- [124] T. T. Tran, M. A. Quintero, K. E. Arpino, Z. A. Kelly, J. R. Panella, X. Wang, and T. M. McQueen, *Chemically Controlled Crystal Growth of $(\text{CH}_3\text{NH}_3)_2\text{AgInBr}_6$* , *CrystEngComm* **20**, 5929–5934 (2018).
- [125] A. Jain, O. Voznyy, and E. H. Sargent, *High-Throughput Screening of Lead-Free Perovskite-Like Materials for Optoelectronic Applications*, *J. Phys. Chem. C* **121**, 7183–7187 (2017).
- [126] E. Y. Peresh, V. Sidei, N. Gaborets, O. Zubaka, I. Stercho, and I. Barchii, *Influence of the Average Atomic Number of the A_2TeC_6 and $\text{A}_3\text{B}_2\text{C}_9$ ($\text{A} = \text{K}, \text{Rb}, \text{Cs}, \text{Tl(I)}$; $\text{B} = \text{Sb}, \text{Bi}$; $\text{C} = \text{Br}, \text{I}$) Compounds on Their Melting Point and Band Gap*, *Inorg. Mater.* **50**, 101–106 (2014).
- [127] G. Tang, Z. Xiao, H. Hosono, T. Kamiya, D. Fang, and J. Hong, *Layered Halide Double Perovskites $\text{Cs}_{3+n}\text{M(II)}_n\text{Sb}_2\text{X}_{9+3n}$ ($\text{M} = \text{Sn}, \text{Ge}$) for Photovoltaic Applications*, *J. Phys. Chem. Lett.* **9**, 43–48 (2018).
- [128] Z. Liu, X. Zhao, A. Zunger, and L. Zhang, *Design of Mixed-Cation Tri-Layered Pb-Free Halide Perovskites for Optoelectronic Applications*, *Adv. Electron. Mater.* **5**, 1900234 (2019).
- [129] P. Harikesh, H. K. Mulmudi, B. Ghosh, T. W. Goh, Y. T. Teng, K. Thirumal, M. Lockrey, K. Weber, T. M. Koh, S. Li, S. Mhaisalkar, and N. Mathews, *Rb as an Alternative Cation for Templating Inorganic Lead-Free Perovskites for Solution Processed Photovoltaics*, *Chem. Mater.* **28**, 7496–7504 (2016).
- [130] B. Saparov, F. Hong, J.-P. Sun, H.-S. Duan, W. Meng, S. Cameron, I. G. Hill, Y. Yan, and D. B. Mitzi, *Thin-Film Preparation and Characterization of $\text{Cs}_3\text{Sb}_2\text{I}_9$: A Lead-Free Layered Perovskite Semiconductor*, *Chem. Mater.* **27**, 5622–5632 (2015).
- [131] A. J. Lehner, D. H. Fabini, H. A. Evans, C.-A. Hébert, S. R. Smock, J. Hu, H. Wang, J. W. Zwanziger, M. L. Chabiny, and R. Seshadri, *Crystal and Electronic Structures of Complex Bismuth Iodides $\text{A}_3\text{Bi}_2\text{I}_9$ ($\text{A} = \text{K}, \text{Rb}, \text{Cs}$) Related to Perovskite: Aiding the Rational Design of Photovoltaics*, *Chem. Mater.* **27**, 7137–7148 (2015).

- [132] K. M. Boopathi, P. Karuppuswamy, A. Singh, C. Hanmandlu, L. Lin, S. A. Abbas, C. C. Chang, P. C. Wang, G. Li, and C. W. Chu, *Solution-Processable Antimony-Based Light-Absorbing Materials Beyond Lead Halide Perovskites*, *J. Mater. Chem. A* **5**, 20843–20850 (2017).
- [133] J.-C. Hebig, I. Kühn, J. Flohre, and T. Kirchartz, *Optoelectronic Properties of $(\text{CH}_3\text{NH}_3)_3\text{Sb}_2\text{I}_9$ Thin Films for Photovoltaic Applications*, *ACS Energy Lett.* **1**, 309–314 (2016).
- [134] A. E. Maughan, A. M. Ganose, M. M. Bordelon, E. M. Miller, D. O. Scanlon, and J. R. Neilson, *Defect Tolerance to Intolerance in the Vacancy-Ordered Double Perovskite Semiconductors Cs_2SnI_6 and Cs_2TeI_6* , *J. Am. Chem. Soc.* **138**, 8453–8464 (2016).
- [135] B. Saparov, J.-P. Sun, W. Meng, Z. Xiao, H.-S. Duan, O. Gunawan, D. Shin, I. G. Hill, Y. Yan, and D. B. Mitzi, *Thin-Film Deposition and Characterization of a Sn-Deficient Perovskite Derivative Cs_2SnI_6* , *Chem. Mater.* **28**, 2315–2322 (2016).
- [136] S. De Wolf, J. Holovsky, S.-J. Moon, P. Löper, B. Niesen, M. Ledinsky, F.-J. Haug, J.-H. Yum, and C. Ballif, *Organometallic Halide Perovskites: Sharp Optical Absorption Edge and Its Relation to Photovoltaic Performance*, *J. Phys. Chem. Lett.* **5**, 1035–1039 (2014).
- [137] Y. Liao, H. Liu, W. Zhou, D. Yang, Y. Shang, Z. Shi, B. Li, X. Jiang, L. Zhang, L. N. Quan, R. Quintero-Bermudez, B. R. Sutherland, Q. Mi, E. H. Sargent, and Z. Ning, *Highly Oriented Low-Dimensional Tin Halide Perovskites with Enhanced Stability and Photovoltaic Performance*, *J. Am. Chem. Soc.* **139**, 6693–6699 (2017).
- [138] F. Hao, C. C. Stoumpos, P. Guo, N. Zhou, T. J. Marks, R. P. Chang, and M. G. Kanatzidis, *Solvent-Mediated Crystallization of $\text{CH}_3\text{NH}_3\text{SnI}_3$ Films for Heterojunction Depleted Perovskite Solar Cells*, *J. Am. Chem. Soc.* **137**, 11445–11452 (2015).
- [139] M. R. Filip, S. Hillman, A. A. Haghighirad, H. J. Snaith, and F. Giustino, *Band Gaps of the Lead-Free Halide Double Perovskites $\text{Cs}_2\text{BiAgCl}_6$ and $\text{Cs}_2\text{BiAgBr}_6$ from Theory and Experiment*, *J. Phys. Chem. Lett.* **7**, 2579–2585 (2016).
- [140] E. T. McClure, M. R. Ball, W. Windl, and P. M. Woodward, *$\text{Cs}_2\text{AgBiX}_6$ ($X = \text{Br}, \text{Cl}$): New Visible Light Absorbing, Lead-Free Halide Perovskite Semiconductors*, *Chem. Mater.* **28**, 1348–1354 (2016).
- [141] A. H. Slavney, T. Hu, A. M. Lindenberg, and H. I. Karunadasa, *A Bismuth-Halide Double Perovskite with Long Carrier Recombination Lifetime for Photovoltaic Applications*, *J. Am. Chem. Soc.* **138**, 2138–2141 (2016).
- [142] F. Wei, Z. Deng, S. Sun, F. Xie, G. Kieslich, D. M. Evans, M. A. Carpenter, P. D. Bristowe, and A. K. Cheetham, *The Synthesis, Structure and Electronic Properties of a Lead-Free Hybrid Inorganic–organic Double Perovskite ($\text{MA}_2\text{KBiCl}_6$ ($\text{MA} = \text{Methylammonium}$))*, *Mater. Horizons* **3**, 328–332 (2016).

- [143] J. Luo, X. Wang, S. Li, J. Liu, Y. Guo, G. Niu, L. Yao, Y. Fu, L. Gao, Q. Dong, C. Zhao, M. Leng, F. Ma, W. Liang, L. Wang, S. Jin, J. Han, L. Zhang, J. Etheridge, J. Wang, Y. Yan, E. H. Sargent, and J. Tang, *Efficient and Stable Emission of Warm-White Light from Lead-Free Halide Double Perovskites*, *Nature* **563**, 541 (2018).
- [144] M.-G. Ju, M. Chen, Y. Zhou, J. Dai, L. Ma, N. P. Padture, and X. C. Zeng, *Toward Eco-Friendly and Stable Perovskite Materials for Photovoltaics*, *Joule* **2**, 1231–1241 (2018).
- [145] F. Jiang, D. Yang, Y. Jiang, T. Liu, X. Zhao, Y. Ming, B. Luo, F. Qin, J. Fan, H. Han, L. Zhang, and Y. Zhou, *Chlorine-Incorporation-Induced Formation of the Layered Phase for Antimony-Based Lead-Free Perovskite Solar Cells*, *J. Am. Chem. Soc.* **140**, 1019–1027 (2018).
- [146] N. Pai, J. Lu, T. R. Gengenbach, A. Seeber, A. S. Chesman, L. Jiang, D. C. Senevirathna, P. C. Andrews, U. Bach, Y.-B. Cheng, and A. N. Simonov, *Silver Bismuth Sulfoiodide Solar Cells: Tuning Optoelectronic Properties by Sulfide Modification for Enhanced Photovoltaic Performance*, *Adv. Energy Mater.* **9**, 1803396 (2019).
- [147] S. Curtarolo, W. Setyawan, G. L. W. Hart, M. Jahnatek, R. V. Chepulskii, R. H. Taylor, S. Wang, J. Xue, K. Yang, O. Levy, M. Mehl, H. T. Stokes, D. O. Demchenko, , and D. Morgan, *AFLOW: an Automatic Framework for High-Throughput Materials Discovery*, *Comput. Mater. Sci.* **58**, 218–226 (2012).
- [148] G. Kresse and D. Joubert, *From Ultrasoft Pseudopotentials to the Projector Augmented-Wave Method*, *Phys. Rev. B* **59**, 1758–1775 (1999).
- [149] J. P. Perdew, K. Burke, and M. Ernzerhof, *Generalized Gradient Approximation Made Simple*, *Phys. Rev. Lett.* **77**, 3865–3868 (1996).
- [150] S. Grimme, J. Antony, S. Ehrlich, and H. Krieg, *A Consistent and Accurate Ab Initio Parametrization of Density Functional Dispersion Correction (DFT-D) for the 94 Elements H-Pu*, *J. Chem. Phys.* **132**, 154104 (2010).
- [151] J. Klimeš, D. R. Bowler, and A. Michaelides, *Chemical Accuracy for the Van Der Waals Density Functional*, *J. Phys.: Condens. Matter* **22**, 022201 (2009).
- [152] J. Heyd, G. E. Scuseria, and M. Ernzerhof, *Hybrid Functionals Based on a Screened Coulomb Potential*, *Chem. Phys.* **118**, 8207–8215 (2003).
- [153] A. V. Krukau, O. A. Vydrov, A. F. Izmaylov, and G. E. Scuseria, *Influence of the Exchange Screening Parameter on the Performance of Screened Hybrid Functionals*, *J. Chem. Phys.* **125**, 224106 (2006).
- [154] C. Zheng and O. Rubel, *Aziridinium Lead Iodide: A Stable, Low-Band-Gap Hybrid Halide Perovskite for Photovoltaics*, *J. Phys. Chem. Lett.* **9**, 874–880 (2018).
- [155] E. F. Schubert, *Light-emitting diodes* (E. Fred Schubert, 2018).

- [156] J. Nelson, *The physics of solar cells* (World Scientific Publishing Company, 2003).
- [157] L. Zeng, Y. Yi, C. Hong, J. Liu, N. Feng, X. Duan, L. Kimerling, and B. Alamariu, *Efficiency Enhancement in Si Solar Cells by Textured Photonic Crystal Back Reflector*, *Appl. Phys. Lett.* **89**, 111111 (2006).
- [158] S. D. Stranks, G. E. Eperon, G. Grancini, C. Menelaou, M. J. Alcocer, T. Leijtens, L. M. Herz, A. Petrozza, and H. J. Snaith, *Electron-Hole Diffusion Lengths Exceeding 1 Micrometer in an Organometal Trihalide Perovskite Absorber*, *Science* **342**, 341–344 (2013).
- [159] X. Y. Chin, D. Cortecchia, J. Yin, A. Bruno, and C. Soci, *Lead Iodide Perovskite Light-Emitting Field-Effect Transistor*, *Nat. Commun.* **6**, 7383 (2015).
- [160] S. Siegel and E. Gebert, *The Structures of Hexagonal CsCdCl₃ and Tetragonal Cs₂CdCl₄*, *Acta Cryst.* **17**, 790–790 (1964).
- [161] T. J. Huang, Z. X. Thiang, X. Yin, C. Tang, G. Qi, and H. Gong, *(CH₃NH₃)₂PdCl₄: A Compound with Two-Dimensional Organic–Inorganic Layered Perovskite Structure*, *Chem. Eur. J.* **22**, 2146–2152 (2016).
- [162] X. Liu, T. J. Huang, L. Zhang, B. Tang, N. Zhang, D. Shi, and H. Gong, *Highly Stable, New, Organic-Inorganic Perovskite (CH₃NH₃)₂PdBr₄: Synthesis, Structure, and Physical Properties*, *Chem. Eur. J.* **24**, 4991–4998 (2018).
- [163] N. Sakai, A. A. Haghighirad, M. R. Filip, P. K. Nayak, S. Nayak, A. Ramadan, Z. Wang, F. Giustino, and H. J. Snaith, *Solution-Processed Cesium Hexabromopalladate (IV), Cs₂PdBr₆, for Optoelectronic Applications*, *J. Am. Chem. Soc.* **139**, 6030–6033 (2017).
- [164] R. Roccanova, W. Ming, V. R. Whiteside, M. A. McGuire, I. R. Sellers, M.-H. Du, and B. Saparov, *Synthesis, Crystal and Electronic Structures, and Optical Properties of (CH₃NH₃)₂CdX₄ (X= Cl, Br, I)*, *Inorg. Chem.* **56**, 13878–13888 (2017).
- [165] M. A. Green, A. Ho-Baillie, and H. J. Snaith, *The Emergence of Perovskite Solar Cells*, *Nat. Photon.* **8**, 506–514 (2014).
- [166] K. Tanaka, T. Takahashi, T. Ban, T. Kondo, K. Uchida, and N. Miura, *Comparative Study on the Excitons in Lead-Halide-Based Perovskite-Type Crystals CH₃NH₃PbBr₃ CH₃NH₃PbI₃*, *Solid State Commun.* **127**, 619–623 (2003).
- [167] W.-J. Yin, T. Shi, and Y. Yan, *Unusual Defect Physics in CH₃NH₃PbI₃ Perovskite Solar Cell Absorber*, *Appl. Phys. Lett.* **104**, 063903 (2014).
- [168] Z. Xiao, W. Meng, J. Wang, and Y. Yan, *Thermodynamic Stability and Defect Chemistry of Bismuth-Based Lead-Free Double Perovskites*, *ChemSusChem* **9**, 2628–2633 (2016).
- [169] T. Li, X. Zhao, D. Yang, M.-H. Du, and L. Zhang, *Intrinsic Defect Properties in Halide Double Perovskites for Optoelectronic Applications*, *Phys. Rev. Appl.* **10**, 041001 (2018).

- [170] K. Kuhar, A. Crovetto, M. Pandey, K. S. Thygesen, B. Seger, P. C. Vesborg, O. Hansen, I. Chorkendorff, and K. W. Jacobsen, *Sulfide Perovskites for Solar Energy Conversion Applications: Computational Screening and Synthesis of the Selected Compound LaYS₃*, Energy Environ. Sci. **10**, 2579–2593 (2017).
- [171] A. M. Elseman, A. E. Shalan, S. Sajid, M. M. Rashad, A. M. Hassan, and M. Li, *Copper-Substituted Lead Perovskite Materials Constructed with Different Halides for Working (CH₃NH₃)₂CuX₄-Based Perovskite Solar Cells from Experimental and Theoretical View*, ACS Appl. Mater. Interfaces **10**, 11699–11707 (2018).
- [172] S. Abrahams, J. Ihringer, and P. Marsh, *Structural and Thermal Dependence of Normal-Mode Condensations in K₂TeBr₆*, Acta Crystallogr. Sect. B **45**, 26–34 (1989).
- [173] B. Delley and E. Steigmeier, *Quantum Confinement in Si Nanocrystals*, Phys. Rev. B **47**, 1397 (1993).
- [174] J. K. Ellis, M. J. Lucero, and G. E. Scuseria, *The Indirect to Direct Band Gap Transition in Multilayered MoS₂ as Predicted by Screened Hybrid Density Functional Theory*, Appl. Phys. Lett. **99**, 261908 (2011).
- [175] A. Kojima, K. Teshima, Y. Shirai, and T. Miyasaka, *Organometal Halide Perovskites as Visible-Light Sensitizers for Photovoltaic Cells*, J. Am. Chem. Soc. **131**, 6050–6051 (2009).
- [176] W. S. Yang, B.-W. Park, E. H. Jung, N. J. Jeon, Y. C. Kim, D. U. Lee, S. S. Shin, J. Seo, E. K. Kim, J. H. Noh, and S. I. Seok, *Iodide Management in Formamidinium-Lead-Halide-based Perovskite Layers for Efficient Solar Cells*, Science **356**, 1376–1379 (2017).
- [177] N. R. E. Laboratory, *Research Cell Record Efficiency Chart* (2019). [Online; accessed August 23, 2019].
- [178] C. Bernal and K. Yang, *First-Principles Hybrid Functional Study of the Organic–Inorganic Perovskites CHNH₃SnBr₃ and CH₃NH₃SnI₃*, J. Phys. Chem. C **118**, 24383–24388 (2014).
- [179] G. Kresse and J. Furthmüller, *Efficient Iterative Schemes for Ab-Initio Total-Energy Calculations Using a Plane-Wave Basis Set*, Phys. Rev. B **54**, 11169–11186 (1996).
- [180] P. E. Blöchl, *Projector Augmented-Wave Method*, Phys. Rev. B **50**, 17953–17979 (1994).
- [181] A. A. Emery, J. E. Saal, S. Kirklin, V. I. Hegde, and C. Wolverton, *High-Throughput Computational Screening of Perovskites for Thermochemical Water Splitting Applications*, Chem. Mater. **28**, 5621–5634 (2016).
- [182] M. T. Curnan and J. R. Kitchin, *Effects of Concentration, Crystal Structure, Magnetism, and Electronic Structure Method on First-Principles Oxygen Vacancy Formation Energy Trends in Perovskites*, J. Phys. Chem. C **118**, 28776–28790 (2014).

- [183] C. Freysoldt, J. Neugebauer, and C. G. Van de Walle, *Fully Ab Initio Finite-Size Corrections for Charged-Defect Supercell Calculations*, Phys. Rev. Lett. **102**, 016402 (2009).
- [184] T. M. Brenner, D. A. Egger, L. Kronik, G. Hodes, and D. Cahen, *Hybrid Organic—inorganic Perovskites: Low-Cost Semiconductors with Intriguing Charge-Transport Properties*, Nat. Rev. Mater. **1**, 15007 (2016).
- [185] S. D. Stranks and H. J. Snaith, *Metal-Halide Perovskites for Photovoltaic and Light-Emitting Devices*, Nat. Nanotechnol. **10**, 391–402 (2015).
- [186] J. Burschka, N. Pellet, S.-J. Moon, R. Humphry-Baker, P. Gao, M. K. Nazeeruddin, and M. Grätzel, *Sequential Deposition as a Route to High-Performance Perovskite-Sensitized Solar Cells*, Nature **499**, 316–319 (2013).
- [187] L. Etgar, P. Gao, Z. Xue, Q. Peng, A. K. Chandiran, B. Liu, M. K. Nazeeruddin, and M. Grätzel, *Mesoscopic CH₃NH₃PbI₃/TiO₂ Heterojunction Solar Cells*, J. Am. Chem. Soc. **134**, 17396–17399 (2012).
- [188] B. V. Lotsch, *New Light on an Old Story: Perovskites Go Solar*, Angew. Chem. Int. Ed. **53**, 635–637 (2014).
- [189] N.-G. Park, *Organometal Perovskite Light Absorbers Toward a 20% Efficiency Low-Cost Solid-State Mesoscopic Solar Cell*, J. Phys. Chem. Lett. **4**, 2423–2429 (2013).
- [190] Y. Yamada, T. Nakamura, M. Endo, A. Wakamiya, and Y. Kanemitsu, *Near-Band-Edge Optical Responses of Solution-Processed Organic—inorganic Hybrid Perovskite CH₃NH₃PbI₃ on Mesoporous TiO₂ Electrodes*, Appl. Phys. Express **7**, 032302 (2014).
- [191] B. J. Foley, D. L. Marlowe, K. Sun, W. A. Saidi, L. Scudiero, M. C. Gupta, and J. J. Choi, *Temperature Dependent Energy Levels of Methylammonium Lead Iodide Perovskite*, Appl. Phys. Lett. **106**, 243904 (2015).
- [192] H. J. Snaith, *Perovskites: the Emergence of a New Era for Low-Cost, High-Efficiency Solar Cells*, J. Phys. Chem. Lett. **4**, 3623–3630 (2013).
- [193] W.-J. Yin, T. Shi, and Y. Yan, *Unique Properties of Halide Perovskites as Possible Origins of the Superior Solar Cell Performance*, Adv. Mater. **26**, 4653–4658 (2014).
- [194] A. Buin, P. Pietsch, J. Xu, O. Voznyy, A. H. Ip, R. Comin, and E. H. Sargent, *Materials Processing Routes to Trap-Free Halide Perovskites*, Nano Lett. **14**, 6281–6286 (2014).
- [195] D. Shi, V. Adinolfi, R. Comin, M. Yuan, E. Alarousu, A. Buin, Y. Chen, S. Hoogland, A. Rothenberger, K. Katsiev, Y. Losovyj, X. Zhang, P. A. Dowben, O. F. Mohammed, E. H. Sargent, and O. M. Bakr, *Low Trap-State Density and Long Carrier Diffusion in Organolead Trihalide Perovskite Single Crystals*, Science **347**, 519–522 (2015).

- [196] G. Xing, N. Mathews, S. Sun, S. S. Lim, Y. M. Lam, M. Grätzel, S. Mhaisalkar, and T. C. Sum, *Long-Range Balanced Electron- and Hole-Transport Lengths in Organic–Inorganic $\text{CH}_3\text{NH}_3\text{PbI}_3$* , *Science* **342**, 344–347 (2013).
- [197] J. You, Z. Hong, Y. M. Yang, Q. Chen, M. Cai, T.-B. Song, C.-C. Chen, S. Lu, Y. Liu, H. Zhou, and Y. Yang, *Low-Temperature Solution-Processed Perovskite Solar Cells with High Efficiency and Flexibility*, *ACS Nano* **8**, 1674–1680 (2014).
- [198] Y. Zhao and K. Zhu, *Solution Chemistry Engineering Toward High-Efficiency Perovskite Solar Cells*, *J. Phys. Chem. Lett.* **5**, 4175–4186 (2014).
- [199] F. Bi, S. Markov, R. Wang, Y. Kwok, W. Zhou, L. Liu, X. Zheng, G. Chen, and C. Yam, *Enhanced Photovoltaic Properties Induced by Ferroelectric Domain Structures in Organometallic Halide Perovskites*, *J. Phys. Chem. C* **121**, 11151–11158 (2017).
- [200] C.-J. Tong, W. Geng, O. V. Prezhdo, and L.-M. Liu, *Role of Methylammonium Orientation in Ion Diffusion and Current–Voltage Hysteresis in the $\text{CH}_3\text{NH}_3\text{PbI}_3$ Perovskite*, *ACS Energy Lett.* **2**, 1997–2004 (2017).
- [201] J. Jankowska and O. V. Prezhdo, *Ferroelectric Alignment of Organic Cations Inhibits Nonradiative Electron–Hole Recombination in Hybrid Perovskites: Ab Initio Nonadiabatic Molecular Dynamics*, *J. Phys. Chem. Lett.* **8**, 812–818 (2017).
- [202] S. Kanno, Y. Imamura, A. Saeki, and M. Hada, *Rotational Energy Barriers and Relaxation Times of the Organic Cation in Cubic Methylammonium Lead/Tin Halide Perovskites from First Principles*, *J. Phys. Chem. C* **121**, 14051–14059 (2017).
- [203] G. Kresse and J. Furthmüller, *Efficiency of Ab-Initio Total Energy Calculations for Metals and Semiconductors Using a Plane-Wave Basis Set*, *Comput. Mater. Sci.* **6**, 15–50 (1996).
- [204] W.-J. Yin, Y. Yan, and S.-H. Wei, *Anomalous Alloy Properties in Mixed Halide Perovskites*, *J. Phys. Chem. Lett.* **5**, 3625–3631 (2014).
- [205] K. Momma and F. Izumi, *VESTA 3 for Three-Dimensional Visualization of Crystal, Volumetric and Morphology Data*, *J. Appl. Crystallogr.* **44**, 1272–1276 (2011).
- [206] S. Nazir, M. Behtash, and K. Yang, *Enhancing Interfacial Conductivity and Spatial Charge Confinement of $\text{LaAlO}_3/\text{SrTiO}_3$ Heterostructures via Strain Engineering*, *Appl. Phys. Lett.* **105**, 141602–141605 (2014).
- [207] T. J. Jacobsson, J.-P. Correa-Baena, M. Pazoki, M. Saliba, K. Schenk, M. Grätzel, and A. Hagfeldt, *Exploration of the Compositional Space for Mixed Lead Halogen Perovskites for High Efficiency Solar Cells*, *Energy Environ. Sci.* **9**, 1706–1724 (2016).
- [208] W.-L. Yan, G.-H. Lu, and F. Liu, *Effect of Chlorine Substitution on Lattice Distortion and Ferroelectricity of $\text{CH}_3\text{NH}_3\text{PbI}_3$* , *J. Phys. Chem. C* **120**, 17972–17977 (2016).

- [209] L. Atourki, E. Vega, B. Marí, M. Mollar, H. A. Ahsaine, K. Bouabid, and A. Ihlal, *Role of the Chemical Substitution on the Structural and Luminescence Properties of the Mixed Halide Perovskite Thin MAPbI_{3-x}Br_x(0 ≤ X ≤ 1) Films*, Appl. Sur. Sci. **371**, 112–117 (2016).
- [210] C. Quarti, E. Mosconi, P. Umari, and F. De Angelis, *Chlorine Incorporation in the CH₃NH₃PbI₃ Perovskite: Small Concentration, Big Effect*, Inorg. Chem. **56**, 74–83 (2017).
- [211] J. Liu and O. V. Prezhdo, *Chlorine Doping Reduces Electron–hole Recombination in Lead Iodide Perovskites: Time-Domain Ab Initio Analysis*, J. Phys. Chem. Lett. **6**, 4463–4469 (2015).
- [212] M. Jiang, J. Wu, F. Lan, Q. Tao, D. Gao, and G. Li, *Enhancing the Performance of Planar Organo-Lead Halide Perovskite Solar Cells by Using a Mixed Halide Source*, J. Mater. Chem. A **3**, 963–967 (2015).
- [213] M.-c. Kim, B. J. Kim, D.-Y. Son, N.-G. Park, H. S. Jung, and M. Choi, *Observation of Enhanced Hole Extraction in Br Concentration Gradient Perovskite Materials*, Nano Lett. **16**, 5756–5763 (2016).
- [214] D. Bi, W. Tress, M. I. Dar, P. Gao, J. Luo, C. Renevier, K. Schenk, A. Abate, F. Giordano, J.-P. C. Baena, J.-D. Decoppet, S. M. Zakeeruddin, M. K. Nazeeruddin, M. Grätzel, and A. Hagfeldt, *Efficient Luminescent Solar Cells Based on Tailored Mixed-Cation Perovskites*, Sci. Adv. **2**, e1501170 (2016).
- [215] X. Zheng, C. Wu, S. K. Jha, Z. Li, K. Zhu, and S. Priya, *Improved Phase Stability of Formamidinium Lead Triiodide Perovskite by Strain Relaxation*, ACS Energy Lett. **1**, 1014–1020 (2016).
- [216] C. Yi, J. Luo, S. Meloni, A. Boziki, N. Ashari-Astani, C. Grätzel, S. M. Zakeeruddin, U. Röthlisberger, and M. Grätzel, *Entropic Stabilization of Mixed A-Cation ABX₃ Metal Halide Perovskites for High Performance Perovskite Solar Cells*, Energy Environ. Sci. **9**, 656–662 (2016).
- [217] O. Y. Gorbenko, S. Samoilenov, I. Graboy, and A. Kaul, *Epitaxial Stabilization of Oxides in Thin Films*, Chem. Mater. **14**, 4026–4043 (2002).
- [218] Z. Xu, P. Salvador, and J. R. Kitchin, *First-Principles Investigation of the Epitaxial Stabilization of Oxide Polymorphs: TiO₂ on (Sr,Ba)TiO₃*, ACS Appl. Mater. Interfaces **9**, 4106–4118 (2017).
- [219] T. Chen, B. J. Foley, C. Park, C. M. Brown, L. W. Harriger, J. Lee, J. Ruff, M. Yoon, J. J. Choi, and S.-H. Lee, *Entropy-Driven Structural Transition and Kinetic Trapping in Formamidinium Lead Iodide Perovskite*, Sci. Adv. **2**, e1601650 (2016).
- [220] B. Liu, M. Long, M.-Q. Cai, X. Hao, and J. Yang, *Ferroelectric Polarization in CsPbI₃/CsSnI₃ Perovskite Heterostructure*, J. Phys. Chem. C **122**, 17820–17824 (2018).

- [221] C. Zhu, X. Niu, Y. Fu, N. Li, C. Hu, Y. Chen, X. He, G. Na, P. Liu, H. Zai, Y. Ge, Y. Lu, X. Ke, Y. Bai, S. Yang, P. Chen, Y. Li, M. Sui, L. Zhang, H. Zhou, and Q. Chen, *Strain Engineering in Perovskite Solar Cells and Its Impacts on Carrier Dynamics*, Nat. Commun. **10**, 815 (2019).
- [222] Z. Xiao, Y. Yan, H. Hosono, and T. Kamiya, *Roles of Pseudo-Closed s^2 Orbitals for Different Intrinsic Hole Generation between Tl–Bi and In–Bi Bromide Double Perovskites*, J. Phys. Chem. Lett. **9**, 258–262 (2018).
- [223] G. Tang, Z. Xiao, and J. Hong, *Designing Two-Dimensional Properties in Three-Dimensional Halide Perovskites via Orbital Engineering*, J. Phys. Chem. Lett. **10**, 6688–6694 (2019).